The Electrodeless Lorentz Force Thruster Experiment

Thomas E. Weber

A dissertation submitted in partial fulfillment

of the requirements for the degree of

Doctor of Philosophy

University of Washington

2010

Program authorized to offer degree:

Department of Aeronautics & Astronautics

University of Washington

Abstract

The Electrodeless Lorentz Force Thruster Experiment

Thomas E. Weber

Chair of the Supervisory Committee:
Research Associate Professor John Slough
Department of Aeronautics & Astronautics

The Electrodeless Lorentz Force (ELF) thruster is a novel type of plasma thruster, which utilizes Rotating Magnetic Field current drive within a diverging magnetic field to form, accelerate, and eject a Field Reversed Configuration plasmoid. The ELF program is a result of a Small Business Technology Transfer grant awarded to MSNW LLC by the Air Force Office of Scientific Research for the research of the revolutionary space propulsion concept represented by ELF. These grants are awarded to small businesses working in collaboration with a university, in this case, the University of Washington. The program was split into two concurrent research efforts; a numerical modeling study undertaken at the UW branch of the Plasma Science and Innovation Center, and an experimental effort taking place at the UW Plasma Dynamics Laboratory with additional support from MSNW (the latter being the subject of this dissertation). It is the aim of this dissertation is to present to the reader the necessary background information needed to understand the operation of the ELF thruster, an overview of the experimental setup, a review of the significant experimental findings, and a discussion regarding the operation and performance of the thruster.

Contents

List of Figures

List of Tables

Chapter 1

Introduction

This chapter serves as an introduction to the Electrodeless Lorentz Force (ELF) thruster experimental program. Motivation for the development of an ELF-type thruster precedes a brief review of the physical processes taking place within the ELF thruster, including the utility of Field Reversed Configuration (FRC) plasmoids to space propulsion, FRC equilibria, Rotating Magnetic Field current drive, and FRC energy content and expansion. An outline of the typical operation of ELF is given, followed by a short discussion on the merits of the ELF thruster concept.

1.1 Plasma Propulsion

In order to effectively explore and colonize space, man must be capable of traveling throughout the solar system in a relatively short time frame, and have the ability to do so with a large enough payload to effectively complete the desired ob-

jective. Similarly, for missions in cis-lunar space, it is attractive to have a spacecraft capable of fast orbital maneuvers that can carry a large payload or is capable of flying missions that require large changes in velocity (ΔV) without the requirement of refueling. For these types of missions, if the propellant mass is not to dominate the spacecraft, the thruster needs to be capable of providing a large amount of impulse while using very little propellant (high specific impulse).

Upon examination of the Rocket Equation (first derived by Konstantin Tsiolkovsky in 1903[6]),

$$\frac{m_o}{m_b} = e^{\Delta V/v_e} \tag{1.1}$$

(where m_o is the initial mass of the spcacecraft, m_b is the burnout mass,ΔV is the total mission velocity increment, and v_e is the exhaust velocity) it becomes clear that in order to keep the propellant mass at a reasonable level, the exhaust velocity must be at or above the total mission ΔV. Presently the highest exhaust velocity attainable by chemical rockets is roughly 5 km/s. This limitation makes their use inappropriate (or impossible) for high-energy missions where the ΔV requirements are large. Electric (plasma) propulsion provides a means to increase the exhaust velocity of the propellant, thus expanding the range of possible missions. The most significant handicap of electric propulsion is the fact that the thrusters that are currently space-qualified all have a very low power/mass ratio, which translates to low thrust, and long mission times.

The thrust (T) and power (P) can be computed from the exhaust velocity and

the mass flow ($\dot{m}$) rate.

$$T = \dot{m} v_e \tag{1.2}$$

$$P = \frac{1}{2}\dot{m} v_e^2 = \frac{1}{2} v_e T \tag{1.3}$$

Equation 1.1 shows that high exhaust velocity is desirable to reduce propellant mass, however, equation 1.3 shows that for a given thrust, an increase in exhaust velocity requires an increase in power. As the exhaust velocity is increased, a point will be reached when the mass savings in propellant will be counteracted by the additional power plant mass. A good rule of thumb is that for a given mission, the exhaust velocity of the thruster should be equal to the ΔV of the mission up to that point.

High specific impulse missions that have utilized electric propulsion have been flown to date, although historically the power has been limited to only a few kilowatts by the power sources available in space, this situation appears to be changing. The International Space Station (ISS) currently generates the most power of any man made object in space at roughly 100 kW [7]. The solar arrays on the ISS are heavy and bulky, but technology is improving quickly. A state-of-the-art solar array such as the Ultraflex Array (which will be flown on the Space Technology 8 (ST8) mission) is capable of producing $\sim$ 200 W/kg and has the ability to fold into a very small size during launch [8]. Considering the rapid development of solar technology it is likely that a mobile spacecraft powered by solar arrays will soon be capable of producing power in the hundreds of kilowatts.

Sometimes the use of solar panels is not an option, such as in missions to the outer planets. An alternative to solar arrays is to use nuclear fission as a power source. The largest drawback to using nuclear power is that it requires a large investment in mass to start producing power. However, the power produced by a reactor does not scale linearly with mass, as it does with solar power. At 100 kW the specific power is around 25-30 W/kg, at 10 MW the specific power is 250-300 W/kg, and at 200 MW the specific power is 500 W/kg [9, 10]. With these trends, it is not out of the realm of possibility that it is possible to launch a spacecraft capable of producing megawatts of power in the near future (not considering economic or political factors). Regardless of the power plant, plasma thrusters capable of operating at power levels in excess of 100 kW may soon be coming into demand.

The ELF thruster is intended to fill the need for a plasma thruster capable of operating efficiently at any power level, while also being lightweight and small in size. This is accomplished by repetitively ejecting coherent masses of plasma called Field Reversed Configurations (FRCs) at high frequency and high velocity. As will be seen, the operation of ELF inherently sidesteps many potential pitfalls associated with high power plasma propulsion, while simultaneously providing multiple beneficial thruster qualities.

1.2 Pulsed Plasmoid Propulsion

The ELF thruster generates thrust through the creation and subsequent ejection of a configuration of plasma known as a Field Reversed Configuration (FRC).

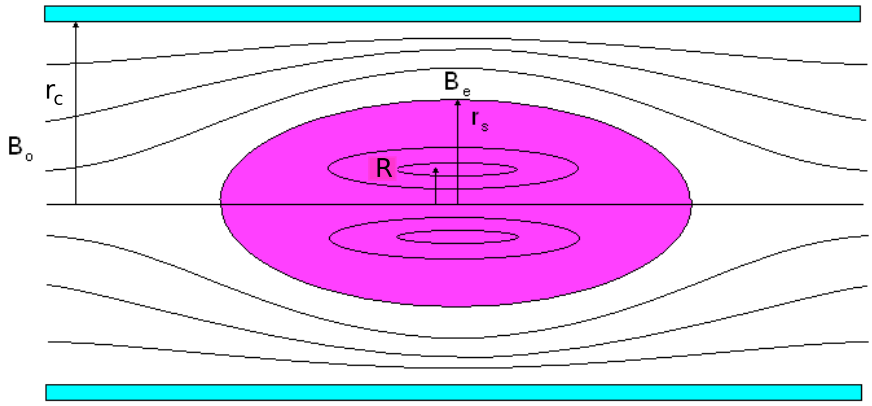

Figure 1.1: FRC magnetic topology.

An FRC is classified as a plasmoid, in that it is a coherent structure of plasma and magnetic field. It also has a closed magnetic structure, a simply connected separatrix, and a toroidal internal magnetic topology (see Figure 1.1). The current in an FRC is purely toroidal, making the internal magnetic fields purely poloidal. The term Field Reversed Configuration stems from the observation that the direction of the field on axis within an FRC is reversed from that of the vacuum bias field.

The FRC is mostly studied as a fusion energy plasma confinement concept, and as such, is capable of being produced at very high energy densities. It is for this reason that that a thruster which ejects FRCs for the production of thrust is capable of very high thrust densities.

The periodic ejection of FRCs has several inherent benefits over the ejection of a steady state stream of plasma produced by the leading plasma thrusters. Perhaps the greatest advantage is the extreme scalability in power attainable through pulsed operation. Thrusters which employ a steady stream of exhaust are optimized for

a certain power and mass flow rate, with any deviation from the prescribed values resulting in a decrease of efficiency and a change in the exhaust velocity. In contrast, the operation of a pulsed thruster is optimized for operation over one pulse. The power can be scaled simply by pulsing more or less often, with essentially no change in the operation of the thruster. In this way, the thruster can maintain maximum efficiency at any desired power level with no change in the exhaust velocity.

Another major advantage of FRC propulsion is the fact that the plasma is contained within a closed magnetic structure that is isolated from the external magnetic field. Thus, there is no need for the plasma to detach itself from field lines that are tied to the thruster in order to escape the vicinity of the spacecraft. This allows the FRC to be formed within and ejected by the applied field without being tied to it. Expanding the FRC allows the thermal energy of the plasma to be converted to kinetic energy through the expansion and acceleration of the FRC much in the same manner that a rocket nozzle converts the thermal energy of the exhaust into bulk velocity.

1.3 FRC Equilibrium

Although an FRC is an equilibrium configuration, in ELF, equilibrium is never fully attained. However, since the configuration is approximately in equilibrium during some phases of the formation and ejection process, known information regarding FRC equilibria can be applied during these times. Most importantly, while the FRC is approximately in radial equilibrium, many of the properties of the con-

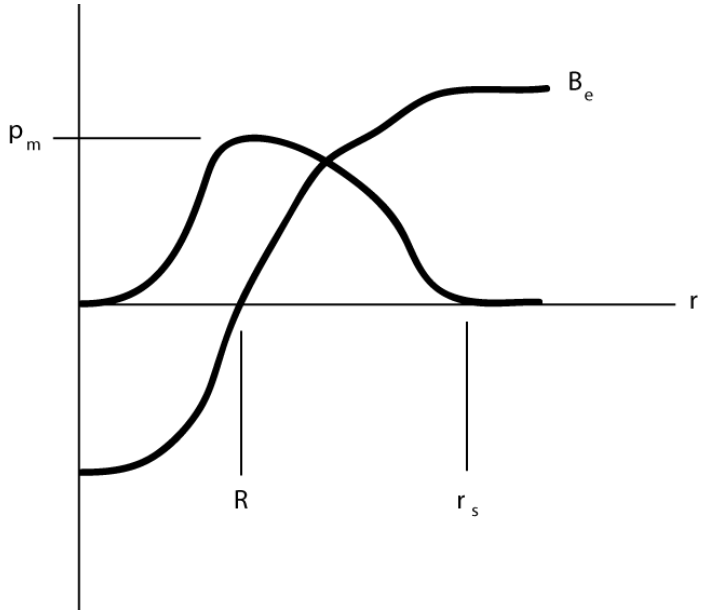

Figure 1.2: Typical magnetic and pressure profiles near the middle of an FRC.

figuration can be captured with a 1-D model of the radial profile.

Consider an FRC in radial equilibrium inside a flux conserving cylinder (as in Figure 1.1) with a known radius (r_c) and vacuum axial magnetic bias field (B_o). It is assumed that the FRC is elongated (prolate, with $l \geq r_s$, where l is the length of the FRC and r_s is the radius of the separatrix) with a racetrack-shaped separatrix (straight field lines along most of the length). Since the nominal FRC is azimuthally symmetric, it can be described in terms of the total length and a 1D radial profile.

The radial magnetic and gas pressure profiles near the middle of the FRC typically resemble Fig. 1.2. Pressure is peaked (p_m) at the magnetic null ($r = R$), and the external magnetic field (B_e) is uniformly compressed outside the separatrix ($r_s < r < r_c$). Within the separatrix ($r < r_s$) the total pressure (gas pressure +

magnetic pressure) is constant (radial pressure balance), providing a relationship between the gas pressure and magnetic field.

$$p_m = p + \frac{B^2}{2\mu_o} = \frac{B_e^2}{2\mu_o} \tag{1.4}$$

Since the FRC is in a static equilibrium, it is reasonable to assume that pressure gradients do not exist along field lines, making pressure a function of the magnetic flux ($p = p(\psi)$). Since pressure is a function of flux, the cross sectional area between the axis and the magnetic null is equal to the area between the magnetic null and the separatrix, and the location of the magnetic null is $R = r_s/\sqrt{2}$. The flux of the external field is the same whether or not the FRC is present and is simply $\phi_e = \pi r_c^2 B_o = \pi(r_c^2 - r_s^2)B_e$, where B_o is the field when the FRC is not present (see Figure 1.1). This flux relation sets the value of the external field to

$$B_e = \frac{B_o}{1 - x_s^2} \tag{1.5}$$

where $x_s = r_s/r_c$.

By integrating the Maxwell stress tensor and the gas pressure (from Equation 1.4) over a volume containing half the FRC and considering axial forces, one obtains the relation [1]

$$\langle\beta\rangle = 1 - \frac{x_s^2}{2} \tag{1.6}$$

in which the average beta is the ratio of the average gas pressure to external magnetic pressure ($\langle\beta\rangle = \frac{\langle p\rangle}{B_e^2/2\mu_o}$). This can be a particularly useful relation, since

it permits the calculation of average global quantities from the knowledge of x_s.

In an important corallary to Equation 1.6, the total magnetic flux within the FRC can be found to be [1]

$$\phi_{FRC} = \frac{\pi}{2} r_s^2 B_e \left(\frac{x_s}{\sqrt{2}} \right)^{1+\epsilon} \tag{1.7}$$

where the parameter ϵ depends on the specific shape of the profile. The amount of magnetic flux contained within the FRC can vary between two extremes corresponding to the sharp boundary ($\epsilon = 1$, minimum possible flux) and the modified sharp boundary ($\epsilon = 0$, maximum possible flux) magnetic profiles. The amount of flux is later shown to be a useful quantity in determining the expansion of an FRC in a diverging magnetic field.

The radial profile of most FRC equilibria can be described by a rigid-rotor FRC model in which the electrons rotate uniformly [13]. The density and magnetic field are given by

$$n_e = n_m \mathrm{sech}^2 K_{RR} u \tag{1.8}$$

$$B_z = B_e \tanh K_{RR} u \tag{1.9}$$

where $u = (r/R)^2 - 1$, n_m is the density at the magnetic null, and K_{RR} is the rigid-rotor profile factor (near unity).

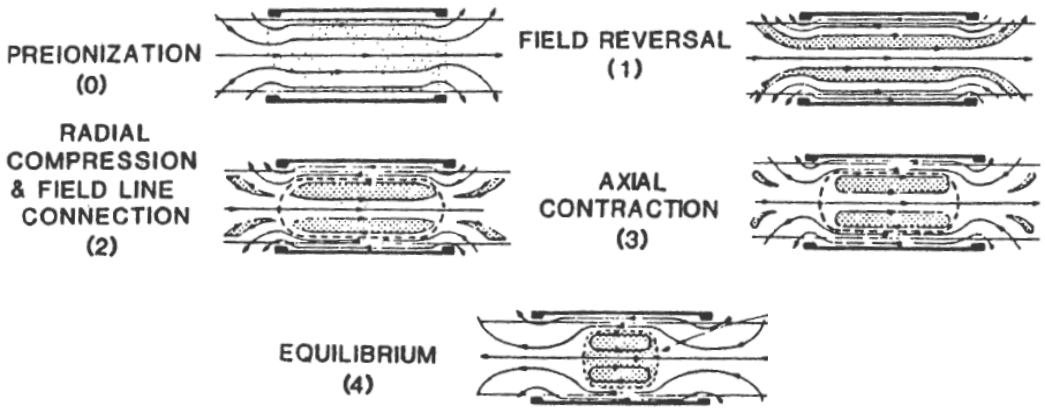

Figure 1.3: Field reversed theta-pinch (FRTP) FRC formation [1].

1.4 FRC Formation

There are several methods of forming an FRC as briefly outlined in [1]. However, formation in the context of a space thruster places some restrictions on the characteristics of the chosen formation process. Most importantly, the formation method must take place in a geometry amenable to the ejection of an FRC from one end of the formation section, it must utilize potentially lightweight efficient hardware, and it must take place on a fairly short timescales to reduce radiative losses as much as possible. Two formation methods satisfy these requirements: the Field Reversed Theta Pinch (FRTP) formation method, and the Rotating Magnetic Field (RMF) formation method.

The FRTP method (shown in Figure 1.3) is currently the most widely utilized FRC formation scheme. The formation process begins with a pre-ionized plasma column in which a reversed axial bias field is embedded. The axial field is then

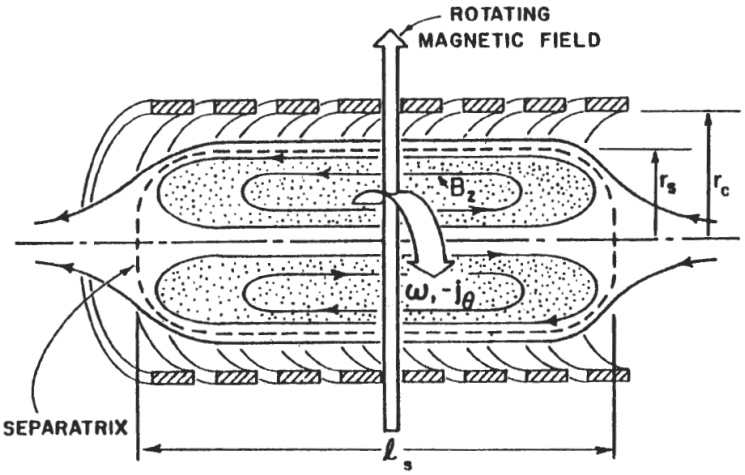

Figure 1.4: Rotating magnetic field (RMF) current drive [1].

reversed faster than the resistive diffusion timescale. The axial fields on the ends of the plasma column reconnect and form a closed FRC.

The FRTP method is capable of producing high density, high temperature FRCs and initiating translation over very short timescales (microseconds). However, this scheme demands a very large swing of flux over a very short time during formation, which requires the utilization of large, high voltage pulsed power systems. In addition, during part of the formation process, hot plasma is swept against the wall of the formation chamber, which sputters material from the wall, and drains energy from the plasma. Large amounts of energy can also be lost if the pre-ionized gas is not conductive enough to hold in the initial flux. For these and other reasons, the FRTP method has historically proven to be a relatively inefficient method of formation.

RMF current drive (first used by Blevin and Thonemann in 1962 [11]) utilizes

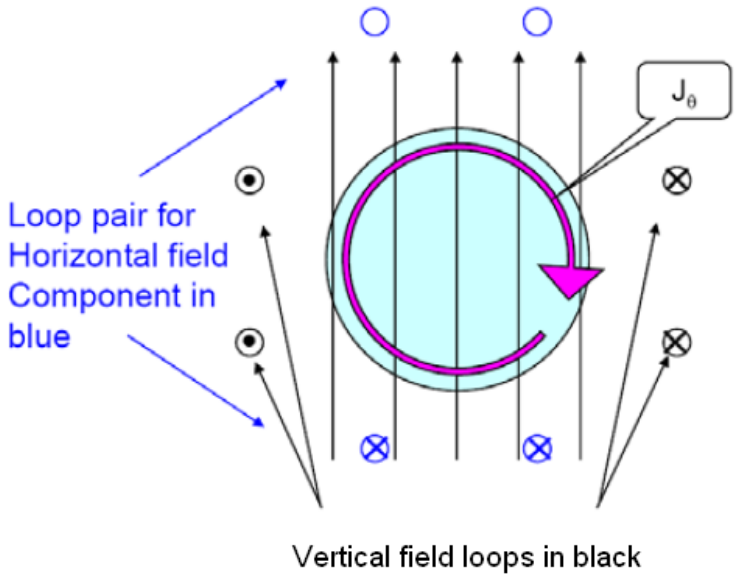

Figure 1.5: End-on view of RMF.

a rotating magnetic field transverse to the plasma column (see Figures 1.4 and 1.5) which rotates at a frequency between the ion cyclotron and the electron cyclotron frequencies.

$$\omega_{ci} < \omega_{RMF} < \omega_{ce} \tag{1.10}$$

The motion of the electrons is capable of responding to the magnetic fields over the short timescales of the oscillation, and as a result, a synchronous azimuthal electron rotation at the same angular velocity as the RMF is driven. Due to their larger mass, the ions cannot respond to the rotating field and therefore do not experience an average azimuthal driving force. As long as this configuration is maintained, the driven current resembles that of a rigid rotor ($j_\theta = -ne\omega r$) [12, 13].

Figure 1.4 and 1.5 depict the typical layout of an RMF system. Two orthogonal

Helmholtz pairs (henceforth referred to as antennae) oscillate out of phase with each other to produce a steady magnetic field which rotates in the $r-\theta$ plane transverse to the axial bias field. Thus the fields within the RMF formation region can be written in the form of Equation 1.11.

$$\mathbf{B} = B_\omega \cos(\omega t)\hat{\mathbf{e}_\mathbf{r}} + B_\omega \sin(\omega t)\hat{\mathbf{e}_\theta} + B_z\hat{\mathbf{e}_\mathbf{z}} \tag{1.11}$$

RMF is a non-inductive form of current drive ($I_{RMF} \propto \omega$ rather than $I \propto \Delta\phi$, as in the FRTP formation scheme), thus it is capable of driving significant amounts of current without the inherent requirement of high magnetic fields. High voltages can be developed on the antennae due to the high frequencies used, however, since the magnitude of the magnetic field can be low, the currents used can also be low, and the system as a whole can be made to be very lightweight and with more efficient components. There are also several secondary benefits to the use of RMF, for example, if the gas does not immediately break down upon application of the RMF, the RMF simply continues to ring with very little inherent energy loss until the gas breaks down. Also, since the field is never reversed, at no time during the formation process does hot plasma come into physical contact with the chamber wall, this limits the energy dissipated during the formation process to radiative losses. It is for these reasons that RMF formation is thought to be a potentially very efficient and lightweight formation technique for pulsed FRC formation in ELF.

In addition to the requirement stated in Equation 1.10 that the RMF frequency

lie between the ion and electron cyclotron frequencies, it is also required that the collision frequency of the electrons be less than the cyclotron frequency. This is needed in order for the electrons to be able to complete their orbital motion within the magnetic field, if the motion of the electrons is interrupted by a collision before one gyro-orbit can be completed, then the electrons will not remain magnetized to the RMF.

$$\gamma = \frac{\omega_{ce}}{\nu_{ei}} > 1 \tag{1.12}$$

Another important dimensionless parameter is the ratio of the plasma depth to the resistive skin depth. This must not be too high if the RMF is to penetrate into the plasma and drive current. It has been both observed experimentally and shown through numerical calculations that if $\frac{\gamma}{\lambda} > 1$ the RMF will penetrate the plasma and drive a fully synchronous, rigid-rotor electron current, but for $\frac{\gamma}{\lambda} < 1$ the RMF will be screened out by eddy currents in the plasma, penetration will not occur and no current will be driven [13, 14, 15].

$$\lambda = \frac{r_s}{\delta} \tag{1.13}$$

$$\frac{\gamma}{\lambda} = \sqrt{\frac{2}{\mu_o \eta \omega r_s^2}} \frac{B_\omega}{e n_e} \tag{1.14}$$

Hence, the ratio of γ and λ may be used to identify areas of potential tradeoffs while maintaining the ability to drive current with the RMF. It is interesting to note that, in this case, an increase in plasma resistivity actually decreases the ability of the RMF to penetrate the plasma.

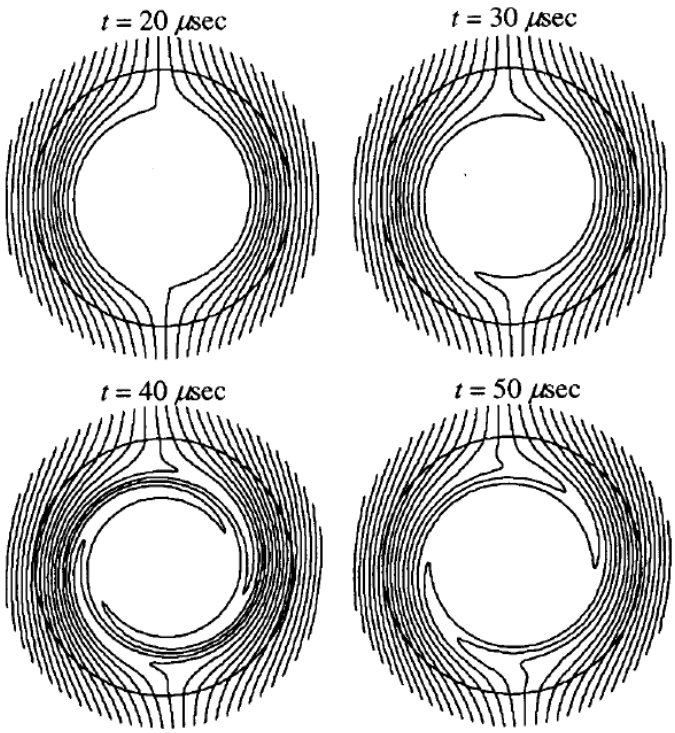

Figure 1.6: A numerical calculation of RMF penetration as a function of time starting with a cold, un-magnetized plasma column [2].

While the above relations are derived for a steady state solution, the formation process in ELF is highly dynamic (see Section 1.6), and the limits of the above restrictions are not clear. However, recent numerical calculations seem to verify the predicted current drive limitations of RMF in a dynamic setting [2].

In ELF, not only is the RMF the primary FRC formation mechanism, but it also is responsible for the majority of the ionization of the neutral gas within the thruster. It was noticed in previous experiments that RMF is a prolific ionizer of neutral gas. An electrodeless ionization source is extremely attractive from the prospective of thermal insulation and thruster lifetime. Thus, the decision was

made that the RMF would pull double duty as the main source of ionization as well as the FRC formation and current drive scheme. This is also an attractive solution from the perspective of current drive since the plasma will be produced on field lines while the RMF is already present and fully penetrated.

1.5 FRC Expansion

An understanding of adiabatic processes in an FRC is vitally important to the study of its dynamics since an FRC is by nature are a closed system. There is keen interest in FRC deceleration and compression in fusion experiments [16, 17] [18], while space propulsion requires a consideration of expansion and acceleration [12].

Consider an FRC initially in radial equilibrium with a small drift velocity (as in position 1 of Figure 1.7). As the FRC approaches section 2 the external axial magnetic field drops allowing the FRC to expand radially. A radial magnetic field is also present which serves to accelerate the FRC through the $\mathbf{j} \times \mathbf{B}$ force, where the azimuthal component of the current interacts with the radial component of the magnetic field to produce a downstream force. This can also be interpreted as a non-uniform magnetic pressure ($p_{mag} = B^2/2\mu_o$) exerted on the FRC at the separatrix. In order to compute the final state of the FRC, it is useful to note that the total energy in the system is conserved throughout the process (assuming various losses like radiation and interaction with the walls are negligible).

Initially (position 1 in Figure 1.7) there is only thermal and magnetic energy (E_{th}, E_B) within the FRC (the initial drift kinetic energy is considered to be

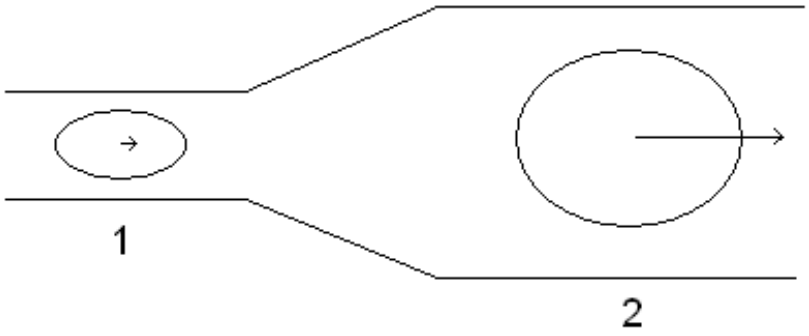

Figure 1.7: Initial (1) and final (2) conditions.

negligible). There is also energy stored in the compression of the vacuum axial magnetic field between the FRC and the flux conserving wall (E_{vac}).

$$E_{total} = E_{FRC} + E_{vac} \tag{1.15}$$

The thermal and magnetic FRC energies are integrated within the volume of the separatrix. The factor of $\frac{3}{2}$ assumes that the particles have three degrees of freedom based on the fact that most of the particles in an FRC are located near the magnetic null.

$$E_{FRC} = E_{th} + E_B \tag{1.16}$$

$$E_{th} = \int \frac{3}{2} nkT \mathrm{d}V \tag{1.17}$$

$$E_{th} = \frac{3}{2} NkT \tag{1.18}$$

$$E_B = \int \frac{B_z^2}{2\mu_\mathrm{o}} \mathrm{d}V \tag{1.19}$$

where N is the total number of particles and T is the species temperature, or conversely N is the total number of ions and T is the total temeperature $(T_i + T_e)$.

Using pressure balance (Equation 1.4), the magnetic energy can be expressed in terms of the pressure and the external field.

$$E_{FRC} = \frac{3}{2}NkT + \int \left(\frac{B_e^2}{2\mu_o} - p \right) \mathrm{d}V \tag{1.20}$$

$$E_{FRC} = \frac{3}{2}NkT - NkT + \frac{B_e^2}{2\mu_o}V \tag{1.21}$$

Using the average of β, the volume can be expressed in terms of the quantities already present in the above expression.

$$\langle \beta \rangle = \frac{\langle p \rangle}{\frac{B_e^2}{2\mu_o}} = 1 - \frac{1}{2}x_s^2 \tag{1.22}$$

$$\langle \beta \rangle \frac{B_e^2}{2\mu_o} \frac{1}{kT} = \langle n \rangle = \frac{N}{V} \tag{1.23}$$

$$V = \frac{NkT}{\langle \beta \rangle \frac{B_e^2}{2\mu_o}} \tag{1.24}$$

This allows further simplification of the expression for the energy within the separatrix.

$$E_{FRC} = \frac{1}{2}NkT + \frac{B_e^2}{2\mu_o} \frac{NkT}{\langle \beta \rangle \frac{B_e^2}{2\mu_o}} \tag{1.25}$$

$$E_{FRC} = NkT \left(\frac{1}{2} + \frac{1}{\langle \beta \rangle} \right) \tag{1.26}$$

The vacuum magnetic energy is equal to the difference in energy between the

configuration of a magnetic field of strength B_e filling the the volume between the separatrix and the wall, and that of an axial field of strength B_o filling the entire volume when the FRC is not present.

$$E_{vac} = E_{B_e} - E_{B_\mathrm{o}} \tag{1.27}$$

$$E_{B_e} = \int \frac{B_e^2}{2\mu_\mathrm{o}} \mathrm{d}V_{ext} = l\pi \left(r_w^2 - r_s^2\right) \frac{B_e^2}{2\mu_\mathrm{o}} \tag{1.28}$$

$$E_{B_\mathrm{o}} = \int \frac{B_\mathrm{o}^2}{2\mu_\mathrm{o}} \mathrm{d}V = l\pi r_w^2 \frac{B_\mathrm{o}^2}{2\mu_\mathrm{o}} \tag{1.29}$$

Using a similar approach as was used to obtain Equation 1.26, the energy in the external field can be expressed as a function of N T, and x_s (keeping in mind that $\langle\beta\rangle$ is a function only of x_s).

$$E_{B_e} = l\pi \frac{r_s^2}{x_s^2} \left(1 - x_s^2\right) \frac{B_e^2}{2\mu_\mathrm{o}} \tag{1.30}$$

$$E_{B_\mathrm{o}} = l\pi \frac{r_s^2}{x_s^2} \left(1 - x_s^2\right)^2 \frac{B_e^2}{2\mu_\mathrm{o}} \tag{1.31}$$

$$E_{vac} = l\pi \frac{r_s^2}{x_s^2} \frac{B_e^2}{2\mu_\mathrm{o}} \left(1 - x_s^2 - \left(1 - x_s^2\right)^2\right) \tag{1.32}$$

$$E_{vac} = NkT \frac{(1 - x_s^2)}{\langle\beta\rangle} \tag{1.33}$$

The total energy of the system (in the initial condition, or position 1 in Figure 1.7)

reduces to a function of N and T.

$$E_{total} = NkT\left(\frac{1}{2} + \frac{1}{\langle\beta\rangle} + \frac{1-x_s^2}{\langle\beta\rangle}\right) \tag{1.34}$$

$$E_{total} = NkT\left(\frac{1}{2} + \frac{2-x_s^2}{1-\frac{1}{2}x_s^2}\right) = NkT\left(\frac{1}{2}+2\right) \tag{1.35}$$

$$E_{total} = \frac{5}{2}NkT \tag{1.36}$$

It is interesting to consider the fractional amount of energy contained within the FRC to the total energy. This can be easily computed using Equation 1.26 and 1.36.

$$\frac{E_{FRC}}{E_{total}} = \frac{NkT\left(\frac{1}{2}+\frac{1}{\langle\beta\rangle}\right)}{\frac{5}{2}NkT} \tag{1.37}$$

$$\frac{E_{FRC}}{E_{total}} = \frac{1}{5} + \frac{2}{5\langle\beta\rangle} = \frac{1}{5} + \frac{2}{5\left(1-x_s^2/2\right)} \tag{1.38}$$

Thus, the fraction of energy within an FRC is always between $\frac{3}{5}E_{total}\left(x_s = 0\right)$ and $E_{total}\left(x_s = 1\right)$. Therefore, in the context of flux compression of an FRC, no more than $\frac{2}{5}$ of the total energy input goes into the compression of the external field.

Alternatively, the energy can be expressed in terms of the length, which is useful in determining the total energy from external measurements, and calculating the pV work.

$$E_{total} = \frac{5}{2}NkT = \frac{5}{2}l\pi r_s^2\langle\beta\rangle\frac{B_e^2}{2\mu_o} \tag{1.39}$$

$$E_{total} = \frac{5}{2}\langle\beta\rangle\frac{x_s^2}{\left(1-x_s^2\right)^2}l\pi r_w^2\frac{B_o^2}{2\mu_o} \tag{1.40}$$

Constant flux wall expansion/compression is another illustrative case to consider, since it is similar to the expansion process occurring in ELF, and current liner compression fusion studies [19].

Starting with the first law of thermodynamics with no heat addition: $\mathrm{d}E + \mathrm{d}W = \mathrm{d}Q = 0$, where $\mathrm{d}W = p\mathrm{d}V$. This can be evaluated by examining the Maxwell stress tensor just inside the tube wall and just past the ends of the FRC.

$$\mathrm{d}W = P_r 2\pi r_w l \mathrm{d}r_w + P_z \pi r_w^2 \mathrm{d}l \tag{1.41}$$

$$\mathrm{d}W = \frac{B_e^2}{2\mu_\mathrm{o}} 2\pi r_w l \mathrm{d}r_w - \frac{B_\mathrm{o}^2}{2\mu_\mathrm{o}} \pi r_w^2 \mathrm{d}l \tag{1.42}$$

$$\mathrm{d}W = \frac{\phi_\mathrm{o}^2}{2\mu_\mathrm{o}} \frac{2\pi r_w l \mathrm{d}r_w}{\left(\pi r_w^2\right)^2 \left(1 - x_s^2\right)^2} - \frac{\phi_\mathrm{o}^2}{2\mu_\mathrm{o}} \frac{\mathrm{d}l}{\pi r_w^2} \tag{1.43}$$

$$\mathrm{d}W = \frac{\phi_\mathrm{o}^2}{2\mu_\mathrm{o}} \frac{l}{\pi r_w^2} \left(\frac{\mathrm{d}r_w}{r_w \left(1 - x_s^2\right)^2} - \frac{\mathrm{d}l}{l} \right) \tag{1.44}$$

Using the volumetric equation for energy, the differential can be computed (A_t is the area of the tube).

$$E = \frac{5}{2} \langle \beta \rangle \frac{x_s^2}{\left(1 - x_s^2\right)^2} \frac{\phi_\mathrm{o}^2}{2\mu_\mathrm{o}} \frac{l}{A_t} \tag{1.45}$$

$$\mathrm{d}E = \frac{5}{2} \langle \beta \rangle \frac{x_s^2}{\left(1 - x_s^2\right)^2} \frac{\phi_\mathrm{o}^2}{2\mu_\mathrm{o}} \left(\frac{A_t \mathrm{d}l - l \mathrm{d}A_t}{A_t^2} \right) \tag{1.46}$$

$$\mathrm{d}E = \mathrm{d}W \tag{1.47}$$

$$\frac{5}{2}\left\langle\beta\right\rangle\frac{x_s^2}{\left(1-x_s^2\right)^2}\frac{\phi_{\mathrm{o}}^2}{2\mu_{\mathrm{o}}}\left(\frac{A_t\mathrm{d}l-l\mathrm{d}A_t}{A_t^2}\right)=\frac{\phi_{\mathrm{o}}^2}{2\mu_{\mathrm{o}}}\frac{l}{A_t}\left(\frac{\mathrm{d}r_w}{r_w\left(1-x_s^2\right)^2}-\frac{\mathrm{d}l}{l}\right) \tag{1.48}$$

$$\frac{5}{2}\left\langle\beta\right\rangle\frac{x_s^2}{\left(1-x_s^2\right)^2}\left(\frac{\mathrm{d}l}{l}-\frac{\mathrm{d}A_t}{A_t}\right)=\frac{\mathrm{d}r_w}{r_w\left(1-x_s^2\right)^2}-\frac{\mathrm{d}l}{l} \tag{1.49}$$

$$\frac{5}{2}\left\langle\beta\right\rangle\frac{x_s^2}{\left(1-x_s^2\right)^2}\left(\frac{\mathrm{d}l}{l}-\frac{2\mathrm{d}r_w}{r_w}\right)=\frac{\mathrm{d}r_w}{r_w\left(1-x_s^2\right)^2}-\frac{\mathrm{d}l}{l} \tag{1.50}$$

$$\frac{\frac{5}{2}\left\langle\beta\right\rangle x_s^2+\left(1-x_s^2\right)^2}{2\frac{5}{2}\left\langle\beta\right\rangle x_s^2+1}\frac{\mathrm{d}l}{l}=\frac{\mathrm{d}r_w}{r_w} \tag{1.51}$$

$$l^{\frac{\frac{5}{2}\left\langle\beta\right\rangle x_s^2+\left(1-x_s^2\right)^2}{2\frac{5}{2}\left\langle\beta\right\rangle x_s^2+1}}r_w=const \tag{1.52}$$

If the profile and total flux within the FRC are constant throughout the process (which is in accorance with observations [1]), then the x_s is also constant.

The scaling derived above is useful for static expansion or compression, however, the expansion which takes place in ELF also serves to accelerate the FRC. The total energy is then the sum of the thermal and magnetic energies within the FRC, the energy of the compressed bias field, and the kinetic energy of the plasma.

$$E_{total}=\frac{5}{2}NkT+\frac{1}{2}Nm_iv^2 \tag{1.53}$$

Equating the energy at position 1 to that at position 2 (in Figure 1.7).

$$\frac{5}{2}NkT_1=\frac{5}{2}NkT_2+\frac{1}{2}Nm_iv_2^2 \tag{1.54}$$

$$v_2=\sqrt{\frac{5}{m_i}(kT_1-kT_2)} \tag{1.55}$$

The details of the conversion depend on the specific expansion under consideration

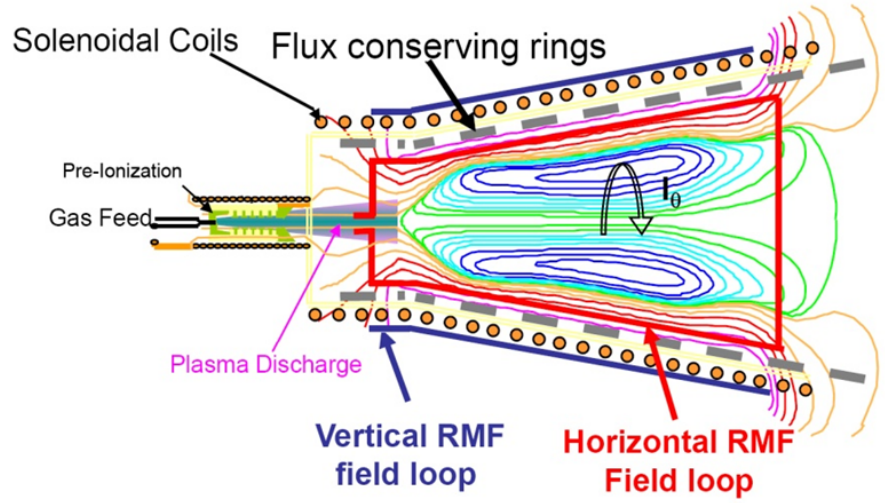

Figure 1.8: Operation of the ELF thruster.

(such as nozzle shape). However one can measure the efficiency of the expansion process by measuring the temperatures (or size of the plasma) before and after the expansion.

1.6 The ELF Thruster

As stated earlier, the ELF concept is to generate thrust through the rapid formation and ejection of high velocity FRC plasmoids. Rotating magnetic fields are utilized to simultaneously ionize neutral propellant and form an FRC in a diverging axial bias magnetic field which imparts a net downstream force on the plasmoid through the $\mathbf{j} \times \mathbf{B}$ interaction. As the FRC translates downstream, it also expands, converting some of the plasma thermal energy to directional energy (similar to a gasdynamic nozzle), resulting in the ejection of a fast, cold plasmoid.

The experimental version of the ELF thruster consists of a quartz cone (roughly 50 cm in length with an average radius of 10 cm) with segmented copper flux conservers beneath a solenoidal wire magnet wound directly on to the sides of the cone and two pairs of copper strap RMF antennae (2 vertical and 2 horizontal) mounted directly atop the solenoidal magnet (see Figures 1.8 and 1.9). The upstream (small) end of the cone contains a small magnetoplasmadynamic arc (MPD) which serves both to introduce neutral gas into the cone (via a fast puff valve) and to provide a small amount of seed plasma in order to facilitate the RMF breakdown of the neutral gas (the MPD is henceforth referred to as the pre-ionization system, or PI). A straight cylindrical quartz section (with additional flux conservers and solenoidal magnets) is mated to the small end of the cone to provide additional room for the axial movement of the PI. There is also an additional wire magnet wound around a separate PVC ring near the small end of the cone which is axially adjustable to provide additional bias field near the PI. The large end of the cone exhausts into a large quartz chamber (80 cm in diameter $\times$ 1.25 m in length) which is meant to simulate space. There is, however, a small amount of bias field present in the drift chamber (provided by a separate magnet system) to facilitate the study of the plume. The RMF system in ELF consists of an RF excitation source (square wave), inductively coupled via a 1:1 transformer with an oscillating LC tank circuit consisting of a high voltage capacitor and the RMF antennae.

Due to experimental constraints, the vast majority of the testing of ELF was characterized by the formation and ejection of a single FRC. The intended operation is, as previously stated, the repeated formation and ejection of multiple

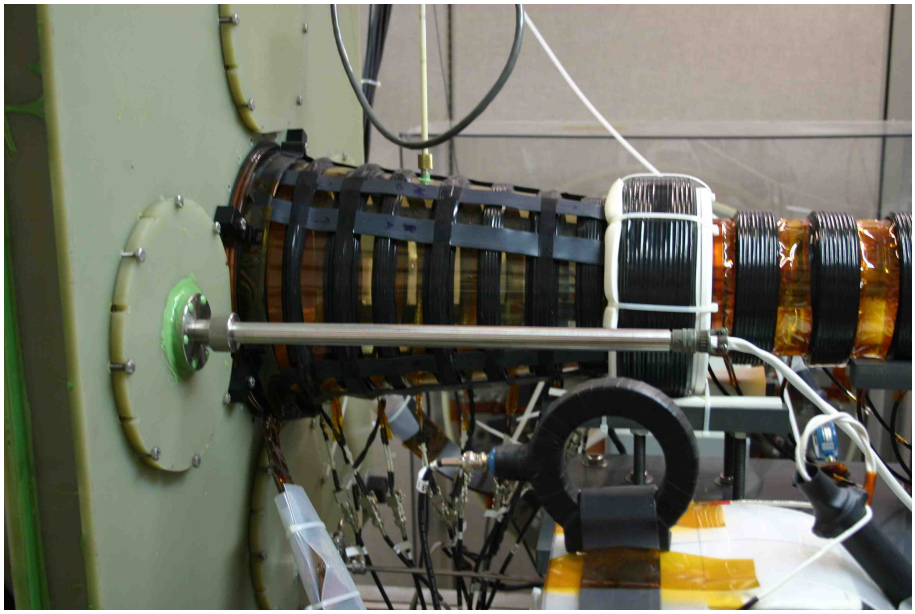

Figure 1.9: Photograph of the ELF thruster experiment.

FRCs in quick sucession. Due to the pulsed repetitive nature of the thruster and limited confirmation with multiple-FRC tests, initial testing and development of the thruster could be performed with a reasonable degree of confidence that the single-shot behavior which was observed would be representative of one pulse of repetitive operation.

The operation of ELF during testing consisted of three main stages: pre-formation, formation, ejection. The bias fields, neutral gas puff, and pre-ionization are all initiated during the pre-formation stage. The initiation and duration of the RMF induced formation process constitutes the formation stage, and the ejection stage consists of the axial translation, expansion, acceleration, and ejection of the FRC from the cone into the drift chamber.

The following describes the operation of the ELF thruster in “single shot mode”,

as it was tested for the majority of the experimental investigation. First the bias coil is fired, this magnetic field is slow to rise so it must be fired first if it is to reach peak value during the formation and ejection phases. It is envisioned that this would be a relatively steady field during multiple discharge operation. The bias field is slow enough that it completely soaks through the flux conservers lining the formation section. The flux conservers are of a thickness to allow magnetic fields to soak through on long timescales (such as the bias fields), but to act as flux conservers over the shorter timescales of formation and ejection. Several milliseconds after the bias is initiated, the puff valve within the PI is opened (for a duration of several hundred microseconds) initiating a flow of neutral gas between the electrodes of the PI, and into the formation section. Several hundred microseconds later the PI is triggered, initiating an arc between the electrodes, and accelerating a small amount of plasma into the cloud of neutral gas which is slowly translating across the formation section (this concludes the pre-formation phase of operation). Tens of microseconds after the triggering of the PI, the RF excitation of the RMF system is initiated, and the RMF begins to increase in amplitude (over tens of oscillations, $f_{RMF} = 242$ kHz). When the RMF amplitude grows large enough, the the neutral gas is ionized, diamagnetic current is driven in the plasma, and an FRC begins to form. As the driven current increases (the FRC gaining energy), the circulating energy in the tank circuit quickly decreases. As the energy in the tank approaches zero, and the amplitude of the RMF gets small, the RF excitation source is disengaged and the formation phase ends. When the FRC has grown to fill most of the cross sectional area of the formation section, the axial bias field becomes compressed against

the flux conservers at the wall, the pressure on the separatrix increases, and the FRC feels a downstream acceleration force. As the FRC translates downstream, it expands and accelerates, decreasing in temperature. This process continues even after the plasmoid has left the thruster, since the magnetic field continues to diverge strongly in the immediate vicinity of the exit. Eventually the FRC leaves the region of the diverging field as a cold, fast plasmaoid.

1.7 ELF Advantages

The present ELF thruster is aimed at power levels of $10 - 100$ kW and above, with exhaust velocities of $15 - 40$ km/s ($I_{sp} = 1500 - 4000$ s). These goals were set in accordance with the predicted increase in power generating capability in space over the next several years. ELF was designed from the beginning to be a high power ($\sim$ 1 MW) plasma thruster; however, to effectively compete against variants of current thruster technology (such as high power Hall thrusters), it was considered a priority to attempt to develop ELF at a power level just above the capabilities of current established technologies.

Currently, Hall thrusters are the dominant type electric propulsion device used in cis-lunar space. The typical Hall thruster is only capable of operation several kilowatts, however, higher-power variants (tens of kilowatts) are under development. Projections for Hall thruster scaling (see Figure 1.10) estimate that the power level and the thruster mass scale with the cross sectional area of the thruster. In addition, the magnetic system consists of a large iron core, is typically $75 - 80$ %

of the total thruster mass, and the scaling is unlikely to improve with further technological development. The thrust/weight ratio of the ELF thruster is expected to be at least an order of magnitude greater than Hall thrusters of equal power (based on the current experimental thruster and the elimination of unnecessary mass).

At a linear power scaling of 0.5 kW/kg, a 100 kW Hall thruster is expected to weigh $\sim$ 200 kG [3]. This estimate does not include the power processing unit (Hall thrusters require carefully regulated power) which is typically on the order of the thruster mass. ELF is estimated to be capable of operation at power levels greater than 100 kW at a mass of $\sim$ 5 kg, resulting in a scaling of 20 kW/kg. This puts the Hall thruster 195 kG heavier than the ELF thruster (20$\times$ heavier than ELF), and several times the size. If this mass difference were used to fly additional solar panels (Ultraflex panels at $\sim$ 200 W/kg, for example), the resulting increase in spacecraft power generation would be $\sim$ 40 kW. Considering that ELF essentially does not need a power processing unit (unregulated power works fine for charging capacitors), the estimate for additional spacecraft power roughly doubles, approaching the total power consumed by the thruster.

An alternative way to consider the situation is that ELF does not need to be very efficient in order to compete against a Hall thruster at a power level of 100 kW. At higher power levels, the advantage of an ELF-like thruster becomes even more dramatic. Unlike the established thruster types, ELF was designed to be capable of operation at high power levels, and there is no inherent thrust density limit to the operation of the thruster. However, in order to facilitate the development of an ELF-like thruster, it is desirable to maximize the efficiency in order to produce

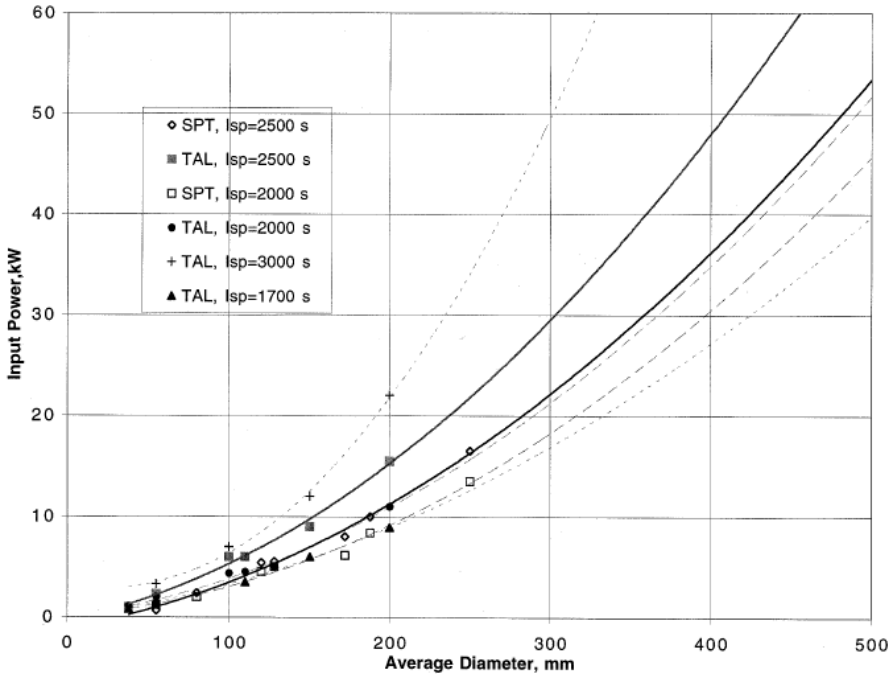

(a) Hall thruster size and power scaling.

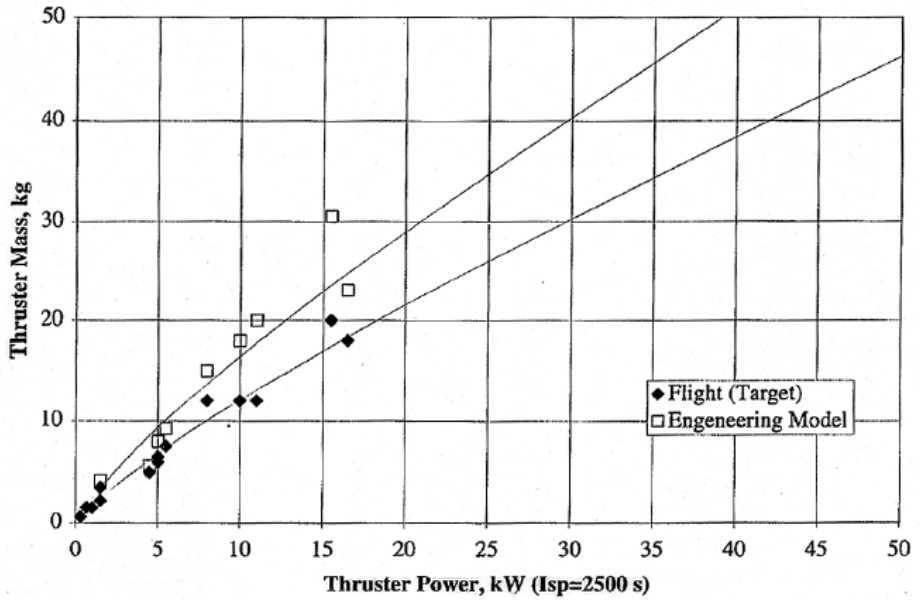

(b) Hall thruster mass and power scaling.

Figure 1.10: Projected Hall thruster scaling based on current experimental thrusters and estimated development [3].

a thruster which is competitive at the lower (more common) power level of tens of kilowatts.

In addition to the previously mentioned advantages of a pulsed plasmoid propulsion scheme (extreme power scalability, and no magnetic detachment issues, see Section 1.2), there are several qualities inherent to the ELF design which are extremely attractive in a space thruster.

Since the ionization, formation, and acceleration process is completely electrodeless and takes place within an axial magnetic bias field, there is virtually no plasma contact with the surfaces of the thruster. This prevents thermal losses to the thruster walls, as well as wall sputtering, plume contamination, catalyzed propellant recombination, and essentially all loss mechanisms except for radiation. There is also no inherent limit on the operational lifetime of the thruster since there are no erosion issues, and all switching components are solid state.

Another characteristic of ELF, which may prove to be very attractive from a mission design standpoint, is that the operation of the thruster is essentially propellant independent. Since the RMF drives electron current while leaving the ions unaffected, the current drive process can remain unchanged regardless of the atomic species used. Also, since all the propellant is ejected as a coherent plasmoid, only the aggregate mass and velocity is of propulsive interest. Thus there is no need to operate in a heavy gas to obtain desirable exhaust velocities (although a heavy gas may offer potential mass per ionization-energy advantages). As will be presented in Chapter 3, the current ELF thruster has demonstrated that it is capable of forming and ejecting an FRC using virtually any gaseous propellant

(including waste gases, complex combustion by-products, and in-situ resources). Additional thruster system mass savings could be affected by the use of easily storable liquid propellants (such as propane, which could also serve as a secondary energy source), thus alleviating the added mass and cost associated with operation in xenon.

In addition, an ELF-type thruster could serve as the basis of an air-breathing thruster design. This capability would enable a variety of exotic missions including high altitude air-breathing hypersonic flight, high altitude to orbit flight, drag mitigation for low orbits, the flight of highly eccentric orbits with powered thrust at perigee, and the atmospheric collection of propellant for refueling purposes.

Chapter 2

Experimental Setup

This chapter outlines the physical characteristics of the ELF experiment including the vacuum system, magnet and RMF systems, gas-feed and pre-ionization systems, the data acquisition system, and the diagnostic equipment. The experiment described is the current version of ELF (ca. late 2009), prior to that earlier configurations of ELF were tested. Changes leading to the current configuration were performed in the interest of improving experimental flexibility, thruster performance, and diagnostic accuracy.

2.1 Vacuum Sytem

There are two main sections of the vacuum system on the ELF experiment: the thruster and the drift chamber. The thruster section consists of a 46 cm long conical section and a 42 cm long cylindrical section 14 cm in diameter, both made

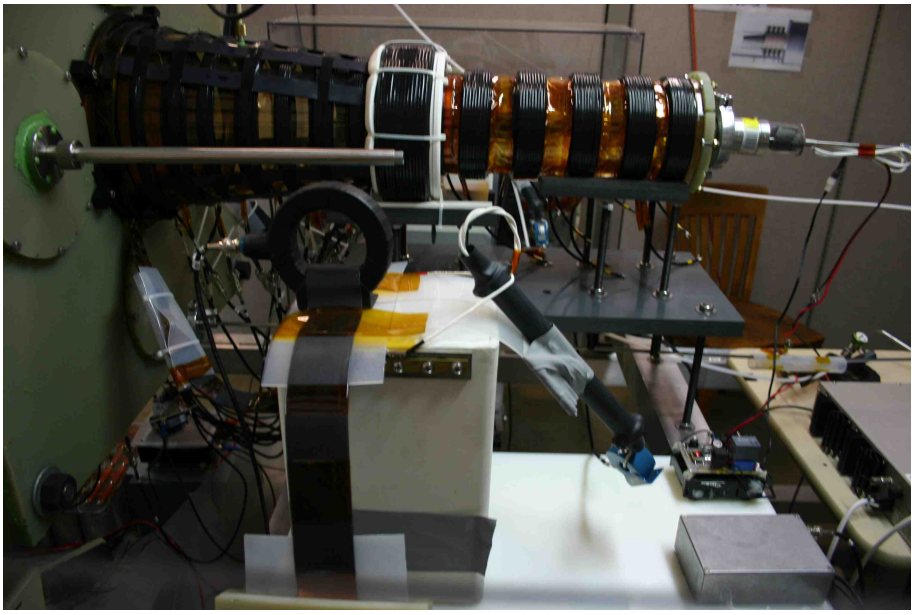

Figure 2.1: Side view of the thruster section of the vacuum boundary.

of clear fused quartz (see Figure 2.1).

The cylindrical section is capped on the upstream side by a circular plate of G-10/FR-4 Garolite fiberglass, sealed with a greased O-ring (Buna-N O-ring and Apieson grease), and held in place by a groove machined in the G-10. Bolts are tightened into bolt-holes machined into the G-10 just outside the outermost diameter of the quartz in order to hold the fiberglass in place while the experiment is not under vacuum.

An NW50 vacuum feed-through port is installed in the center of the fiberglass plate for the insertion of the MPD pre-ionization (PI) source/gas feed (see Section 2.3). The PI is mounted within a quartz cylinder 60 cm in length and 4.5 cm in diameter. The seals are formed at the downstream end of the PI cylinder (near the electrodes) and at the NW50 flange in the G-10 plate (the interior of the PI

cylinder is not under vacuum), with the seal at the NW50 flange is formed between the flange and the quartz PI cylinder (the O-ring is supported by the quartz, not an O-ring keeper). The O-ring is compressed against the flange and the cylinder with a steel annulus (the same dimensions as the lip of the NW50 flange) and a clamp. Immediately outside this seal, a rubber-lined double hose clamp is attached to the PI cylinder to prevent it from being sucked into the chamber by vacuum forces.

A $\frac{1}{4}$ inch quick-disconnect feed-through is mounted at a radius of 6.5 cm (just inside the inner diameter of the cylindrical quartz section), this feed-through is currently unused but could provide diagnostic access to the thruster section from the upstream side. A greased O-ring is held in a groove machined into the lip of the downstream end of the 42 cm cylindrical quartz section, which provides a seal between the cylindrical and conical pieces of the thruster section that is held together with vacuum forces. There is a $\frac{1}{4}$ inch quick-disconnect installed 25 cm downstream of this interface to provide diagnostic access to the plasma and is currently housing an internal magnetic field probe.

The drift chamber consists of a large Rotosil chamber, 80 cm in diameter (see Figure 2), with G-10 walls on both sides (upstream and downstream), and several $\frac{1}{4}$ inch Quick Disconnect vacuum feed-throughs installed along the length (at 54, 94, and 132 cm downstream of the cone-cylinder interface). The upstream wall is 7.5 cm thick with 5 large holes: one above, below, and on either side of a large center hole (see Figure 2.2). The cone is secured to the center hole with claw clamps and sealed with a greased L-gasket. The other four holes sealed with G-10 plates

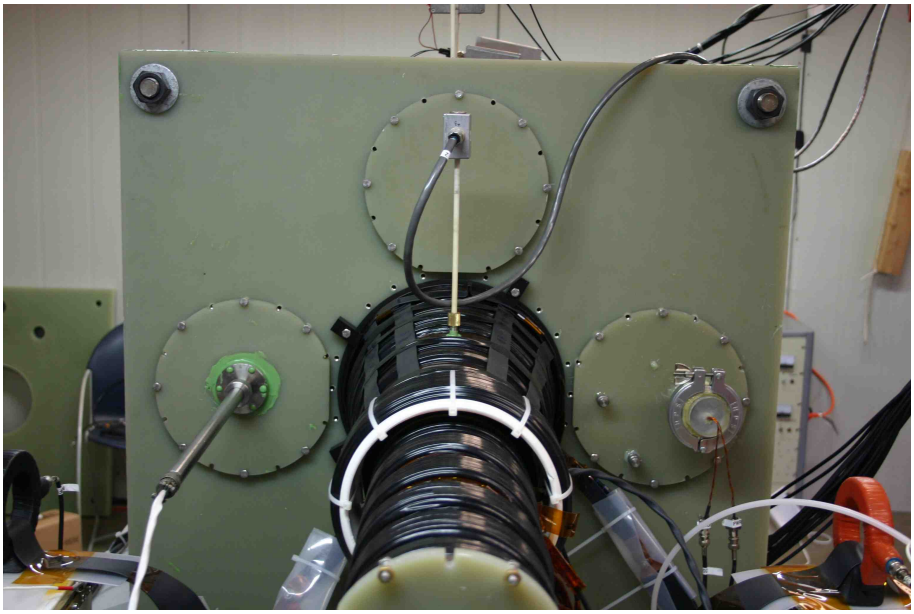

Figure 2.2: Front view of ELF vacuum system.

bolted over greased L-gaskets. The left (when looking downstream) plate has a $\frac{3}{4}$ inch Quick Disconnect vacuum feed-through through which the Fast Ion Gauge (see Section 2.6.2) gains access to the chamber. The bottom plate is furnished with a $\frac{1}{4}$ inch Quick Disconnect occupied by the 90° Langmuir probe which was used for initial analysis, but not for any of the data presented in this thesis. The right plate has an NW50 flange capped with a polycarbonate slug that feeds the electrical connections to the pendulum used for thrust measurements (see Section 2.6.7). The top plate has nothing installed in it.

Four 1 inch threaded rods compress the G-10 walls against the 80 cm quartz drift tube, with greased L-gaskets forming a seal between the walls and the ends of the tube. There is a hole in the center of the downstream wall onto which is bolted an 6-way steel cross (see Figure 2.3). There is a greased O-ring compressed between

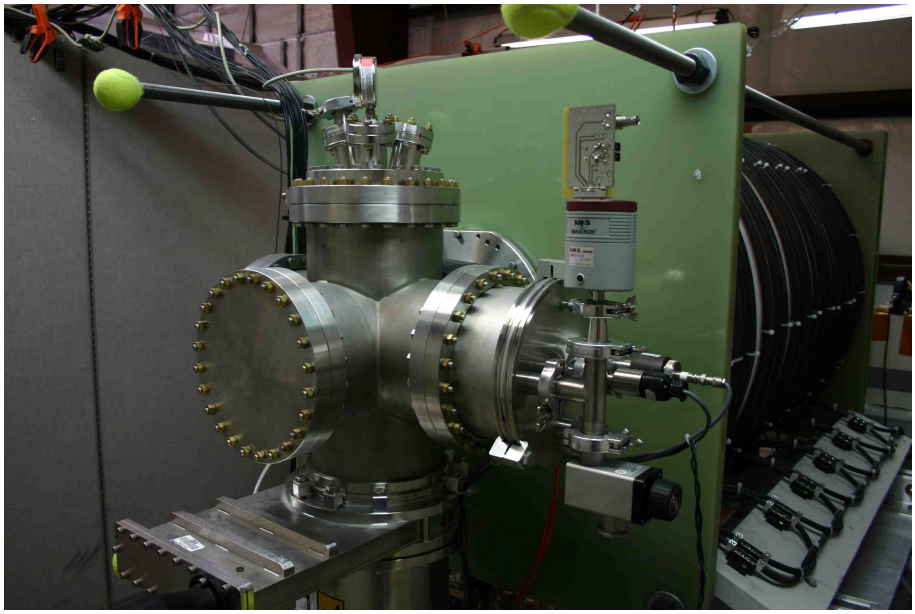

Figure 2.3: Back view of ELF vacuum system.

cross and the downstream wall to form a seal. Attached to the sides and top of the cross are several vacuum measurement instruments are attached (described below). On the bottom of the cross is a mechanical gate valve used to form a temporary seal between the pumps and the chamber.

Mounted to the bottom of the gate valve is an Osaka TG1113MBW-09 turbo-molecular pump controlled by an Osaka TD711/1111-C turbo controller. Attached to the output of the turbo-pump is an Edwards ESDP12 oil-less scroll pump, which exhausts into the laboratory.

The experiment is physically supported in two locations on the 80 cm drift tube, along the two lower over-bolts, and along the cylindrical thruster section. The thruster section and the drift section each sit atop a carriage that is free to roll along a set of rails mounted to an aluminum frame.

There are several instruments used to monitor the quality of vacuum in the experiment. During the initial pumping of the system (when the turbo-pump is still off) a mechanical pressure gauge is used provide a rough estimate of the pressure, when this reaches the limit of its sensitivity the Televac vacuum monitoring system is switched on. The monitoring system consists of a Televac MM200 Dual Display attached to two Televac 2A thermocouple gauges and a Televac 7E1 cold cathode gauge. The first thermocouple is used to measure the remaining pressure in the chamber and serves as an indicator of when to turn the turbo-pump on (after the turbo-pump is turned on, the pressure drops below the gauges limit of sensitivity). The second thermocouple monitors the pressure between the turbo-pump and the scroll pump. The cold-cathode is used to monitor the pressure in the main chamber after the turbo-pump has been turned on. The ELF vacuum system is capable of sustaining a vacuum of roughly 5×10^{-7} Torr.

Also attached to the cross is a Stanford Research Systems Residual Gas Analyzer 100 (RGA), which is used to determine the constituents of any remaining gas in the chamber. This is useful in detecting leaks and other factors that could lead to less than adequate vacuum. One of the main limitations of the ELF vacuum system is that many of the components of the experiment can absorb moisture from the atmosphere and release it slowly when under vacuum resulting in higher than normal pressure in the chamber. While most of this excess moisture is eventually pumped away (over the course of several days), it can initially seem like a leak. The RGA can be used to determine what fraction of the pressure is attributable to water, and what is attributable to leaks. In addition, the RGA can be used to

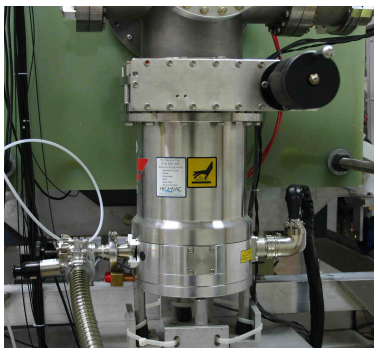

(a) Turbo-pump.

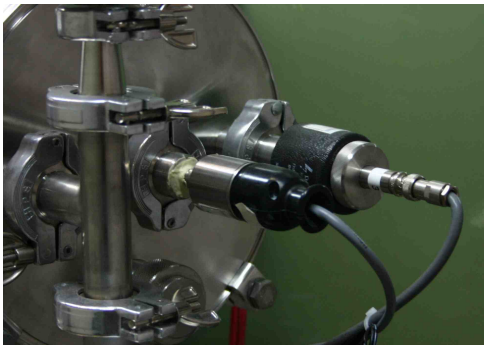

(b) Thrmocouple and cold cathode.

(c) Scroll pump.

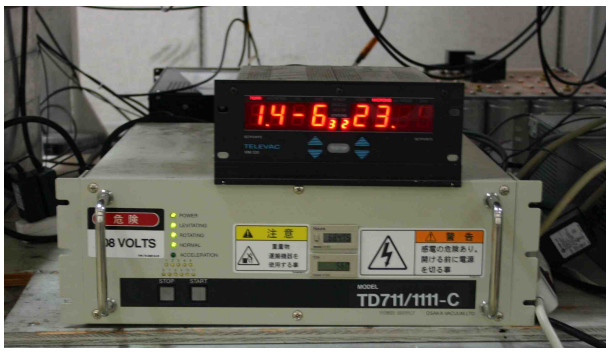

(d) Turbo-pump controller and Televac vacuum monitoring system.

(e) Residual gas analyzer.

Figure 2.4: Various hardware associated with the ELF vacuum system.

detect leaks by spraying a gas not found in the atmosphere (helium in this case) over parts of the experiment and watching for a rise in the partial pressure of that gas.

2.2 Bias System

The slow axial bias fields in ELF are created with several wire-wound magnets: one on the thruster section (cone and small cylinder), another on the drift section, and a third that can move axially over the electrodes of the PI (called the cone, drift, and adjustable biases respectively). As stated in Section 1.3, the FRC is created in a steady axial bias field and expands to compress that field against a flux-conserving boundary. The design of the boundary must be such that axial flux is conserved on the timescales of the FRC formation and translation ($10-100$ of μs) while still allowing the RMF and the axial bias fields penetrate into the chamber. To achieve this, the flux conserver is segmented into rings (to allow the short-timescale non-axial RMF fields to penetrate) of the appropriate thickness that the L/R time of the flux conserver is longer than the FRC growth and translation timescales, but not so long that it is impractical to create a bias field that will soak through.

An estimate for the inductance of the flux conserver can be obtained using the formula for the inductance of a long solenoid and a correction factor (on the order of unity) for finite length, where K is the finite length Nagaoka correction factor (roughly 0.8 in this case), r_c is the average radius of the flux conserver, and l is the

length of the section (the number of turns is 1).

$$L_c = \frac{\mu_o \pi r_c^2 K}{l} \approx \frac{\pi r_c^2}{l} \left(10^{-6}\right) \tag{2.1}$$

The characteristic resistance can be computed using the summed cross sections of the flux conservers and the average length. A_{fc} is the combined cross sectional area of the flux conservers, and η is the conductivity of the flux conserver (Copper: $\eta = 16.78$ nΩ-m).

$$R_c = \frac{2\pi r_c \eta_c}{A_c} \tag{2.2}$$

These combine to yield an approximate timescale for the conservation of flux (τ_c).

$$\tau_c = \frac{L_c}{R_c} = \frac{r_c A_c}{2\eta_c l} \left(10^{-6}\right) \tag{2.3}$$

The bias magnets on ELF were designed using a complete elliptic integral magnetic field solver. This was necessary to design the cone bias in such a way that the magnetic field lines were parallel to the wall of the cone (see Figure 2.5). Once the placement of the magnets and relative number of turns was determined, more or less windings could be added (while keeping the relative number of turns between magnets constant) which changes the inductance and resistance of the magnet. It must be kept in mind that the current required to produce the desired bias field must not exceed the limits of the switch or any other component in the bias system.

The rise time of the bias field must be longer than the characteristic flux conservation timescale. This can be calculated with knowledge of the inductance and

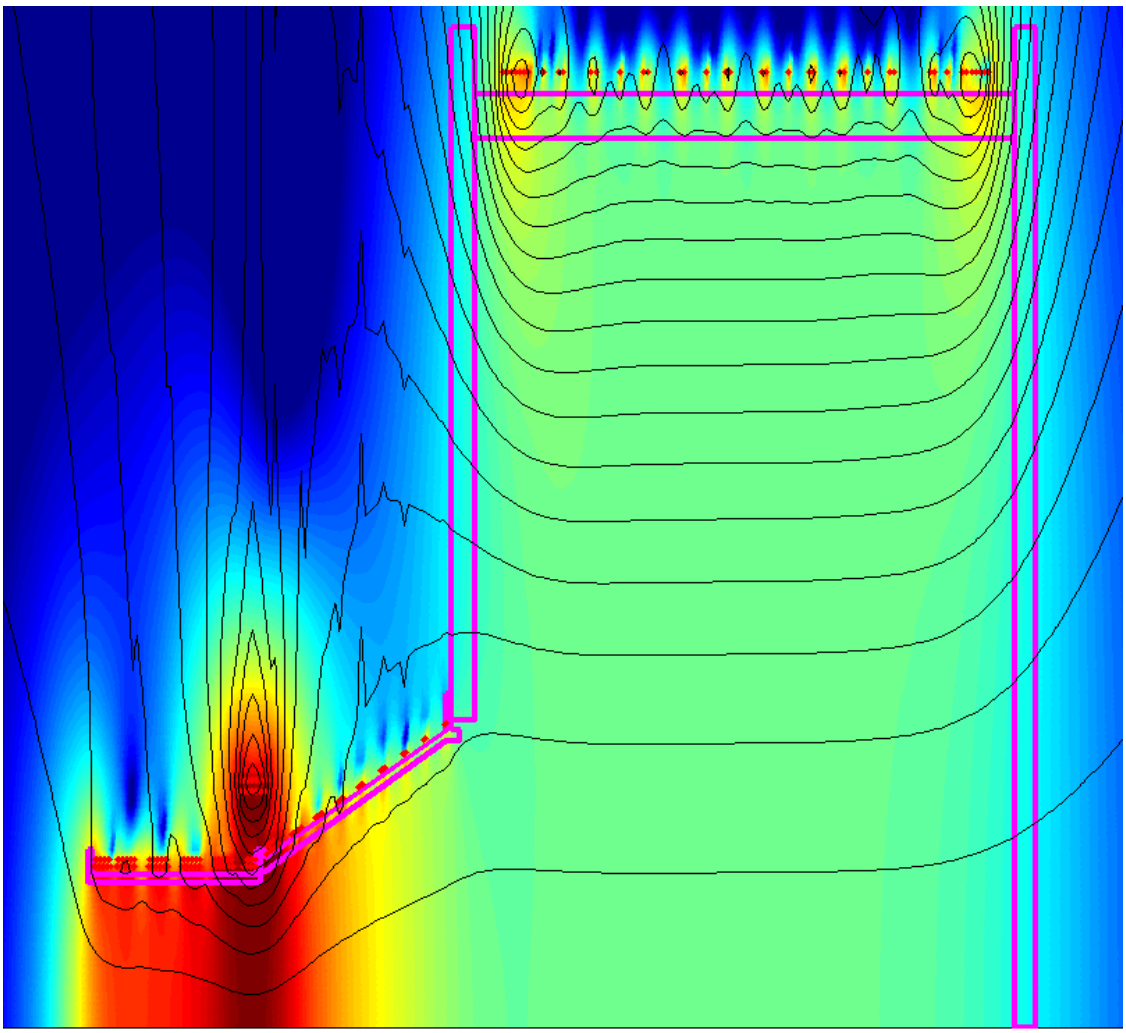

Figure 2.5: Output of ELF bias field solver.

capacitance of the bias system. The inductance can be calculated with a similar manner to Equation 2.1, where r_{mag} is the average radius of the magnet, and N is the number of turns.

$$L_{mag} = \frac{\mu_o N^2 \pi r_{mag}^2 K}{l} \tag{2.4}$$

The rise time is simply the quarter cycle time of the magnet and capacitor bank (C is the capacitance of the bank).

$$\tau_{1/4} = \frac{\pi}{2}\sqrt{L_{mag}C} \tag{2.5}$$

The bias fields on ELF are all equipped with a stack of crowbar diodes (see Figure 2.6), which allows the current to continue circulating after the first quarter cycle. The timescale at which this current dissipates is referred to as the crowbar time.

$$\tau_{cb} = \frac{L_{mag}}{R_{mag}} \tag{2.6}$$

The resistance of the magnet can be computed using the specified resistance per unit length of the wire gauge of the magnet multiplied by the length of wire used (e.g. 4 AWG wire is 292 $\mu\Omega$/ft).

Each magnet is powered a separate bank of electrolytic capacitors, for which the capacitance is chosen to provide the appropriate current over the appropriate timescales. Though the capacitance values are different, the overall design of each bank is similar (see Figure 2.6).

The capacitance values of the electrolytic banks were designed to be: 16 mF

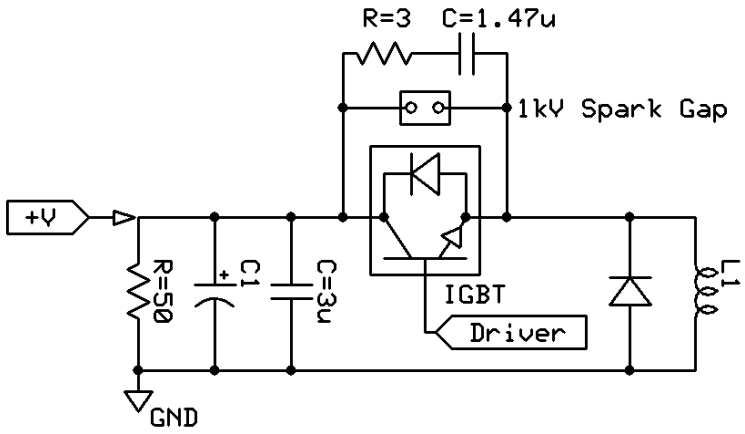

Figure 2.6: Schematic of the capacitor banks for the cone, drift, and adjustable bias systems.

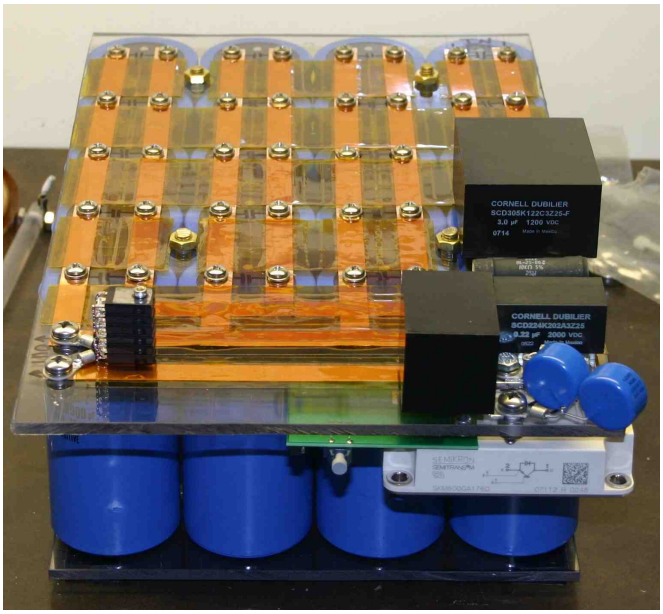

Figure 2.7: Electrolytic capacitor bank and switching setup for the bias systems.

Figure 2.8: The ELF pre-ionization system.

for the cone bias, 20.4 mF for the drift bias, and 15.6 mF for the adjustable bias.

2.3 Pre-Ionization System

The pre-ionization (PI) system in ELF serves two purposes: to introduce neutral gas into the thruster, and to supply an initial amount of seed plasma, which helps the RMF to breakdown the majority of the neutral gas. The PI is not intended to provide a significant amount of energy for either the ionization or acceleration of the gas, that is the purpose of the RMF.

Gas is introduced to the system through a Parker-Hannifin Series 9 (SN 9S3-A2-P1-9B06) fast puff valve driven with a Pulse Power Solutions PUFFDRV2 Fast Puff Valve Driver operating at 600 V. After leaving the puff valve, gas flows through a short passage, between the electrodes of the plasma source, and emerges into the

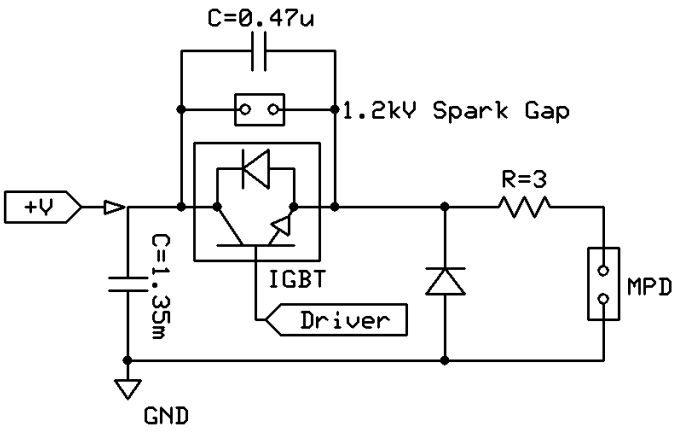

Figure 2.9: Circuit diagram of PI system.

thruster section of the experiment. The energy to power the discharge comes from a bank of capacitors (1.35 mF) located beneath the experiment. The capacitors are switched with a Semikron SKM 800GA176D IGBT capable of delivering a short pulse of power to the electrodes (these switches are also used on the RMF supply and the bias field supplies). A 3 Ω resistor is in line with the plasma so the electrode voltage can remain high, but the current/energy in the discharge can remain low.

The plasma source is a magnetoplasmadynamic arc (MPD) [20] with a long tungsten cathode and a diverging copper anode. Several electrode geometries were tested, and it was determined that, in order for the RMF to efficiently breakdown and initiate an azimuthal current, it is important to have a uniform axi-symmetric discharge (see Section 3.1). In order to achieve a uniform discharge at the relatively low gas flow and power levels required, the electrodes need to be small and closely spaced (see Section 3.1). This enables higher particle and current densities, which provide for a more uniform discharge. The present electrode geometry has a small

throat, with a higher local density and a small inter-electrode spacing to initiate a uniform discharge in a low gas-flow, low power conditions. The long cathode and diverging anode allow the discharge to expand in a way that the $\mathbf{j} \times \mathbf{B}$ force has an outward radial component. The result is a uniform, divergent plume that improves the initial operation of the RMF.

The electrodes are located at the end of a long quartz cylinder that runs the length of the cylindrical portion of the thruster section (see Figure 2.8). This design allows for the maximum amount of flexibility in the axial position of the plasma source. The puff valve is located as near to the electrodes as possible in order to provide as sharp leading edge to the gas pulse as possible (testing with the Fast Ion Gauge revealed that, during "single shot" mode, the thruster operates only on the leading edge of the gas pulse, see Section 3.3). In order to adjust the density in the thruster section without introducing unwanted gas into the drift chamber, the leading edge of the gas pulse needs to be as steep as possible.

The puff valve is located in a region a region of the experiment with a high, low frequency magnetic field. This was interfering with the operation of the valve, thus, the valve needed to be shielded. The frequency was too low to use image currents in a conductor, so a shield was constructed out of ferrite iron (see Figure 2.10). This attenuates the field enough that the operation of the valve is not affected by the bias.

Testing also revealed that the neutral gas has a tendency to flow behind the PI into the small cylindrical section upstream of the cone. In order to prevent this from occurring, a PVC shield was installed just upstream of the electrodes. The

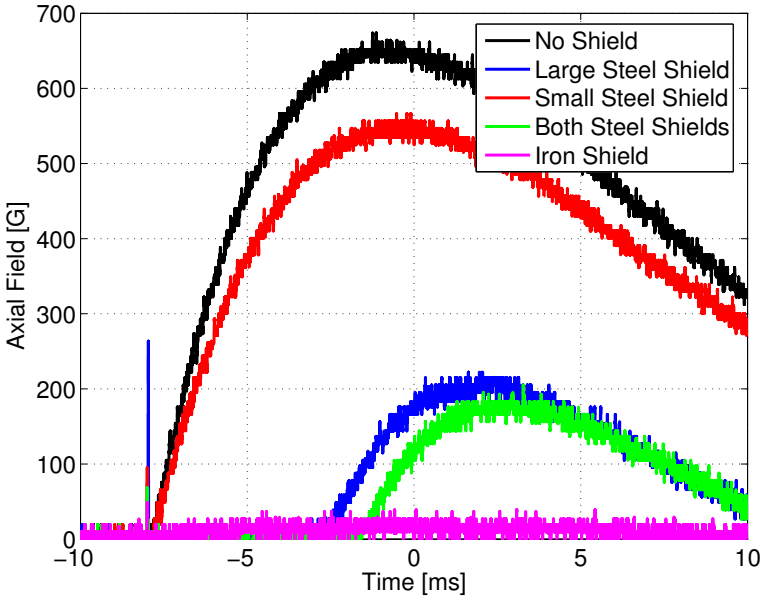

Figure 2.10: Comparison of the axial magnetic field within various shields.

shield has the ability to slide within the cylindrical section to maintain its relative position to the PI during testing at various axial positions.

2.4 RMF System

The RMF system on ELF consists of two identical systems corresponding to the orthogonal directions of the RMF field. Figure 2.11 shows a configuration similar to that of the RMF antennae on ELF (the figure depicts a cylinder for clarity, however the configuration of ELF is conical). Two Helmholtz-like pairs of antennae are mounted to the side of the cone in an orientation such that they produce perpendicular magnetic fields transverse to the axis of the experiment.

These antennae (in series with each other) are connected in series with a trans-

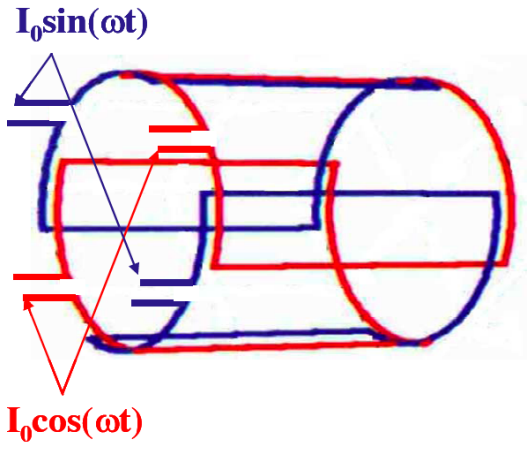

Figure 2.11: Layout of RMF antennae in a Helmholtz-like configuration.

former and a high Q capacitor to form an oscillating LC circuit (see Figure 2.13). This circuit is excited by pulses through the transformer by an RF source located along the sides of the experiment (see Figure 2.12a). The phase of the current in the antennae is offset by 90°, resulting in a steady transverse rotating magnetic field. The RF source consists of 12 parallel channels of identical electrolytic capacitors, snubber circuits, and high-speed solid state IGBT switches (the same Semikron switches used in the other systems). The switches are driven by a custom driver and triggered via optical fiber by a Quantum Composer 9514+ high speed pulse generator. The duration, frequency, and number of pulses is set on the pulse generator, with the start of the sequence triggered by TTL pulse from the CAMAC system (see Section 2.5).

Previous RMF experiments studying FRC sustainment via RMF have utilized a parallel tank circuit configuration [21] (see Figure 2.14b). The impedance of the tank circuit as seen by the RF source can be expressed as the parallel sum of the

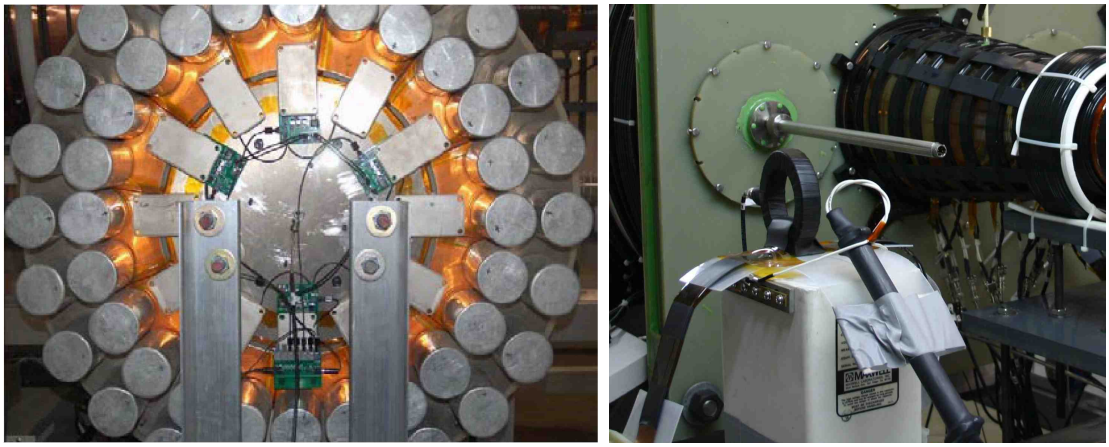

(a) RF Source. (b) Tank circuit.

Figure 2.12: Photographs of RMF system.

impedances of the capacitor and the inductor (which is frequency dependent).

$$Z_p = \left(Z_C^{-1} + Z_L^{-1}\right)^{-1} \tag{2.7}$$

$$Z_p = \frac{i}{\frac{1}{\omega C} - \omega L} \tag{2.8}$$

This configuration is optimal for steady state sustainment, since the tank circuit acts as a band-stop filter, when there is no plasma present, and if the RF excitation is at the characteristic frequency of the tank circuit, the RMF is maintained at very low amplitudes. However, when there is an FRC present, it alters the impedance of the circuit via transformational coupling to the circuit, resulting an a shift in the characteristic frequency of the tank. Since the RF source is no longer within the stop-band of the tank, more power is drawn until the limit of the supply is reached.

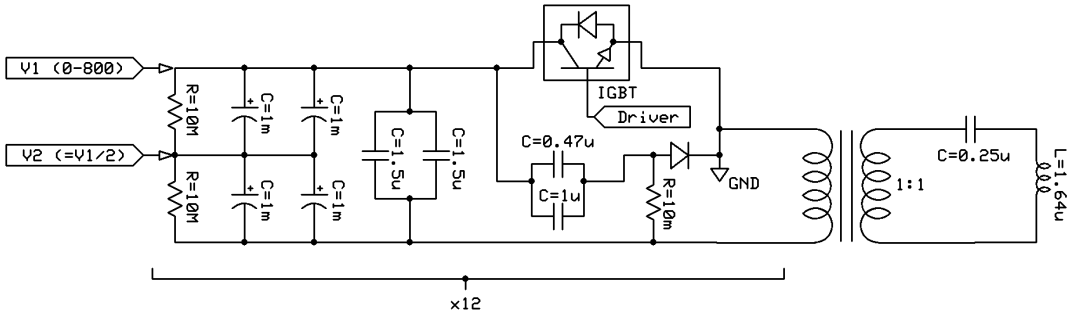

Figure 2.13: Circuit diagram of the RMF system.

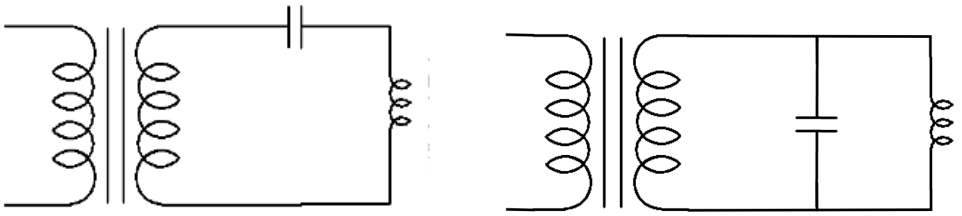

(a) Series. (b) Parallel.

Figure 2.14: Series vs. parallel tank circuits (right side of Figure 2.13).

ELF utilizes a series tank configuration (see Figure 2.14a) in which the impedance seen by the RF source is the series sum of the impedances of the circuit components.

$$Z_s = Z_C + Z_L \tag{2.9}$$

$$Z_s = i\left(\omega L - \frac{1}{\omega C}\right) \tag{2.10}$$

In series, the tank acts as a band-pass filter, and the RF source is tuned to the center of the pass-band. This has the effect of drawing as much power as possible into the tank circuit when there is no plasma present and de-tuning the tank when there is an FRC.

While the parallel tank may be the best choice for RMF sustainment, ELF utilizes a pulsed scheme. Prior to formation, energy pumped into the tank circuit, increasing RMF amplitude to the maximum possible level. When the FRC begins to form, the RF supply is disengaged and the tank circuit rings at whatever frequency physics dictates until the plasma has drained all the energy from the tank. Thus, the RMF amplitude during formation is limited only by the maximum amplitude attainable in an unloaded state, rather than the amplitude attainable during loading.

The situation is analogous to that of a mechanical clutch, in that rotational energy can be stored in a flywheel before the clutch engages. When the clutch is dropped, the energy in the flywheel is transmitted to the load at a much greater rate than would be possible otherwise. Thus, the pulsed RMF formation scheme used in ELF is a novel, high-power method of FRC formation.

2.5 Triggering and Data Acquisition System

The triggering and digitization of data in ELF is all performed through a LeCroy 8013A desktop CAMAC system interfacing with a personal computer through a LeCroy 8901A CAMAC to GPIB interface, then through a National Instruments GPIB-USB-HS GPIB to USB interface. The triggering is performed using a Jorway model 221 timing and sequence card and a Jorway model 222 TTL buffer card. These cards also trigger the digitizers and the RMF triggering system (Quantum Composer model 9514 Pulse Generator) through RG-174/U with LEMO 00 and

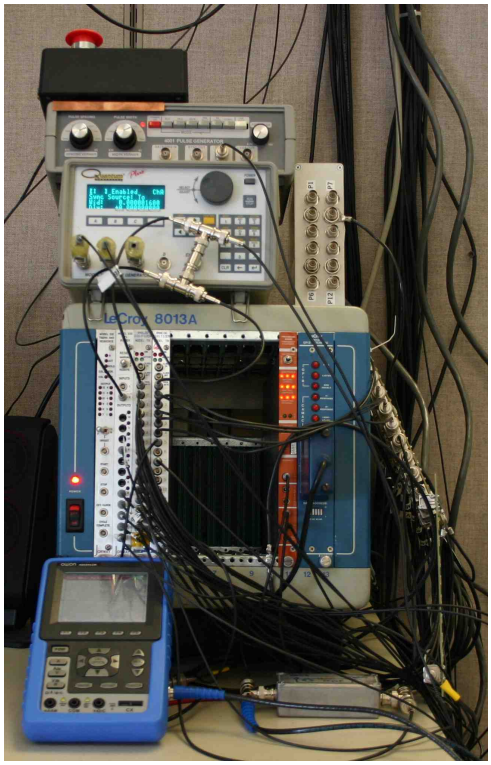

(a) CAMAC based data acquisition and triggering

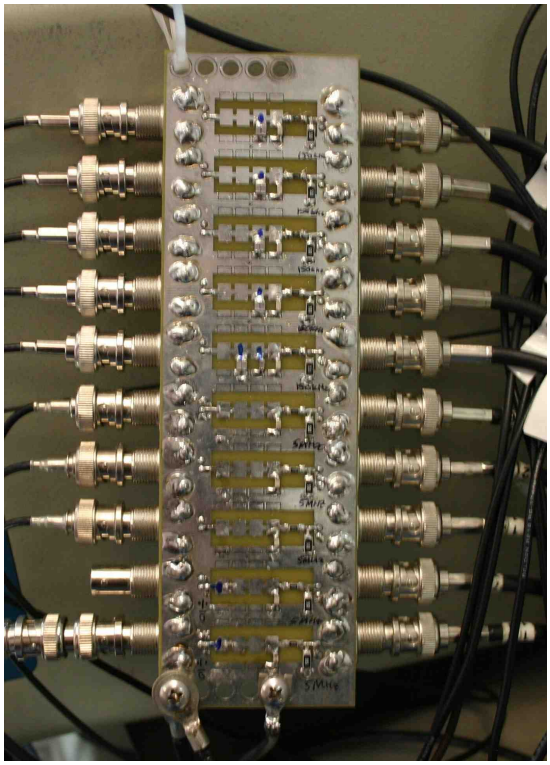

(b) Filter boards.

Figure 2.15: ELF data acquisition and triggering system.

BNC connections. Other components of the experiment (switching, puff, etc.) are triggered via 1 mm plastic optical fiber (Avago 660 nm Versatile Link system) also through the Jorway model 222.

Most of the signals from the experiment are carried on RG-223/U coaxial cable and passed through an external filter board prior to digitization. The filter boards consist of 10 parallel channels with BNC input/output, 50 Ω termination on both sides (as it is observed that the Joerger digitizers produce a high frequency noise), common grounding, and a 150 kHz low-pass filter (the channels for measuring

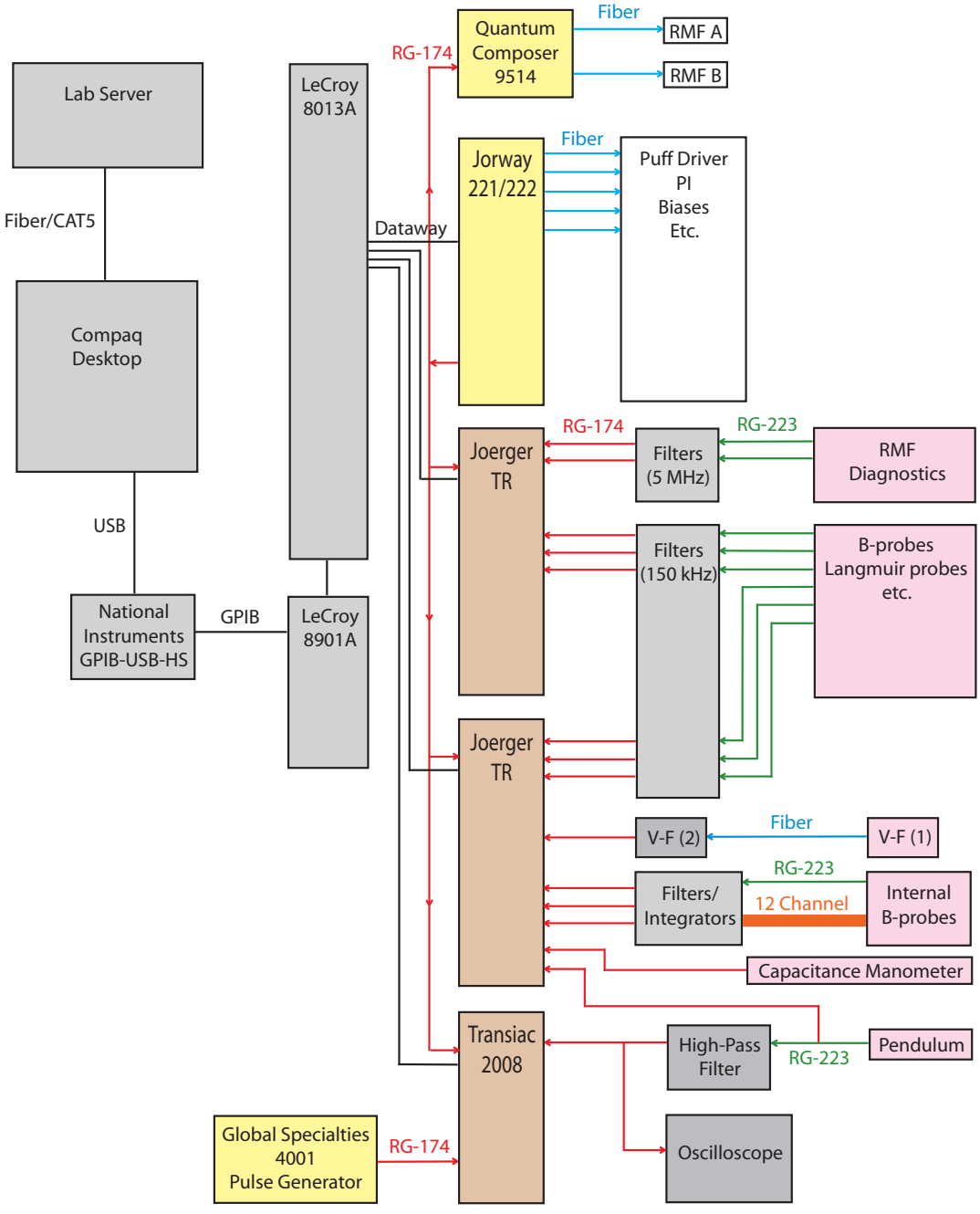

Figure 2.16: Layout of ELF diagnostic, triggering, and data acquisition systems.

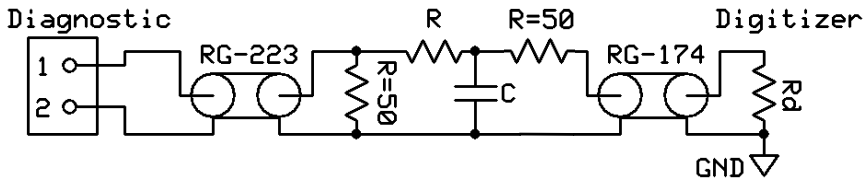

Figure 2.17: Schematic of a single channel of the filter boards.

RMF have 5 MHz filters), which serve to remove excess noise prior to digitization (see Figure 2.17). The characteristic resistance in the RC filter must be much larger than 50 Ω (for proper transmission line termination), but much smaller than the resistance of the digitizer ($50 \ll R \ll R_d$). The capacitance is then set by the required cutoff frequency of the filter (for example, one set of filter channels utilizes $R = 330$ Ω and $C = 3.3$ nF). Since many of the diagnostics are magnetic pickup loops, they are very sensitive to high frequency noise. If the filter boards are not used, the desired low frequency signal can easily be overwhelmed by RMF pickup to the point where the signal exceeds 5 V (the limit of the digitizers), making numerical integration impossible. Some diagnostics pass through other types of signal conditioning circuitry prior to digitization (the pendulum, the capacitance manometer, the internal magnetic field probe, and the voltage-to-frequency probe that senses the charge on the RMF capacitor bank), these will be discussed along with the particular diagnostic in the appropriate section.

After passing through their respective conditioning circuits, the signals are routed via RG-174/U to the appropriate digitizer. There are two, 16 channel, Joerger model TR digitizers, and one, single channel, Transiac 2008 digitizer. The

Transiac is used to measure the slow oscillations of the pendulum (see Section 2.6.7 for further details on this subsystem), while the Joerger cards are used to measure the fast signals. Since the Transiac needs to measure the slow timescales of the pendulum, it requires a slow external TTL clock supplied by a Global Specialties 4001 Pulse Generator (the Joerger cards use an internal clock).

The CAMAC hardware is controlled using several hardware specific drivers written in LabVIEW 7.1 and a comprehensive driver interface VI that is capable of running all required drivers in a single interface. An ActiveX control program (called DatAcqSvr.exe) handles access to the database on the laboratory server, where data is stored in Hierarchical Data Format HDF5 format. This infrastructure is common to several experiments at the University of Washington Plasma Dynamics Laboratory and MSNW (the configuration of a similar system is explored in greater depth in a PhD dissertation by Samuel Andreason [22]).

2.6 Diagnostics

The following section describes the various diagnostics employed on ELF. The diagnostics include neutral gas gauges such as the capacitive manometer and the fast ion gauge, plasma particle flux diagnostics such as the Langmuir probes and the ballistic pendulum, magnetic field probes (both internal and external), current, voltage, and RF energy input (see Figure 2.18 for locations of some diagnostics).

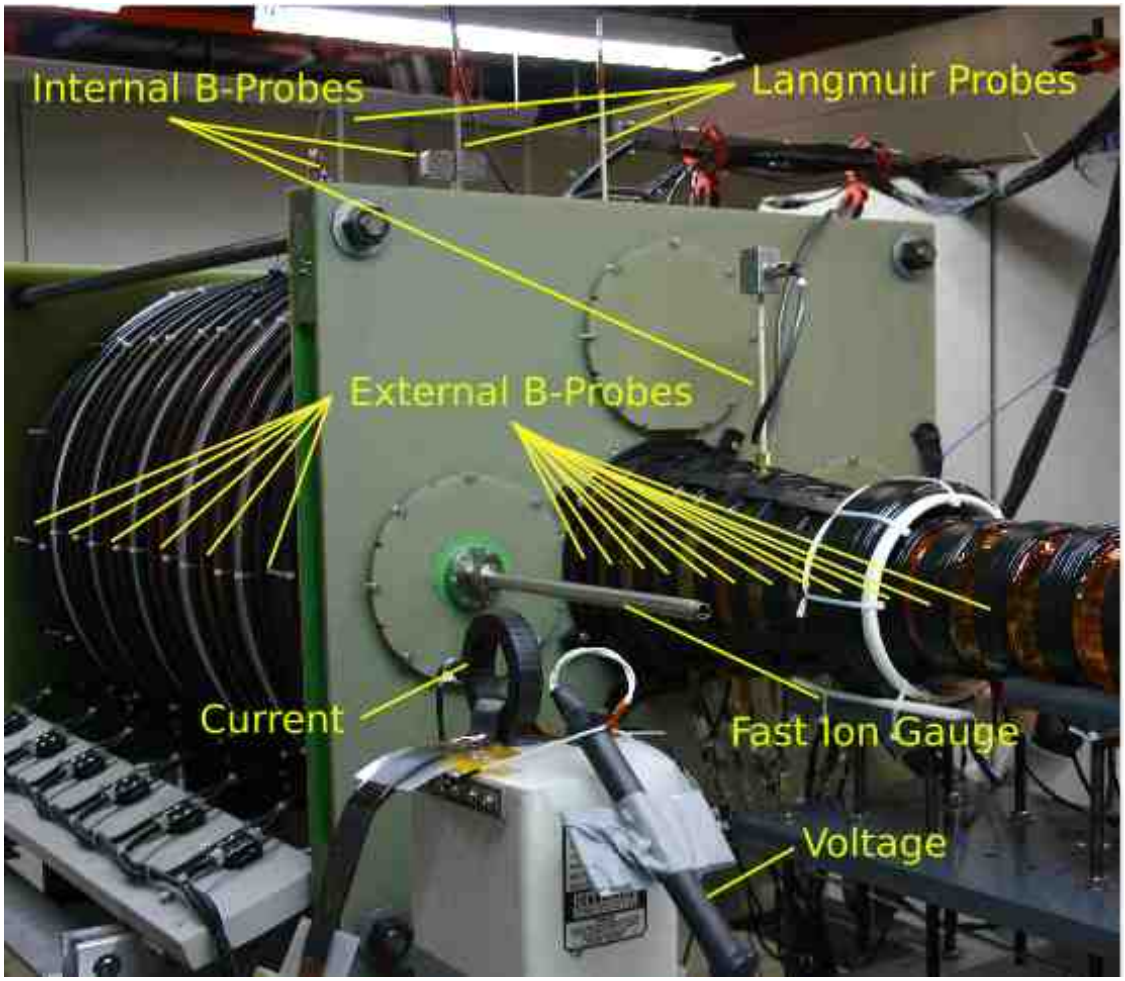

Figure 2.18: Location of the various diagnostics on ELF.

Figure 2.19: MKS Baratron 627A Capacitance Manometer.

2.6.1 Capacitance Manometer

A MKS Baratron 627A Capacitance Manometer (see Figure 2.19) is installed on the 6-way cross at the downstream end of the experiment. The response of the 627A is $0 - 250$ mT ($0 - 10$ V). A capacitance manometer determines the pressure by measuring the capacitance between a flexible membrane and a rigid back plane. This provides a gas independent way to measure the pressure in the chamber. The response time of the device is roughly 200 ms, much longer than the time it takes for gas to distribute itself throughout the chamber. On ELF, the capacitance manometer is used to measure the chamber pressure before and after a gas puff. This provides an estimate for the total amount of gas released through the valve and can be used to calibrate the Fast Ion Gauge (see Section 2.6.2). It

should be noted that the capacitance manometer signal is routed directly into a Joerger TR digitizer (no pre-filtering or termination).

2.6.2 Fast Ion Gauge

An R.M. Jordan B-451 Fast Ion Gauge (FIG) (along with the D-403 Fast Ion Gauge Power Supply) is installed in the left-hand (when looking downstream) circular plate in the upstream G-10 wall of the drift chamber through a $\frac{3}{4}$ inch Quick Disconnect feed-through mounted in the center of the plate (see Figure 2.20a). The gauge is mounted on the end of a $\frac{3}{4}$ inch steel rod that is bent at one end to place the sensor directly in the gas flow at the axis of the experiment. This configuration allows the probe to be swept radially throughout the gas flow, and moved out of the flow (as not to perturb the plasma) when desired.

This ionization gauge uses a Bayard-Alpert type [23], hot filament design, which demonstrates a response that is species dependant [24]. The capacitance manometer (see Section 2.6.1), which is a calibrated, gas independent pressure sensor, was used to calibrate the FIG. The gate valve over the turbo pump was closed, sealing the system, then gas is introduced into the chamber through the puff valve in various amounts. The final signal registered on the FIG was compared to the pressure measured by the capacitance manometer, and was found to require a calibration constant of 0.388 V/mT in nitrogen (see Figure 2.21).

The FIG is capable of measuring pressures of $0 - 0.56$ mT in nitrogen, with a temporal resolution of ~ 10 μs. This is sufficiently fast to measure the time dependence of the flow of neutral gas at the mouth of the thruster. It should also

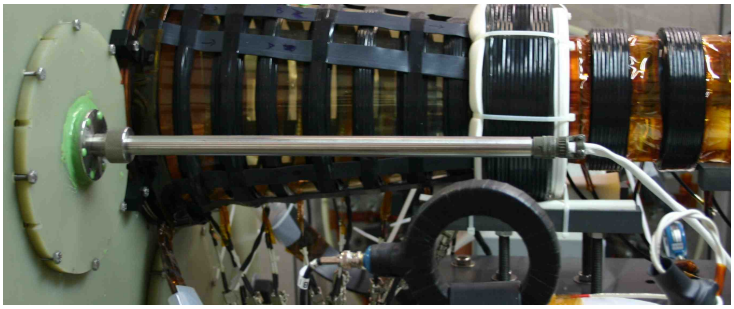

(a) Fast Ion Gauge installed in the drift chamber.

(b) FIG Power Supply.

Figure 2.20: Fast Ion Gauge (FIG) hardware on ELF.

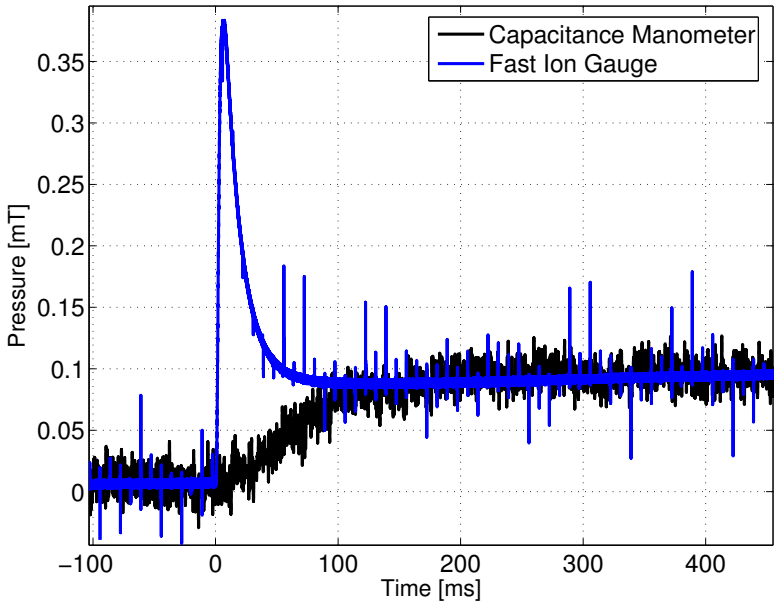

Figure 2.21: Sample waveforms of the Capacitance Manometer and the calibrated FIG.

be noted that the FIG is routed through a standard 50 Ω terminated, 150 kHz low-pass filter board channel.

2.6.3 Current and Voltage Measurement

Often times over the course of experimentation on ELF, the need to measure large currents (kiloamperes) and voltages (kilovolts) over short timescales (microseconds) has arisen. For most purposes, the current probes made by Stangenes Industries were used. The two models currently in use are the 0.5-1.0 (1.0 V/A) and the 3-0.002 (0.002 V/A) Pulse Current Transformers. These probes measure current accurately up to their maximum rated It (amp-seconds) value, then the signal begins to droop. A simple droop correction can be made numerically and incorporated into a calibration m-file (see Appendix A.1 for example).

Currents in the magnets and PI systems are measured using the 3-0.002 probes, and Langmuir probe currents are measured using the 0.5-1.0 probes. Differential voltages in the PI and RMF systems are obtained by measuring the current through a large resistance (typically ~ 5 kΩ) using a 3-0.002 probe. It should be noted that this type of voltage monitor is useful only on systems which see high voltage for a short period of time (for example the voltage across the electrodes of an MPD). It is infeasible to measure a DC voltage (for example the charge voltage of a bank of capacitors) using this method due to excessive power loss through the resistor.

Voltage on the capacitor banks is usually monitored directly via voltage meter, although the RMF charging system (unlike the other systems) is not voltage regulated, and sometimes an accurate recording of the charge voltage is required

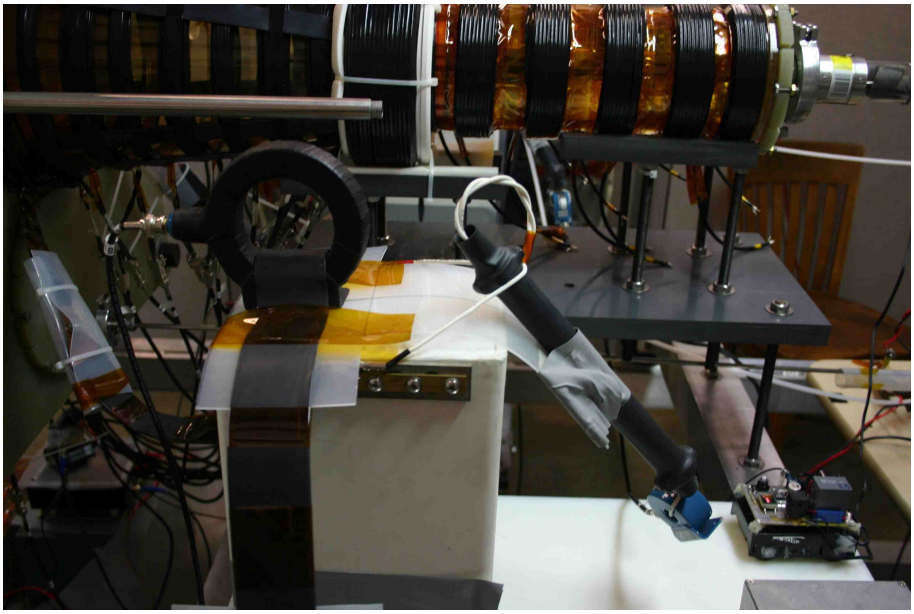

Figure 2.22: Current and voltage probes on the RMF tank circuit.

just before and after the discharge. For this purpose a custom voltage to frequency (V-F) voltage monitoring system (detailed in [22]) is used. It translates a range of voltages into a range of frequencies transmitted via fiber-optic cable outside the experimental enclosure, where the light pulses are converted to electrical pulses and read by the data acquisition system. Since the V-F system senses a much smaller current than the Stangenes 0.5-1.0, a much larger resistor can be used, with negligible power drain.

It should be noted that signals form the voltage and current probes that utilize a Stangenes probe are routed through a standard filter board (150 kHz low-pass, 50 Ω termination) with the exception of the RMF probes (which have 5 MHz low-pass filters). The V-F system has no filtering, but is terminated with 50 Ω.

Figure 2.23: Photograph of Langmuir probe.

2.6.4 Langmuir Probes

There are 3 Langmuir probes installed along the length of the drift chamber, which measure the properties of the ejected plasmoid. Specifically, measurements for the electron temperature and the drift velocity were used. The construction of the probes are nearly identical; floating double probes, consisting of an Alumina rod, with a small cylindrical Tungsten electron-absorbing tip (6 mm in length, 1.75 mm in diameter), and a larger tungsten ion-absorbing plate (5.5 $\times$ 10.5 mm) located downstream of the electron-absorbing tip (see Figure 2.23). The two tips are biased to a set voltage relative to each other (but floating as an assembly). The probe current is measured using a Stangenes current probe (see previous section) which is located within a shielded enclosure near to the experiment, and the signal from the current measurement is transmitted via coaxial cable to the data acquisition system.

The current to the tip of a Langmuir probe is the sum of the ion and electron fluxes. In the case of ELF, the ions are streaming at supersonic speeds, and the

probe current is approximately equal to the ion flux to the probe tip [25].

$$\Gamma_i = f n_\infty c_s \tag{2.11}$$

$$f = \exp\left(-1 - 1.1 M_\infty\right) \tag{2.12}$$

Where M_∞ is negative for the upstream facing side and positive for the downstream facing side of the probe tip, and c_s is the sonic speed, and n_∞ is the density far from the probe tip. The electrons are quite subsonic, and their collection is the same as if the plasma were stationary.

$$\Gamma_e = \frac{1}{4} n_\infty \overline{v_e} \exp\left(eV_o/kT_e\right) \tag{2.13}$$

Where $\overline{v_e}$ is the mean electron speed, and V_o is the probe tip voltage with respect to the plasma potential.

The large probe tips in ELF are operated in ion-saturation, i.e. almost all of the electrons are repelled and only the ion current is measured. This combined with the mach number and sound speed provides a measure of local density. If the flow is supersonic, then the current to the downstream facing side of the probe tip becomes small compared to the upstream collection. The probe current can then be taken to be approximately equal to the mean ionic flux to the upstream surface the size of the probe tip.

$$I = \left(e\Gamma_i A_{cs}\right)_{upstream} - \left(e\Gamma_i A_{cs}\right)_{downstream} \tag{2.14}$$

If the current to electron absorbing tip is below the electron saturation current, then the total probe current (from ion-collecting tip to electron-collecting tip) is simply equal to the rate of ion absorption by the large tip.

Since the current measured is approximately equal to the total integral of the ion flux over the area of the large tip, the integral of the probe signal is approximately equal to the total number of particles passing through an area the size of the large tip as the plasmoid passes. Thus, the axial center of mass of the passing plasmoid can be computed using the time-history of the probe current (when the integral of the probe current reaches half its ultimate value, half of the mass has passed by). Using data from two probes located at different axial position, the velocity of the center of mass of the plasmoid can be computed (see Appendix A.4).

The current to the large tip of the probe when operating below the ion-saturation current can be expressed as a function of the ultimate ion-saturation current, the tip voltage, and the electron temperature.

$$I = I_{si} \tanh\left(eV_{app}/kT_e\right) \tag{2.15}$$

Where V_{app} is the applied voltage between the two probe tips. As the voltage is increased, more electrons are repelled until ion-saturation is reached. Thus, by varying the probe voltage, the electron temperature can be measured.

The inherent uncertainty in the measurements of the center-of-mass velocity and the electron temperature is estimated to be in the range of 15 - 20 %. This is due to approximations regarding the particle flux to the tips of the probes and

variations in the measured data due to the statistical variation in the behavior of the experiment (see Chapter 3). While the uncertainty in many of the diagnostics in the ELF experiment is somewhat high, ELF is proof-of-concept experiment, with the increase of diagnostic accuracy being the subject of future work.

This analysis makes many assumptions which are valid for the plasma parameter ranges within ELF. Specific assumptions are: that the sheath is collisionless, the magnetic field is unimportant, the sheath area is approximately the same as the probe tip area, the drift velocity is supersonic, and the small probe tip is capable of absorbing enough electrons to balance the ion current from the large tip.

2.6.5 Magnetic Field Probes

There are two types of magnetic diagnostics used on ELF; internal and external probes. Both types are wire pick-up loops, operating via Faraday's Law.

$$\nabla \times \mathbf{E} = -\frac{\partial \mathbf{B}}{\partial t} \tag{2.16}$$

The internal probes within the drift chamber consist of many loops of fine magnet wire wound around a hollow tube of alumina roughly 1 cm in diameter, attached to a $\frac{1}{4}$ inch alumina rod fed through the quick-disonnect ports within the drift section (see Figure 2.24). There is also an internal B-probe for probing within the cone, which utilizes small pre-fabricated surface-mount air-core inductors mounted axially completely within an alumina rod.

The signals are partially integrated using a low-pass circuit similar to that

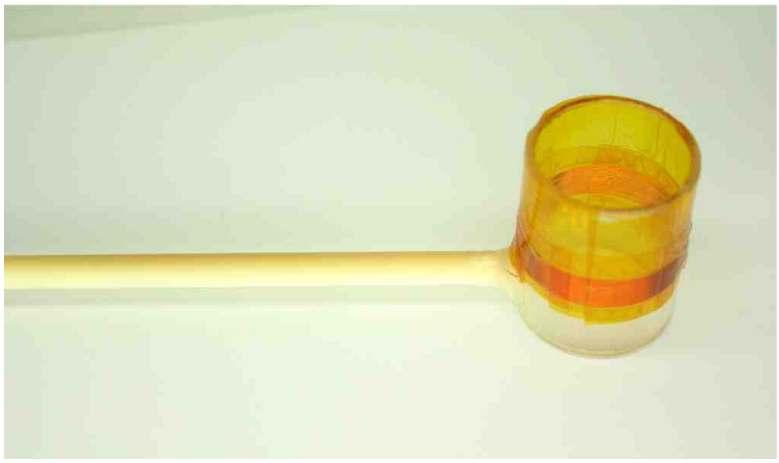

Figure 2.24: Photograph of internal B-probe.

described in Section 2.5 such that the signal over the ranges of interest is maximized. The magnetic field measured by the probe can be determined from the time-history of the measured voltage at the digitizer and a knowledge of the specific construction of the probe and integrator circuit.

$$\frac{V_d}{V_p} = \frac{\frac{1}{i\omega C}}{R + i\omega L + \frac{1}{i\omega C}} \tag{2.17}$$

$$V_p = i\omega\phi \tag{2.18}$$

$$B = \frac{V_d}{NA}\left(RC + i\omega LC + \frac{1}{i\omega}\right) \tag{2.19}$$

$$\tag{2.20}$$

Where V_d is the measured voltage at the digitizer, V_p is the voltage generated by the probe, ω is the frequency of the magnetic field expressed in radians per second, ϕ is the magnetic flux. The quantities L, R, and C are the inductance of the probe,

total circuit resistance (probe plus resistor), and the capacitance within the circuit. Finally N and A are the number of turns and the area of the internal probe.

In order to implement this numerically on a digitized signal, one can transform out of frequency space, and use the integral and derivative of the measured signal to obtain the measured magnetic field (see Appendix A.2 for example).

$$B = \frac{1}{NA}\left(RCV_d + LC\frac{\mathrm{d}V_d}{\mathrm{d}t} + \int_0^t V_d \mathrm{d}t\right) \tag{2.21}$$

Alternatively, Equation 2.17 can be used to obtain an estimate for the digitizer voltage for a given magnetic field and frequency. This can be quite useful when designing the internal probe (see Figure 2.25).

$$V_d = \frac{BNA}{RC + i\omega LC + \frac{1}{i\omega}} \tag{2.22}$$

The external probes consist of a copper solder-wick rope wrapped around a sheet of polyethylene, which is then wrapped around the circumference of the tube (or cone) beneath the flux conservers (see Figure 2.26). In this way, the average excluded field resulting from the presence of an FRC within the flux conserver can be determined. The external B-probe is a very useful diagnostic for determining the properties of an FRC (see Section 1.3). The implementation of these probes is similar to that of the internal probes.

The main sources of uncertainty in the measured magnetic fields arise from an inaccurate knowledge of the precise dimensions and orientation of the probes with respect to the magnetic field, and the inherently large amount of electromagnetic

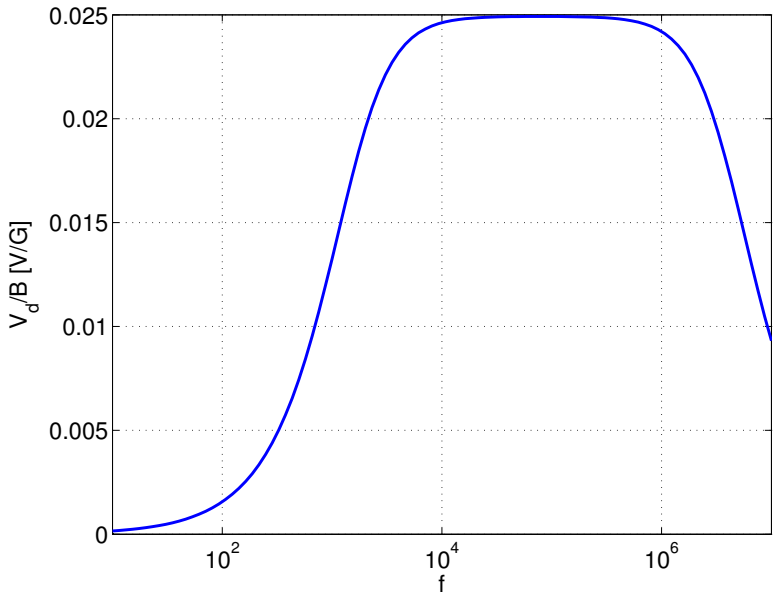

Figure 2.25: Response of the internal B-probe.

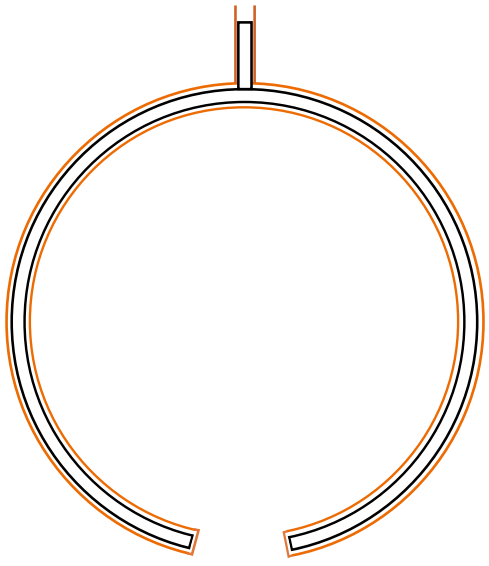

Figure 2.26: Layout of the external B-probes.

noise and magnetic field oscillations due to the presence of the RMF and plasma. Thus the magnetic field diagnostics are estimated to have an inherent uncertainty of 15 - 20 % (similar to that of the Langmuir probe data).

2.6.6 RF Energy

In order to obtain an accurate estimate of the amount of RF energy which is absorbed by the plasma compared to that which is lost by other mechanisms, the operation of the RMF system was simulated using SPICE (specifically Intusoft's ICAP/4Rx software, see Figure 2.27a).

The RF driver and tank circuit were modeled using the specified values for the constituent passive components (confirmed by measurement with a sensitive meter), and the switches were modeled such that their behavior in a simplified circuit matched the trends plotted in the manufacturer data sheets. Non-standard components such as copper strip-line, the 1:1 transformer, and the RMF antennae were measured for an initial estimate, then the output of the SPICE simulation was compared to measurements of the RMF discharging in the absence of plasma in order to refine the model. Voltage and current were measured in multiple locations on the tank circuit and RF supply in order to verify the accuracy of the model.

The plasma was simulated by switching a resistive load into the tank circuit at the observed time of RMF breakdown of the neutral gas. The value of the resistance was adjusted until the output of the simulation was consistent with the experimentally measured waveforms (sometimes multiple different resistive loads were used to match the varying plasma load to match observations). Once the

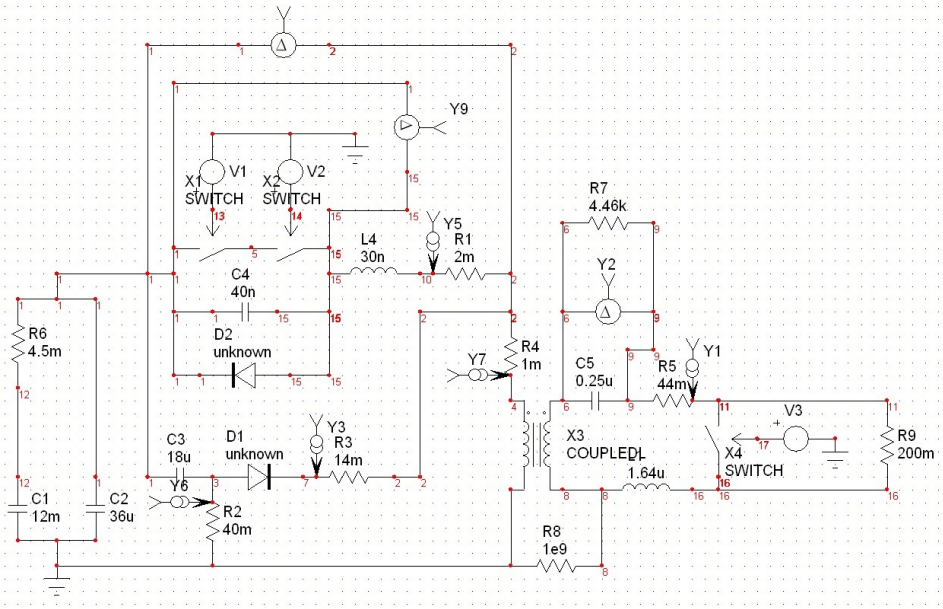

(a) SPICE model of RMF system.

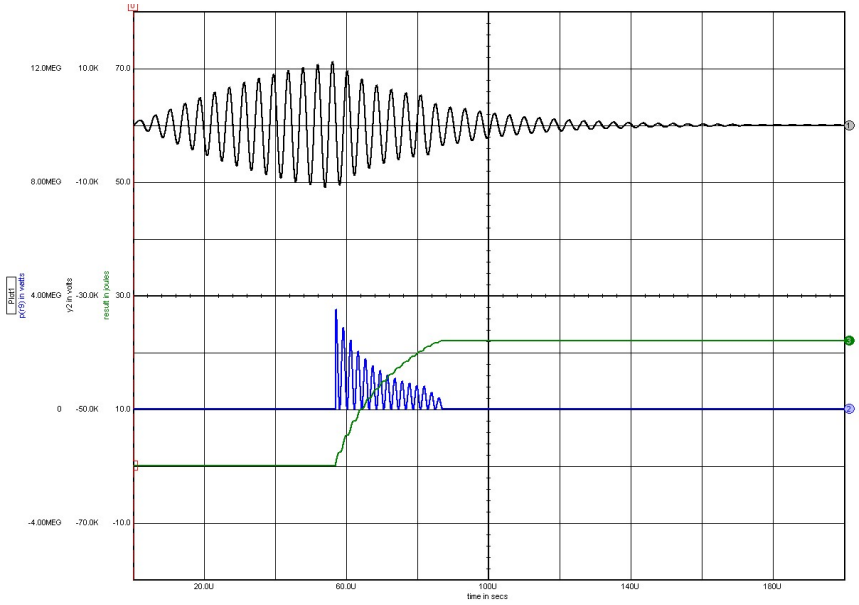

(b) Output of SPICE model.

Figure 2.27: Matching the SPICE waveform to the observed data allows one to compute the energy absorbed by the plasma.

resistive loads were adjusted such that the SPICE waveforms matched the experimentally obtained traces, the energy absorbed by the plasma (resistive load) could be computed for use in determining the formation efficiency (see Figure 2.27b).

The largest source of uncertainty inherent to the estimation of the RF energy into the plasma is due to the fine-scale matching of the voltage traces needed to make an estimate of the energy. This process was done by hand (i.e. not automated), and the energy was found to be similar for a variety of similar discharges. The uncertainty of energy quotes in the remainder of this work come with an estimated uncertainty of ~ 15 %.

2.6.7 Pendulum

A novel type of ballistic pendulum was constructed for the purpose of ascertaining the thrust of ELF. The major concern when measuring the momentum of a plasma using a pendulum is that the collision between the plasma and the pendulum may not be completely inelastic. This can arise in the obvious way due to particles elastically rebounding from the pendulum, but it can also arise from the ablation of the surface of the pendulum due to the large energy of the plasma particles. In an effort to mitigate these effects, the pendulum on ELF was constructed of a lightweight plastic mesh frame faced with a felt-like filter material made from ultra-fine (400 μm) quartz fiber (see Figure 2.28). The material absorbs incident particles, which randomly reflect around inside the microstructure, and are eventually are dispersed omni-directionally at low speed, resulting in a net inelastic collision between the pendulum and the plasma. This effect ensures that

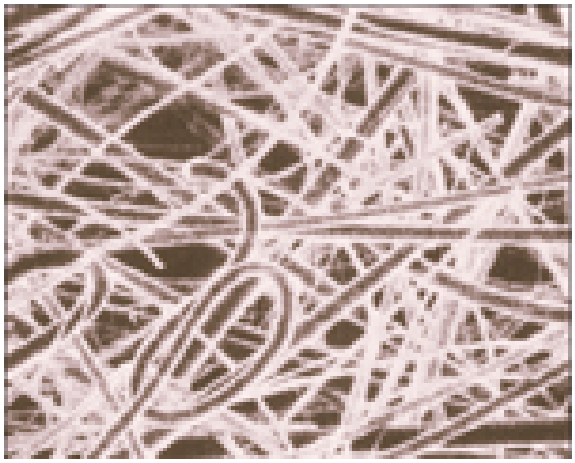

Figure 2.28: Microscopic view of pendulum surface.

any sputtered particles are randomly dispersed as well. One layer of material was used in order to maintain a thin pendulum and promote the equality of the eventual gas dispersal in both the upstream and downstream directions (it is estimated the material is at least several optical depths thick). In addition, the impact of any non-uniformities in the direction of dispersal are minimized by the relatively low velocity which the particles posses after several collisions with the cold pendulum material.

In order to prove that the pendulum does indeed perform in this way, an identical pendulum assembly was tested at the NASA Glenn Research Center micro-Newton thrust stand in chamber VF-3, which is typically used for pulsed plasma thrusters (see Figure 2.29). The plasma source used these tests was the High Power Helicon thruster developed by the University of Washington and MSNW [26], which is similar in design to the ELF thruster. During the tests the thruster was operated at various energy levels, neutral gas was exhausted in varying amounts, and the

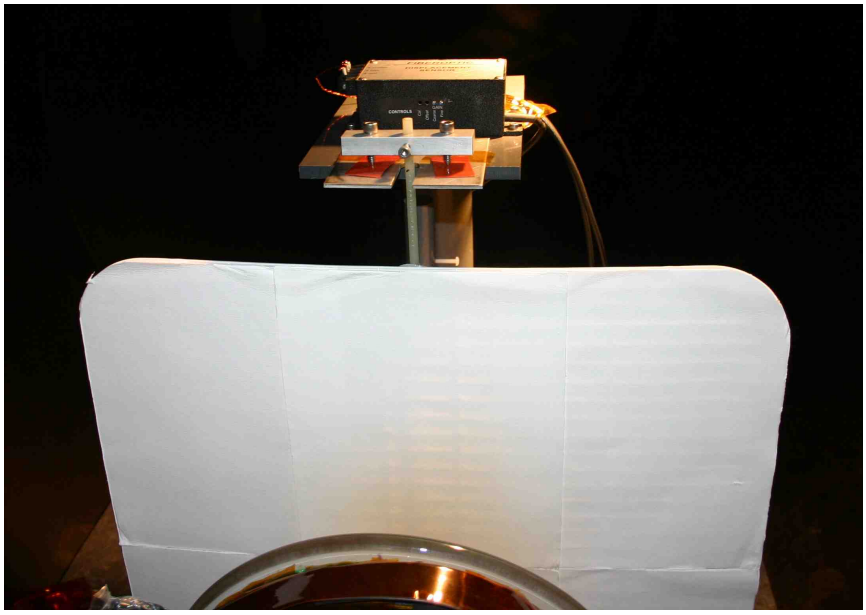

Figure 2.29: Pendulum undergoing testing in Glenn Research Center, chamber VF-3.

thrust measurements obtained from the pendulum were compared to those form the thrust stand. The pendulum showed no evidence of augmented thrust during plasma discharges up to the maximum energy tested.

The ELF pendulum consists of several sheets of quarts fiber material (Advantec - QR100 Quartz Prefilter) mounted on a 52×52 cm nylon grid attached to a $\frac{1}{4}$ inch alumina rod. The alumia rod is secured through an aluminum axle via a set screw, which pivots on an aluminum plate atop two sharpened screws (see Figure 2.29). The aluminum plate is mounted on a PVC frame, which sits inside the 80 cm drift section slightly over a meter downstream of the thruster. The motion of the pendulum is measured by a PHILTEC D169 optical displacement sensor, which consists of a sensor body (located at the top of the PVC structure near the

Figure 2.30: The PHILTEC D160 optical displacement sensor.

pendulum pivot point) and a fiber-optic cable with an eye at the end. The eye is held in place by the PVC structure and determines the distance to the pendulum by reflecting light off a small steel reflector mounted at the bottom edge of the pendulum. Power to the sensor and the output signal are fed through the vacuum boundary.

Since the pendulum is at rest prior to the discharge, the period of the pendulum is long compared to the discharge, and the mass of the plasma is much smaller than the mass of the pendulum; the impulse produced by the thruster can be approximated as being equal to the momentum of the pendulum immediately following the discharge ($\Delta p = mv$, where p is the momentum of the pendulum, m is the pendulum mass, and v is the pendulum velocity). The velocity can be obtained by equating the kinetic energy of the pendulum at the bottom of the swing to the gravitational potential energy at the top of the swing (where g is the acceleration due to gravity, and h is the height risen by the center of mass, see Figure 2.31).

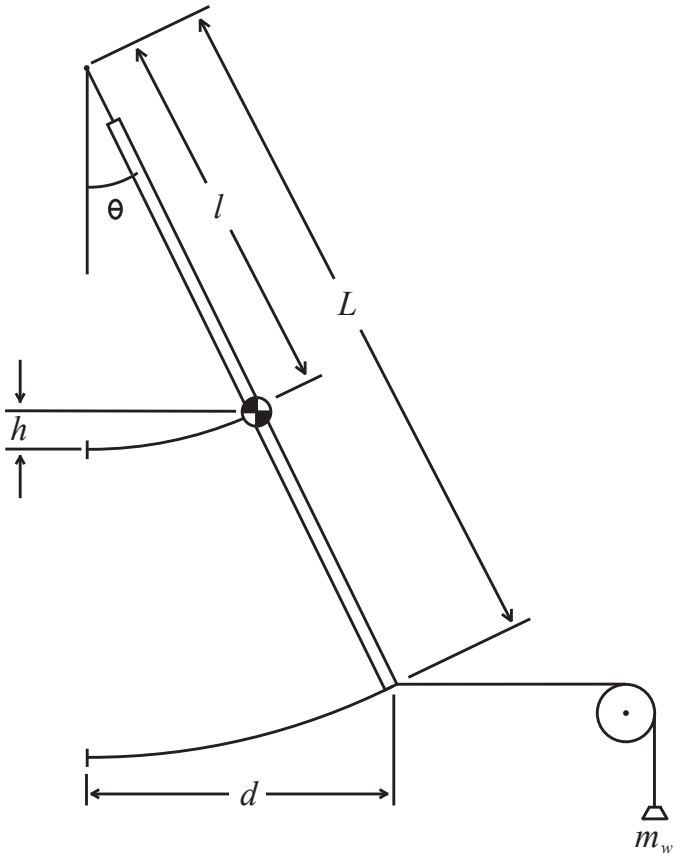

Figure 2.31: Diagram of the pendulum.

$$\frac{1}{2}mv^2 = mgh \tag{2.23}$$

$$v = \sqrt{2gh} \tag{2.24}$$

In order to measure the height through which the center of mass swings, its location needs to be calculated. This can be achieved by measuring the period, and using the small angle approximation for the period of a pendulum (P is the period, l is the distance from the pivot point to the center of mass, and θ is the angle of the pendulum).

$$P \approx 2\pi\sqrt{\frac{l}{g}} \tag{2.25}$$

$$l \approx g\left(\frac{P}{2\pi}\right)^2 \tag{2.26}$$

$$h = l - l\cos\theta \tag{2.27}$$

The angle of the pendulum can be computed from the displacement sensor data (L is the distance from the pivot point to the reflector used by the displacement

sensor, and d is the distance measured by the sensor).

$$\theta = \sin^{-1}\left(\frac{d}{L}\right) \tag{2.28}$$

$$h = l\left[1 - \cos\left(\sin^{-1}\left(\frac{d}{L}\right)\right)\right] \tag{2.29}$$

$$h = l\left[1 - \sqrt{1 - \left(\frac{d}{L}\right)^2}\right] \tag{2.30}$$

To obtain the impulse imparted to the pendulum, the mass must also be known. This can be determined by applying a horizontal force to the pendulum using weights and pulleys, and recording the distance measured by the displacement sensor (see Figure 2.31). By balancing the torques about the pivot point, the effective mass of the pendulum can be inferred (m_w is the mass of the calibration weight).

$$mgl\sin\theta = m_w gL\cos\theta \tag{2.31}$$

$$m = \frac{m_w L}{l\tan\theta} \tag{2.32}$$

Since the period of the pendulum is many orders of magnitude larger than the timescales of the discharge, the pendulum is inherently immune to the high levels of noise present during the discharge, but because of this, the signal from the displacement sensor cannot be measured using the same digitizers as the other diagnostics. Therefore a separate, one-channel digitizer (Transiac 2008) was used to measure the slower signal form the pendulum, thus allowing the signal to be

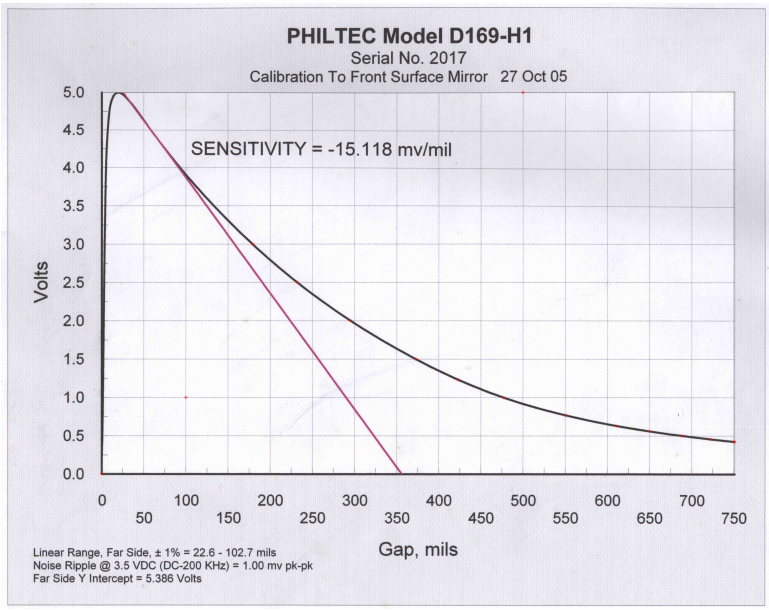

Figure 2.32: Response curve of the PHILTEC D169 optical displacement sensor.

acquired and encoded using the same CAMAC system as the other diagnostics, without having to use an entire 16 channel digitizer to measure the slower signal. The use of the Transiac digitizer did, however, involve some added complication.

The output voltage of the displacement sensor is a function of distance between the eye and reflector (as shown in Figure 2.32). In order to maximize the sensitivity, the eye is positioned such that when the pendulum is at rest, the output voltage of the displacement sensor is roughly 3.5 volts. As the pendulum oscillates, the signal oscillates about this voltage. However, the Transiac digitizer is only capable of measuring a signal of $\pm\frac{1}{4}$V, therefore, the signal is sampled prior to the discharge with one of the channels of the fast digitizers (to determine the offset), then passed through a high-pass filter to the Transiac which captures only the oscillation (not the offset). The offset is then added back to the signal during analysis. Due to

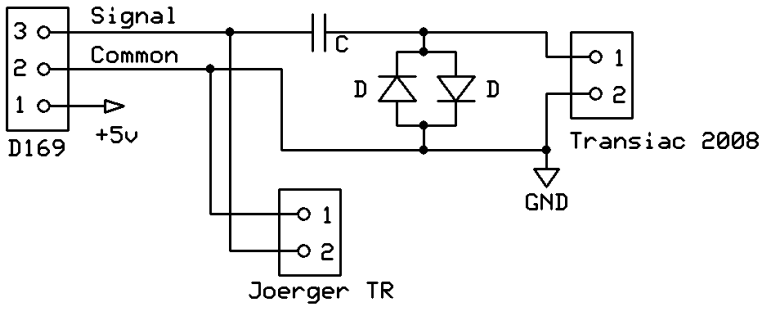

Figure 2.33: Diagram of pendulum circuit.

the relatively low input impedance of the Transiac digitizer (1.1 kΩ), the signal is attenuated slightly. Since the output impedance of the displacement sensor was not known, a correction factor was determined by measuring the signal with a digitizer of relatively high input impedance (Joerger TR - 90 kΩ), and observing the change in signal when the Transiac digitizer was connected and disconnected (the signal was also measured with a 10 MΩ oscilloscope as a secondary confirmation).

During analysis, the first maxima and minima of the signal are used to determine the maximum and minimum distance measured by the displacement sensor (see Appendix A.3). The error caused by the low input impedance of the digitizer can be corrected by multiplying the first maxima of the recorded signal by a correction factor of 0.819, and multiplying the first minima by 1.356. The horizontal displacement of the pendulum can then be obtained using the calibrated response curve supplied by the manufacturer (see Figure 2.32). Using the horizontal distance traveled by the pendulum and the mass of the pendulum, the impulse imparted can be computed using the methods described earlier.

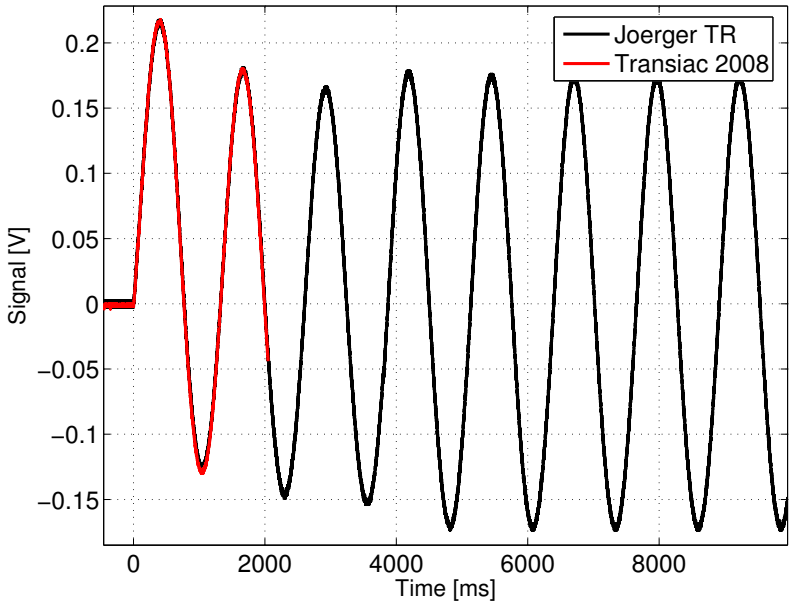

Figure 2.34: Signal attenuation due to Transiac input impedance.

The uncertainty in the impulse measurement comes from several sources: the uncertainty of the digitized signal (≈ 2.5 %), the correction for the input impedance of the Transiac digitizer (≈ 2.5 %, leading to an uncertainty in measured distance of ≈ 5 %), the uncertainty in the mass of the pendulum (≈ 4.5 %), the uncertainty in the distance from the axle to the eye of the sensor (≈ 0.2 %), and the uncertainty of the distance to the center of mass (≈ 0.3 %). These factors combine to give an uncertainty of ≈ 9.85 % in the measurement of the impulse imparted to the pendulum. This is smaller than the typical variation in the impulsed produced by the thruster due to inconstancies in the breakdown time (see Section 3.7). An additional source of error when using the pendulum to make impulse measurements is due to the fact that not 100 % of the plasma emitted from the thruster strikes the pendulum. The fraction of the total plasma absorbed is a function of pendulum

positioning and the level of bias field present in the drift chamber. Several methods were used to determine a correction factor for the mass fraction (see Section 3.8), however, this remains the largest source of uncertainty in the impulse measurement. The estimated uncertainty in the impulse of the plasma as measured by the pendulum is estimated to be 15 - 20 % (similar to the other diagnostics).

The pendulum is a convenient diagnostic for initial testing because it is small, it can fit inside the available vacuum vessel, and it allows the thrust to be measured without the need to place the thruster inside the chamber. However, in some cases of thruster operation, the plasma expands to a point at which it begins to miss the pendulum, providing an incorrect measure of impulse. In addition, the ELF thruster is operating at much higher energy levels than the HPH thruster. The pendulum has not been tested against a thrust stand in this range of plasma energy. Eventually, the ELF thruster will need to be tested on a thrust stand to re-confirm thrust measurements made by the pendulum.

Chapter 3

Experimental Results

In this chapter, selected experimental results are presented to the reader. To date, over 10,000 shots have been taken on the ELF experiment. The earlier phases of testing were fairly exploratory, while the latter phases were more systematic in nature. To present all of the data obtained over the course of testing ELF is beyond the scope of this dissertation, however, information obtained during the early phases of testing that provides valuable insight into the operation of ELF is discussed in Sections 3.1-3.6. The latter phases of testing are the topic of Sections 3.7-3.11.

3.1 Pre-ionization System Development

As described in Section 1.4, the ionization of the neutral gas by the RMF is catalyzed by a small number of free electrons. While it is possible to initiate

the ionization process in the neutral gas using only the naturally occurring trace ionization (resulting from cosmic rays, statistical anomalies, etc.) the addition of a pre-ionization (PI) system greatly enhances the amount of control the operator has over the time at which the ionization process occurs. To date, the only type of pre-ionization that has been employed has been in the form of an arc discharge between two coaxial electrodes similar to the latest PI design described in Section 2.3. This approach was taken because there was a concurrent effort underway to develop coaxial arc PI systems for several other experiments at the MSNW and University of Washington labs. This allowed the synergistic development of a PI more suited to the needs of the ELF system since several pre-existing designs could be tested prior to the construction of an ELF-specific PI system. The development of an electrodeless PI (making ELF truely an *Electrodeless* Lorentz Force thruster) was seen as secondary to the development of other aspects of the thruster and must be a subject of future work. Several of the PI designs that were tested in ELF are described below.

3.1.1 IPA PI

Initially, it was not obvious what characteristics the optimal PI should posses. During the first phase of testing, the RMF system was not yet capable of operating at full power, so flaws in the PI would be more apparent. It was thought that since the final configuration of the plasma would be annular, the neutral gas and the seed plasma should both be deposited annularly rather than on the axis. There was a prototype PI on hand that was built for the Inductive Plasmoid Accelerator

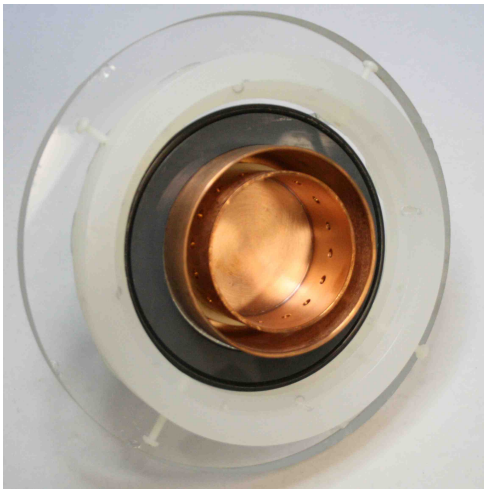

(a) IPA PI prior to installation.

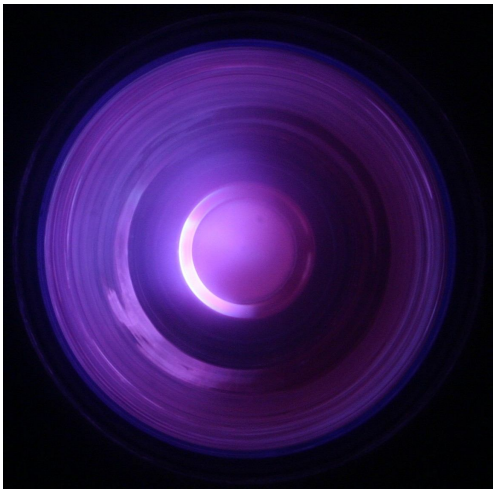

(b) Asymmetric RMF discharge resulting from localized PI arcing.

Figure 3.1: The IPA pre-ionization system.

(IPA) fusion experiment which was annular and roughly the size of the small end of the ELF cone (see Figure 3.1a) which was was modified and installed on ELF.

Upon initial testing, it became immediately clear that the IPA gun was not performing as expected. An examination of photographs taken during the operation of the experiment revealed that the discharge between the electrodes was fairly localized within a small angle of the inter-electrode gap rather than being taking place over the entire azimuth (see Figure 3.1b). In IPA the entire volume was utilized, however in that case, the PI was operated using much higher currents so that all of the charge carriers within the inter-electrode volume were needed to sustain the discharge. In ELF, the goal has always been that the PI use as little energy as possible, thus making the IPA gun a poor choice in this case. In addition, later testing revealed that an axially uniform distribution of neutral gas could be

achieved with a small gas feed on-axis. This removed the perceived requirement that the neutral gas must be injected annularly.

3.1.2 PHD PI

Upon the addition of the small upstream cylindrical section to ELF (see Section 2.1) it became necessary that the PI have the ability to be easily repositioned along the axis of the experiment. This enables the effect of the position of the PI relative to that of the RMF system to be investigated. A PI developed for use on the Pulsed High Density (PHD) fusion experiment, which was designed for ease of axial repositioning, was initially used in the rebuilt ELF experiment. The PHD PI consisted of a cylindrical copper anode surrounding 12 tungsten rods (see Figures 3.2a and 3.2b). While still an annular design, the PHD gun is much smaller than the IPA gun, and the unique cathode design promotes a more uniform discharge.

While the PHD PI was much better at producing a uniform discharge at much lower densities, there were clear directions for further improvement with another iteration of PI. It was still difficult to break down the neutral gas at an interesting range of lower pressures. Also, due to the higher bias fields near the small end of the cone combined with the transient fields produced by the arc of the PI, the gas puff valve would behave erratically; opening and closeing at random times, and occasionally staying open for many times the intended puff duration. Since the impulse from the entire puff is reflected in the pendulum measurement, any inconsistencies result in meaningless data. Since the puff valve in the PHD gun is potted in a location very near to the region of the discharge, this issue was

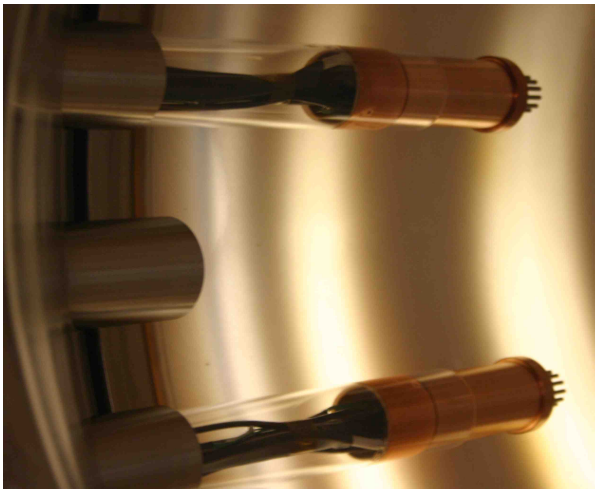

(a) Multiple sources mounted in the PHD experiment.

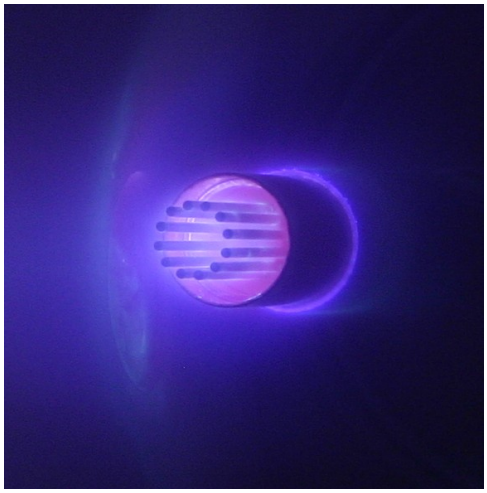

(b) Symmetric discharge in PHD PI.

Figure 3.2: The PHD pre-ionization system.

impossible to resolve without a redesign.

3.1.3 ELF PI

After the PHD PI, there was enough information to design a PI suited to the needs of ELF. Testing with the PHD gun had already revealed that smaller discharge on axis could result in a uniform RMF discharge. In addition, the PI must have the ability to break down gas at low pressures, the design must have the ability to be easily repositioned axially, and the puff valve must be protected from magnetic fields that could interfere with its operation.

There were still concerns that, once leaving the PI, the neutral gas and the seed plasma were not spreading out enough to be optimal for forming an FRC. Testing with the Fast Ion Gauge (see Section 3.3), however, quickly revealed that when the

Figure 3.3: The ELF pre-ionization system.

gas is fed through a PI on axis, it develops a profile that is uniform to within the limits of measurement by the time it reaches the end of the cone. Also, the addition of an adjustable bias field (see Section 3.5) enhanced the spread and uniformity of the seed plasma by mapping most of the field lines that spread throughout the cone directly to the electrodes of the PI.

Moving the puff valve away from the arc and fabricating an iron shield to minimize the effect of the bias field solved the issue of puff reliability (see Section 2.3). This introduced some additional volume between the puff valve and the electrodes, but any affect this had on the flow of neutral gas was found to be unobservable by the time it had flowed into the cone.

To achieve a uniform breakdown at lower pressure and lower voltages, the inter-electrode spacing was smaller than in the previous designs (see next section). Despite this fact, there was still a significant amount of spread in the time at which an

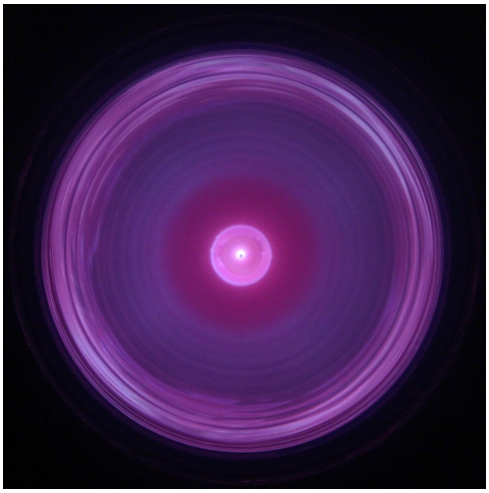

Figure 3.4: Uniform RMF discharge from an ELF-like, single cathode source located on-axis.

arc developed within the PI. This issue was improved with operation at higher line pressures, however, the issue of PI breakdown timing was a concern throughout the course of testing. It was later found that the spread in the time at which the RMF ionizes the majority of the gas is, in most of the interesting cases, larger than the spread in PI breakdown time. Between the two, the statistical variation in the time of ionization affected most of the testing that was performed. As such, at least 5 shots were taken for any given operational condition that was tested.

The entire gun assembly was designed to fit within a quartz tube of the same dimensions as the PHD gun, thus allowing the same sliding vacuum interface to be used (see Section 2.1). A single cathode design was adopted in order to make the dimensions smaller for easier breakdown at low voltages and pressures. Unlike the PHD gun, which was designed for high power, there was little need for a very large cathode area, simply extending the central rod several inches past the anode

provided enough cathode area to keep the discharge steady and uniform.

3.1.4 PI Design

A gas flow is said to be in the fluid regime if the Knudsen number (Kn) is less than 1 ($\mathrm{Kn} = \lambda_{\mathrm{mfp}}/d$, where d is the characteristic length scale of the flow, which is, in this case, the inter-electrode spacing, and λ_{mfp} is the molecular mean free path). The mean free path can be estimated by $\lambda_{\mathrm{mfp}} = \left(\sqrt{2}\pi r_{cs}^2 n\right)^{-1}$ [27], where n is the number density, and r_{cs} is the radius of interaction of the molecule (which is roughly equal to the atomic radius). Taking the atomic radius to be ~ 1 Å, gives the condition $\mathrm{Kn} < 1$ for $nd > 2.27 \times 10^{19}$ [m^{-2}]. Examination of the Paschen curves for various gases reveals that the minimum is typically near 1.0 Torr-cm, for which $\mathrm{Kn} = 0.07$ (at 0.1 Torr-cm, $\mathrm{Kn} = 0.7$). Thus, since the PI aims to operate near the Paschen minimum, the gas must be in the fluid regime.

Since the flow is in the fluid regime, the equations for one dimensional flow in a nozzle can be used to determine the relationship between pressure and channel area. By conserving particles and energy, one can write [28]

$$\frac{A^*}{A} = \frac{\left[1 - \left(\frac{p}{p_o}\right)^{\gamma-1/\gamma}\right]^{1/2} \left(\frac{p}{p_o}\right)^{1/\gamma}}{\left(\frac{\gamma-1}{2}\right)^{1/2} \left(\frac{2}{\gamma+1}\right)^{(1/2)(\gamma+1)/(\gamma-1)}} \tag{3.1}$$

$$\frac{1}{A} \propto p^{1/\gamma} \left(p_o^{\gamma-1/\gamma} - p^{\gamma-1/\gamma}\right)^{1/2} \tag{3.2}$$

where A^* is the area when the flow is sonic, p_o is the stagnation pressure, and γ

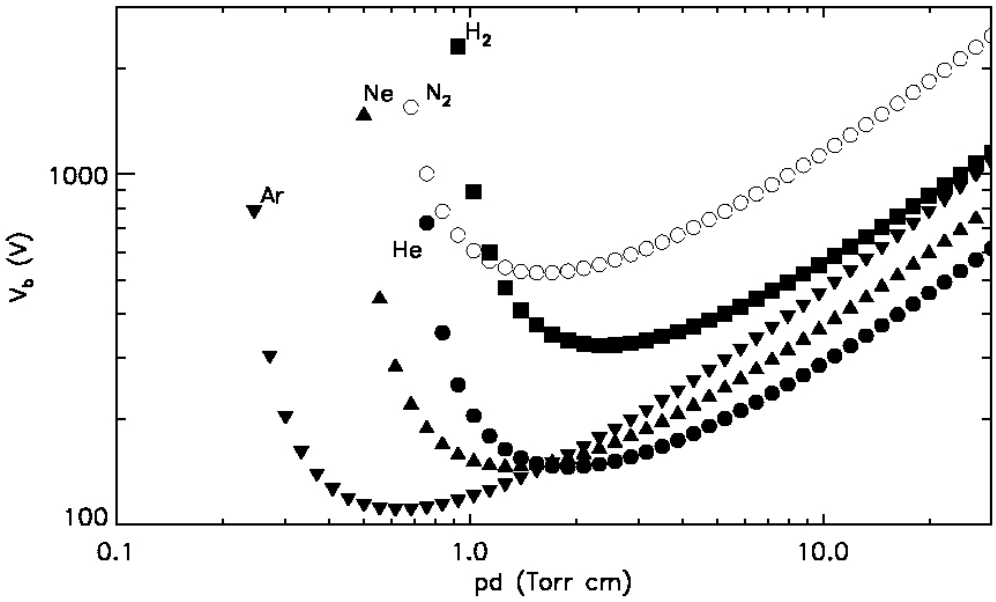

Figure 3.5: Paschen curves for various gases [4].

is the ratio of the specific heats ($\approx 5/3$ for a monoatomic gas and $\approx 7/5$ for a diatomic gas). Since $p \gg p_o$ the second term in the RHS of Equation 3.2 is roughly constant, reducing the equation to $p \propto A^{-\gamma}$.

In a coaxial geometry, the characteristic arc length is $d = r_o - r_i$, where r_o is the radius of the outer electrode, and r_i is the radius of the inner electrode. The channel area is $A = \pi(r_o^2 - r_i^2)$, thus

$$pd \propto \frac{(r_o - r_i)}{(r_o^2 - r_i^2)^\gamma} \tag{3.3}$$

For $r_o \gg r_i$ (as is the case throughout the ELF gun), the inter-electrode distance is roughly $d \approx r$, and the area of the channel is $A \approx \pi r^2$. For $r_o \approx r_i$ (as in the IPA

gun), the channel area is roughly $A \approx 2\pi dr$. This enables one to write Equation 3.3 as

$$pd \propto \begin{cases} r_o^{1-2\gamma} & \text{for } r_o \gg r_i \\ r_o^{-1} d^{1-\gamma} & \text{for } r_o \approx r_i \end{cases}$$

which indicates that in order to increase the product pd, first the radius of the outer electrode must be made as small, then the radius of the inner electrode must increase. Thus, the best way to improve the performance of the gun was to increase the product pd within the region that the arc initiates, hence the small radius of the outer electrode where the arc initiates in the ELF gun.

Operating as near as possible to the Paschen minimum not only helps in breaking down the gas, but also helps the dependability of the time of breakdown. The total time delay between the application of voltage and the breakdown of gas between the electrodes is typically expressed as the sum of the statistical time delay and the formative time delay ($t_d = t_s + t_f$) [29]. It becomes apparent when one examines the current trace in the PI, that the statistical delay time is of much greater concern than the formative time. The likelihood of breakdown occurring within a given time after the initial application of voltage goes like [30, 31]

$$t_s = 1/PN_{\mathrm{o}} \tag{3.4}$$

where

$$P = \begin{cases} 0 & \text{for } q < 1 \\ 1 - 1/q & \text{for } q > 1 \end{cases}$$

and

$$q = \gamma e^{\eta(V - V_o) - 1} \tag{3.5}$$

Where P is the probability of one electron initiating the breakdown, N_o is the number of electrons escaping from the cathode into the gas per second, V is the voltage applied to the electrodes, V_o is the voltage needed to impart enough energy to an electron to ionize the gas, η is the primary ionization coefficient, and γ is the secondary ionization coefficient. Thus the further above the breakdown voltage, the more likely the breakdown is to occur in a short time after the trigger.

This dependence can be seen in Figure 3.6, and in plots of the current vs. time in the PI for shots with varying line pressure (Figure 3.7). One notices that even at higher pressures there are still some shots for which the arc takes tens of microseconds to initiate. This uncertainty in breakdown time requires that several shots be taken at any measured data point in order to estimate the repeatability of the shot, especially at conditions with lower pressures between the electrodes at the time of triggering.

3.2 PI Location

Since the construction of the PI allows for (relatively) easy axial repositioning, the effect of changes to this parameter were investigated. Specifically of interest was

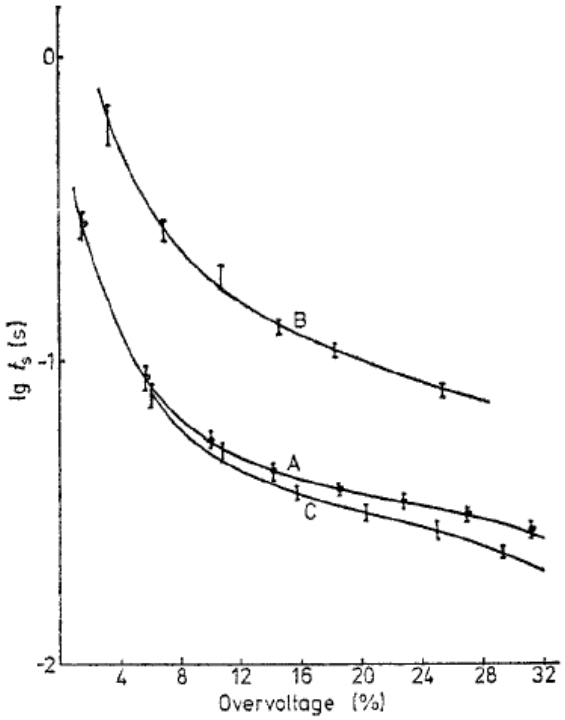

Figure 3.6: Time delay of breakdown as a function of over-voltage. [31]

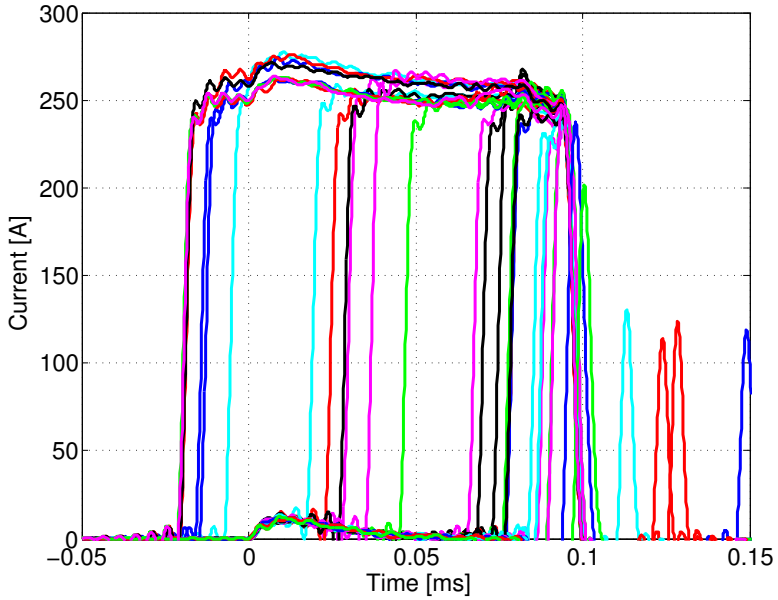

(a) 0 psig

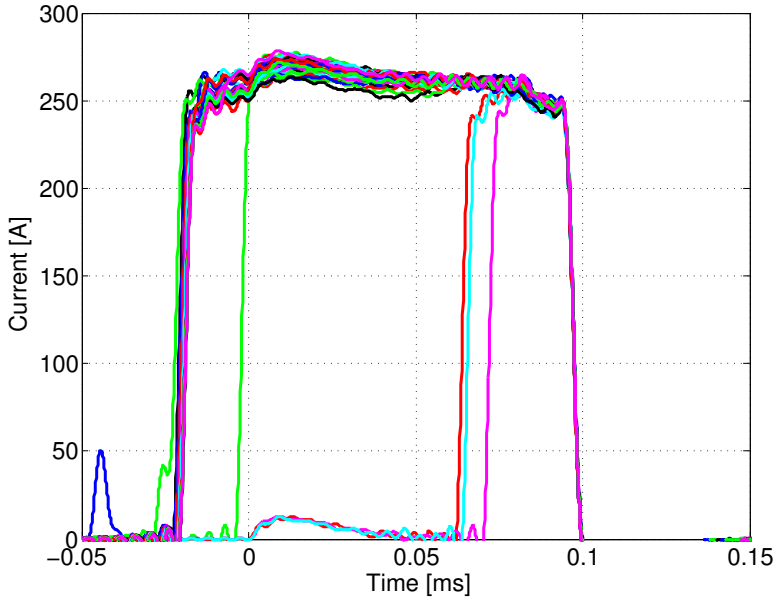

(b) 20 psig

Figure 3.7: The current in the PI for 0 psig and 20 psig line pressures

the effect of axial position relative to the location of the RMF antennae. Previous experiments have shown that plasma originating from a region outside the RMF antennae experienced current drive as a result of interactions with the fringe fields of the antennae. The retention of these field lines impeded the traslation of the plasma into the region beneath the antennae, preventing upstream plasma from flowing into the RMF section, and forming a plug [32]. These results, however, were attained with a completely ionized plasma streaming into a hard vacuum within the RMF region. It was unclear whether this would occur in ELF, where the streaming gas has a low ionization fraction and there is an ample supply of neutrals already within the RMF region. It was also unclear whether or not it would be detrimental for the PI to extend into the formation section, allowing it to come into physical contact with the hot plasma.

The position of the PI is denoted as the axial distance from the upstream end of the anode to the interface between the conical and cylindrical sections of the quartz vacuum boundary. Note in Figure 3.8 that the RMF antennae begin at roughly +3 cm. Four locations were investigated; -10 cm (10 cm upstream of the interface, outside the RMF section), 0 cm (even with the interface, the anode is just outside the RMF antennae and the cathode extends beneath the antennae), +5/+6 cm (both the cathode and anode are with the RMF section), and +10 cm (the gun extends further into the RMF section). The fairly coarse resolution of the scan is owed to the fact that the chamber could not be kept under vacuum while the PI was moved.

Since the timescale of the neutral gas fill is much longer than the timescales

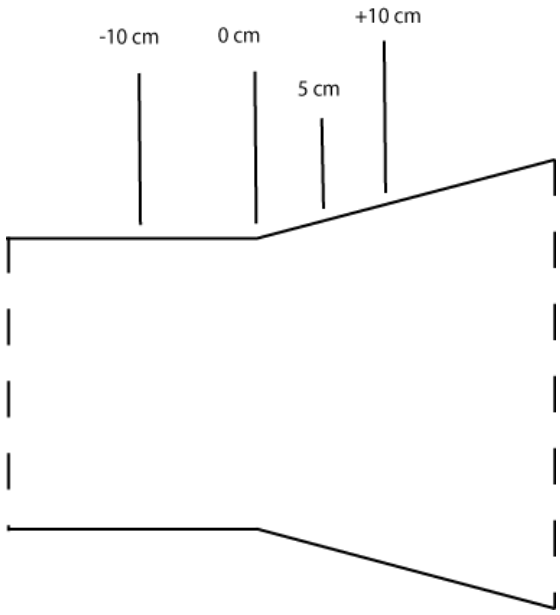

Figure 3.8: Possible PI locations.

of the discharge, a puff timing sweep was performed at each position in order to make an accurate comparison of cases. Since it is believed that the addition of the adjustable bias provides several effects which enhance the uniformity of the discharge and the impulse produced (see Section 3.5), an investigation into the effect of axial position with no adjustable bias present provided the highest sensitivity to non-uniformities that could be deleterious to the operation of the thruster.

Figure 3.9 illustrates that there is little difference in impulse between the -10 cm and the 0 cm positions, indicating that the plasma-plug issue mentioned above is not a problem. There are key differences between the earlier experiment and ELF that prevent this behavior from occurring. In the earlier experiment, the plasma injected into the RMF region was completely ionized and was entering into

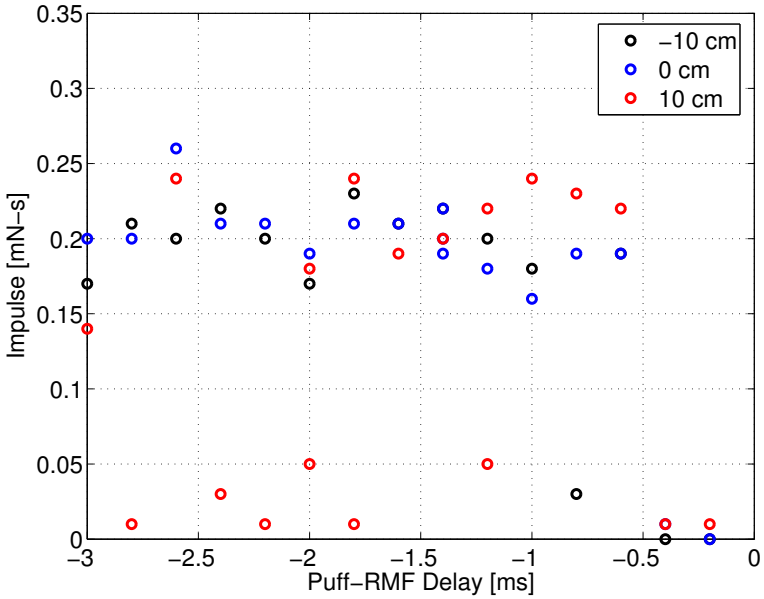

Figure 3.9: Puff sweep at three axial positions with the adjustable bias set to zero.

a hard vacuum where there was a high level of RMF already present. In ELF, there is already an ample supply of neutral gas in the RMF region with only a few seed electrons needed to initiate the breakdown; there is no need for significant quantities of gas to flow across the boundary. Also, the incoming gas enters into the RMF section before there is a significant amount of rotating field present, and it is only partially ionized, so there is less chance for a strong interaction to occur before the RMF section is seeded.

At the +10 cm position, the discharge occasionally fails to occur. This is thought to be due to the collimation of the plasma emanating from the PI. When the PI is further upstream, more flux is mapped to the PI, which then spreads out as the the plasma travels downstream. In addition, the further the plasma has to travel within the RMF section, the more time it has to make collisions and cross

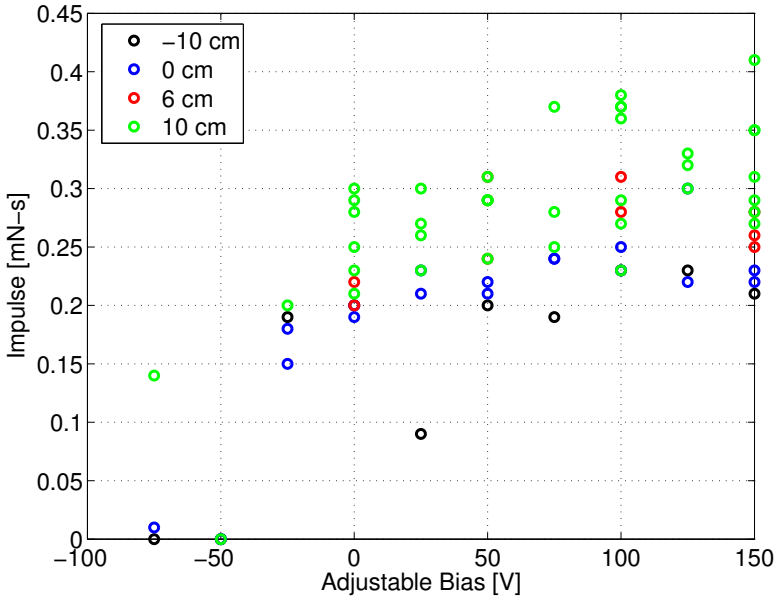

Figure 3.10: Adjustable bias sweep at several axial positions.

magnetic field lines, especially since it is traveling through a background of neutral gas. There is also one case in which the -10 cm position fails to discharge, this could be due to the increased time required for the gas to fill the RMF section.

Since the optimal setting for the adjustable bias was not yet known, a characteristic puff timing for each location was chosen, and an adjustable bias sweep was performed. For the -10 cm and 0 cm positions, the chosen puff timing was -1.4 ms. For the +5/+6 cm and +10 cm positions the chosen puff timing was -1 ms.

In all axial locations there is a clear trend of increasing impulse as the adjustable bias is increased (see Figure 3.10), the reasons for this are discussed in Section 3.5. Again, the +10 cm position produces the largest amount of impulse, however, it also exhibits the highest degree of uncertainty. The -10 cm position produces slightly less impulse than the 0 and +6 cm positions, and there are cases when the

discharge fails to occur properly resulting in a significant reduction of impulse.

It can be seen in Figure 3.9 that for the chosen puff timings of Figure 3.10, the +10 cm position produces an above average impulse, and the -10 cm position produces a below average impulse. Thus the relative magnitude of the impulse produced at each position as observed in Figure 3.10 is not a function position, but rather of puff timing. The object of the adjustable bias sweep was to compare the characteristics of the discharge as a function of adjustable bias level, and identify an attractive level at which to then perform a second puff timing sweep.

Thus far, the discharges from PI positions of 0 cm and +6 cm have demonstrated the highest level of consistency and reliability. Despite the unreliable performance presumably due to issues of plasma spread, the +10 cm position has produced the highest levels of impulse. The -10 cm location, however, has produced the least impulse of any position with no increase in reproducibility. This makes sense when one considers the fact that upstream of the 0 cm position, the axial field is constant, so the amount of flux that is mapped to the electrodes of the PI does not increase as it is positioned further upstream. Also, there is little sense in injecting gas upstream of the RMF section where there is no energy addition to the gas.

Shown in Figure 3.11 is a puff timing sweep for 3 axial positions while the adjustable bias is set to 125 V. This bias condition was chosen because it lay at the high impulse end of the trend observed in Figure 3.10, and any additional bias decreases the impulse at all positions. The -10 cm position was not tested for reasons mentioned above.

As in Figure 3.9, the +10 cm position has markedly higher impulse than the

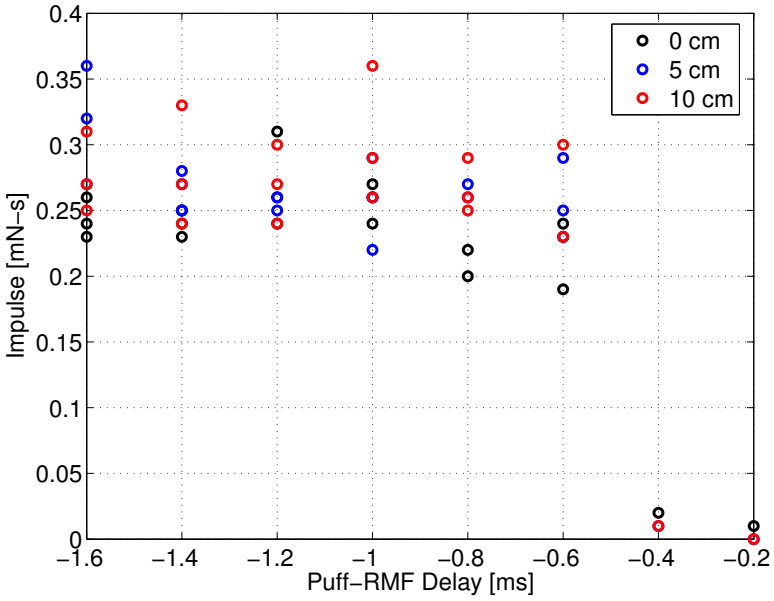

Figure 3.11: Puff sweep at three positions with adjustable bias set to 125 V.

0 cm position times between -1 and 0 ms, but one can also observe that the +5 cm position also produces high levels of impulse at these times. Due to the increased reproducibility compared to the +10 cm position, the +5/+6 cm position is a logical choice to use for future tests.

3.3 Neutral Gas Flow

The process of FRC formation and acceleration in ELF has proven to be very sensitive to the initial distribution of neutral particles (see Section 3.9). Thus, it is important to gain an understanding of the initial distribution of neutral particles within the experiment prior to the occurrence of the discharge. To this end, testing was performed using the Fast Ion Gauge (FIG) (see Section 2.6.2) and the capac-

itance manometer (see Section 2.6.1). The presence of a magnetic field interferes with the operation of the FIG (see Section 2.6.2), so all measurements were taken while triggering only the puff valve. Since there is the potential that the behavior of the puff valve will change with the addition of the bias field (see Section 2.3), the total gas released by the valve, as measured by the capacitance manometer, was compared in cases with and without the bias field present in order to confirm that the amount of gas released by the valve was consistent in each case.

Due to the axisymmetric nature of the distribution, the density at larger radii contributes more to the total number of particles than the density on axis. Unless specified, the density was measured at a radius of 12.4 cm, and at an axial position of +50 cm (near the end of the copper flux conserver described in Section 2.2). In order to determine the radial distribution of the neutral gas, FIG measurements were taken at several radii (see Figure 3.12). It can be seen that the density is uniform to within the uncertainty of the measurement at all times. This alleviates concerns that the neutral gas does not spread out enough for the RMF to drive a large current and that an annular gas source would be needed.

An examination of a typical FIG trace reveals that the leading edge of the gas pulse arrives at the FIG roughly 1 ms after the puff is initiated. The pressure then rises dramatically over the next few milliseconds, peaks, and falls to the equilibrium value over roughly 50 ms (see Figures 3.13, 3.14, 3.12, 3.15). These timescales (milliseconds) are much longer than the typical plasma timescales (microseconds). Therefore, no appreciable amount of gas flows into the RMF section during the discharge process. The FRC consists only of gas that is residing in the cone prior

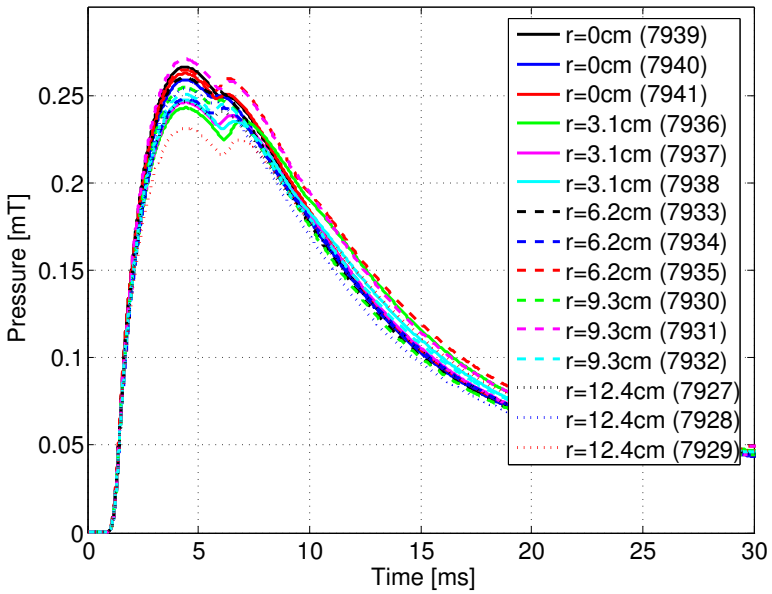

(a) Neutral gas at various radii.

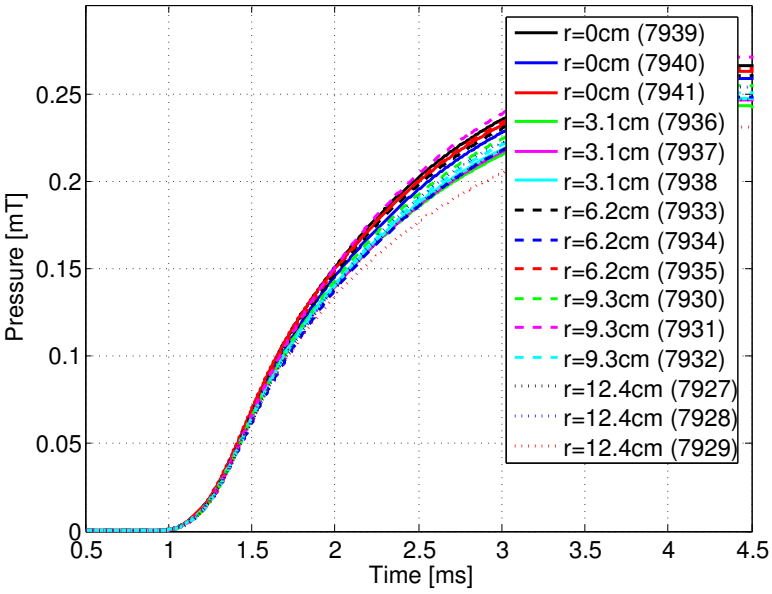

(b) Leading edge.

Figure 3.12: Neutral gas pressures measured at various radial positions.

to the discharge. When an FRC is ejected, the cone is evacuated. Gas continues to stream from the PI, and eventually refills the cone, allowing for subsequent discharges.

Since only some of the gas is used on the first discharge, if this type of gas feed configuration were to be used in a real-world thruster, it would need to operate on a duty cycle: several discharges in quick succession for every puff, with the power level being determined by the puff frequency. In this scenario, at the maximum power level, the puff valve would be left open and gas would stream into the thruster continuously (corresponding to a 100 % duty cycle).

While shots in which multiple discharges were initiated from a single puff have been performed, demonstrating that this type of operation is possible (see Figure 3.16), the RMF supplies were not designed with this in mind, and the energy of the subsequent discharges is diminished. The ELF experiment investigates the feasibility of a thruster operating along these concepts, however, the full realization of this mode of operation is beyond the scope of the current experimental program.

In order to operate as a thruster would in space and conserve propellant, it is necessary to maintain a hard vacuum at the exhaust while filling the RMF section with gas. To best accomplish this, the rise time of the gas pulse (as seen by the FIG) should be as short as possible compared to the time it takes for the gas to transit the RMF section. In an attempt to steepen the leading edge of the pulse, the puff valve was driven at voltages much higher than the recommended 12 V. FIG traces were obtained for driver voltages of 200 V, 400 V, and 600 V (the maximum of the driver). It can be seen in Figure 3.13b that the leading edge of the pulse

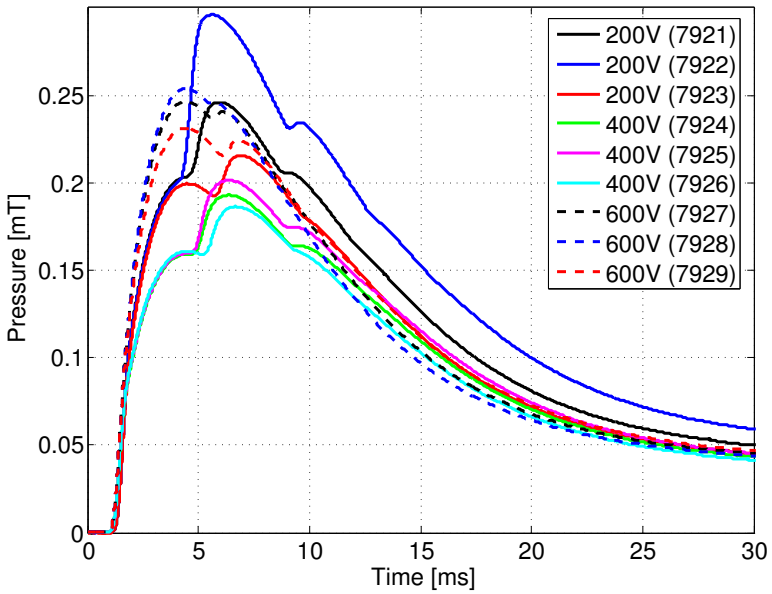

(a) Neutral density trace for various driver voltages.

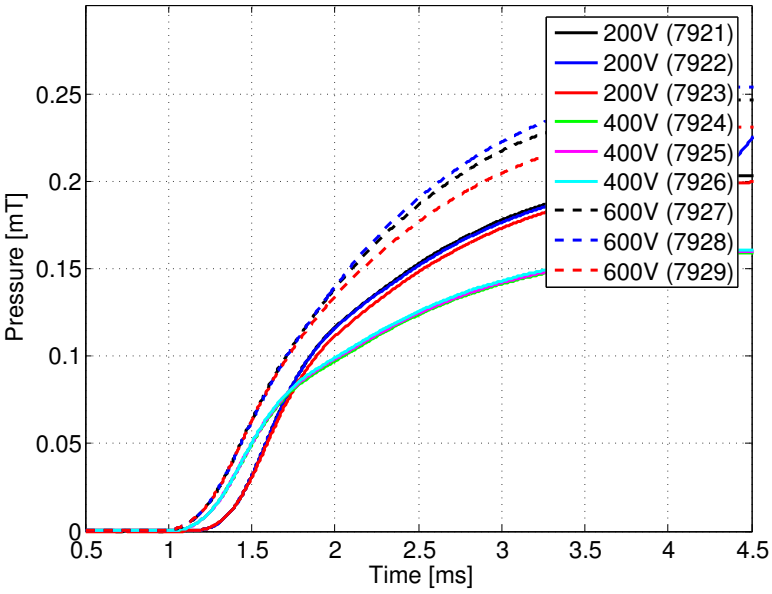

(b) Leading edge.

Figure 3.13: Varying the driver voltage changes the behavior of the puff valve.

is the steepest when 600 V are used, corresponding to a steeper density gradient, and the capacity to fill to higher densities while maintaining a hard vacuum at the exhaust. One can also notice that the multiple puff behavior is diminished when 600 V is used.

Experimentally, the gas emanating from the cone after the discharge imparts additional momentum to the pendulum. When determining the momentum of the FRC, the impulse from a pulse of neutral gas must be subtracted from the measured impulse during a plasma discharge. To minimize the additional impulse from the neutral gas, the puff duration is shortened as much as possible. However, the puff valve can behave in unexpected ways as it is pushed to the limits of its operation.

As the duration of the puff is varied, the shape of the gas pulse changes in an unpredictable manner (see Figure 3.14). In in the majority of the settings investigated, multiple gas puffs can be observed. It is thought that this is due to bouncing of the armature and poppet, resulting from the large driving forces and small timescales of operation. Since any additional gas releases occur long after the discharge has taken place, they only serve to obfuscate the impulse measured by the pendulum. Therefore, during the vast majority of testing that took place, a puff duration of 420 μs was used. This setting produced the highest instantaneous density at the FIG while releasing the least amount of total gas (as determined by the final pressure), and exhibited relatively small secondary puffs. Also, any perturbations to the puff duration do not result in a severe departure from expected behavior as is the case with the shorter timings.

With the puff duration set, the amount of gas released by the puff valve can be

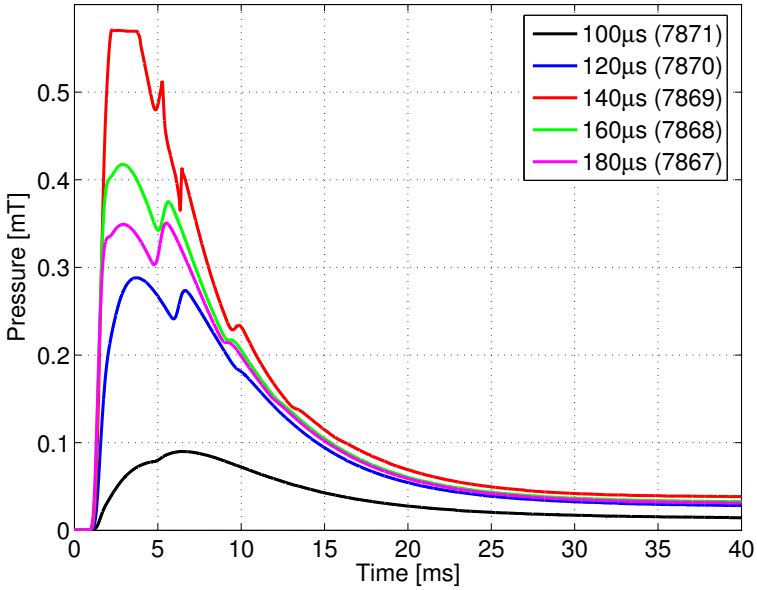

(a) Various puff durations.

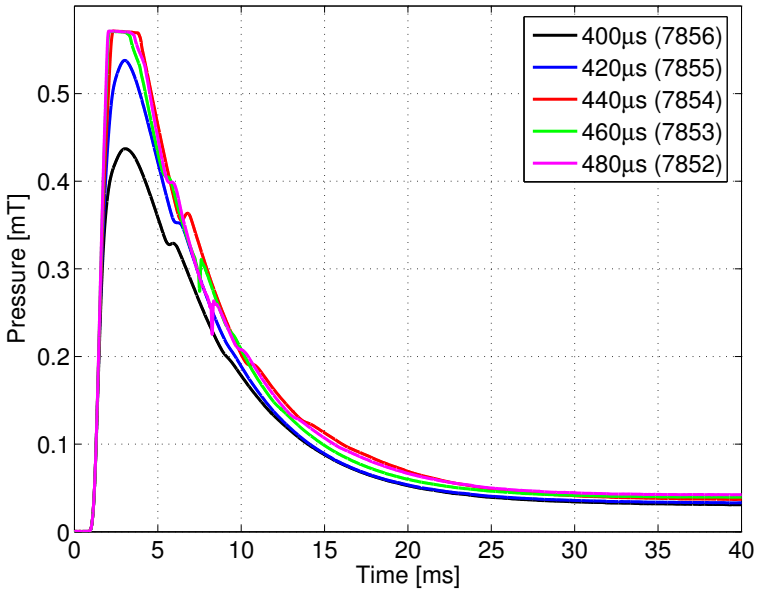

(b) Various puff durations.

Figure 3.14: Gas output of puff valve triggered for varying durations.

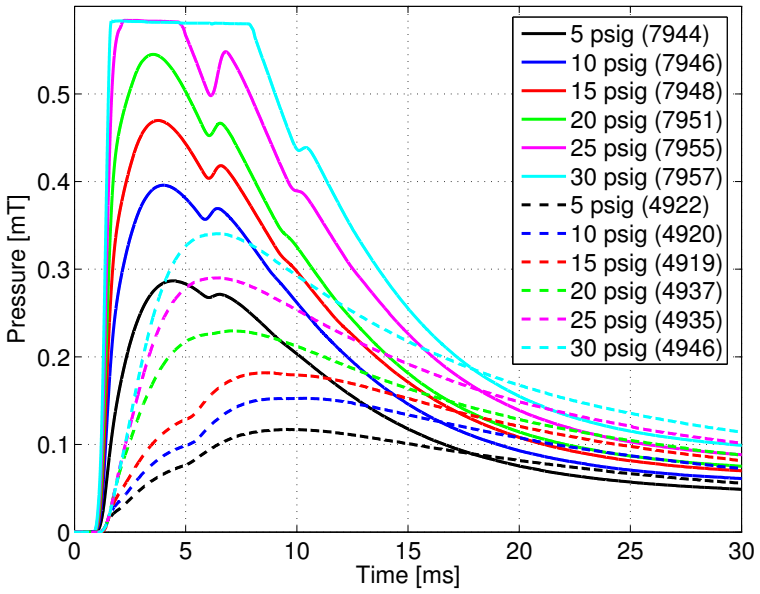

(a) Neutral density trace for various line pressures.

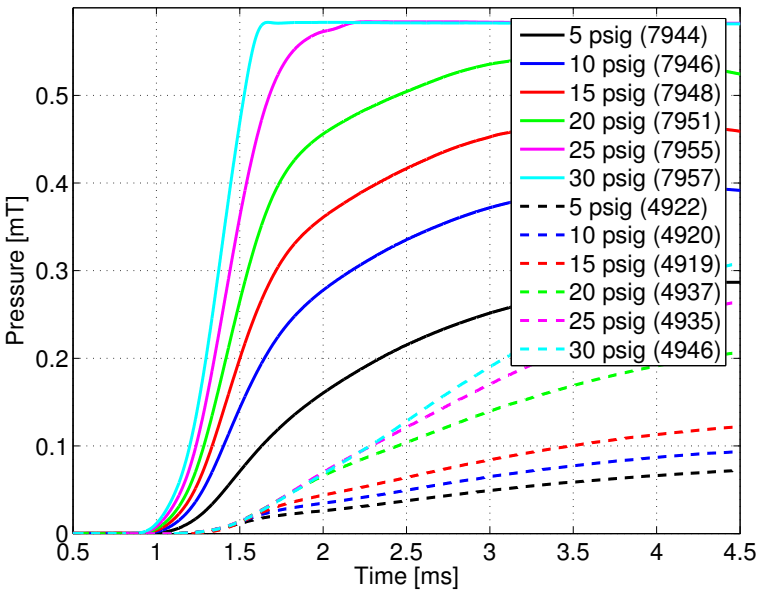

(b) Leading edge.

Figure 3.15: Varying the line pressure with and without the gas shield in place (solid lines indicate tests with the shield, dashed lines indicate tests without the shield). These measurements were taken on axis.

controlled by varying the pressure of the gas line upstream of the puff valve (see Figure 3.15). The St. Venant equation, resulting from the conservation of mass and energy along the length of a nozzle, expresses the mass flow rate in a choked nozzle flow in terms of the density and pressure at the enterance of the nozzle (p_o, ρ_o) and a specified location (A, p, ρ). Choosing the location to be the throat (A^*, p^*), and expressing the pressure ratio as a function of the Mach number, it becomes clear that the mass flow rate varies linearly with the line pressure [33].

$$\dot{m} = A\sqrt{\frac{2\gamma}{\gamma-1}p_o\rho_o\left(\frac{p}{p_o}\right)^{2/\gamma}\left[1-\left(\frac{p}{p_o}\right)^{(\gamma-1)/\gamma}\right]} \tag{3.6}$$

$$\frac{p}{p_o} = \left(1+\frac{\gamma-1}{2}M^2\right)^{-\gamma/(\gamma-1)} \tag{3.7}$$

$$\dot{m} = A^*\sqrt{p_o\rho_o\gamma\left(\frac{2}{\gamma+1}\right)^{(\gamma+1)/(\gamma-1)}} \tag{3.8}$$

$$\dot{m} = A^*p_o\sqrt{\frac{m\gamma}{kT}\left(\frac{2}{\gamma+1}\right)^{(\gamma+1)/(\gamma-1)}} \tag{3.9}$$

The measured pressures as seen in Figure 3.15 appear to be consistent with this scaling. Most importantly, however, manipulation of the line pressure is a simple, high resolution means for scaling the density profile in the cone prior to the discharge.

Upon the addition of the cylindrical section with the axially mobile PI, it was noticed that some of the gas was filling the volume behind the PI before flowing out of the cone. This resulted in spread out gas pulse with a slowly rising leading edge.

In order to prevent this from occurring, a PVC shield was installed just upstream of the interface between the cylindrical and conical sections (see Section 2.3). It can be seen in Figure 3.15 that this resulted in a more compact gas pulse with a much sharper leading edge. Thus it required less line pressure to achieve the same density profile in the cone, resulting in an increased fraction of the gas used to form the FRC.

3.4 RMF Duration

The RMF system in ELF is designed to form FRCs in a pulsed manner rather than the gradual build up and sustainment process used in previous RMF experiments (see Section 2.4), however, apart from this somewhat vague notion, not very much was known about how best to carry out the formation process with the available hardware. Initial testing consisted of injecting gas and firing the PI while operating the RMF as long as there was energy available in the RF supply banks (see Figure 3.16). This testing revealed details about the formation process that could be used to refine the operation of the thruster.

It can be seen (in Figure 3.16a) that the RMF ramps up first to a high amplitude, then as the neutral gas ionizes, the amplitude becomes quickly reduced. Upon examining the energy in the tank circuit (plotted in Figure 3.16b), one can see that almost all of the circulating energy is absorbed by the plasma over a very short time. The RF supply continues to add energy to the tank, however, it quickly is absorbed by the plasma, thus keeping the amplitude of the tank circuit relatively

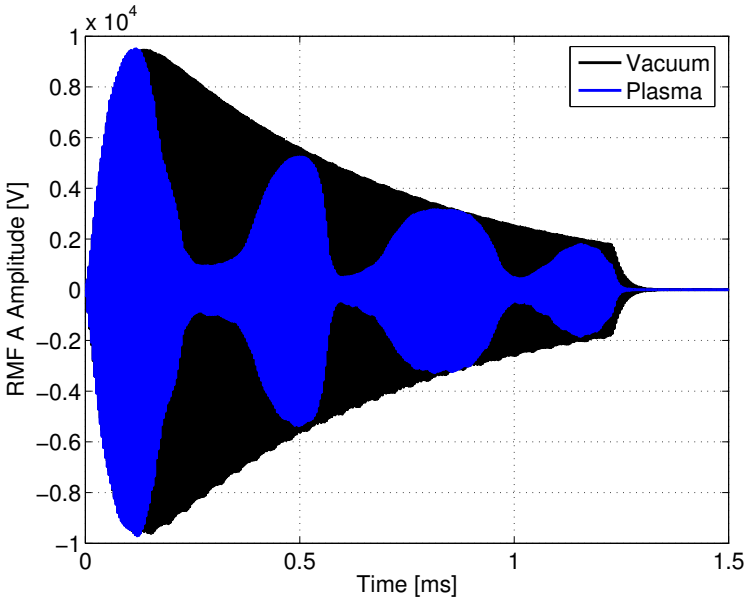

(a) Voltage on the capacitor of the tank circuit.

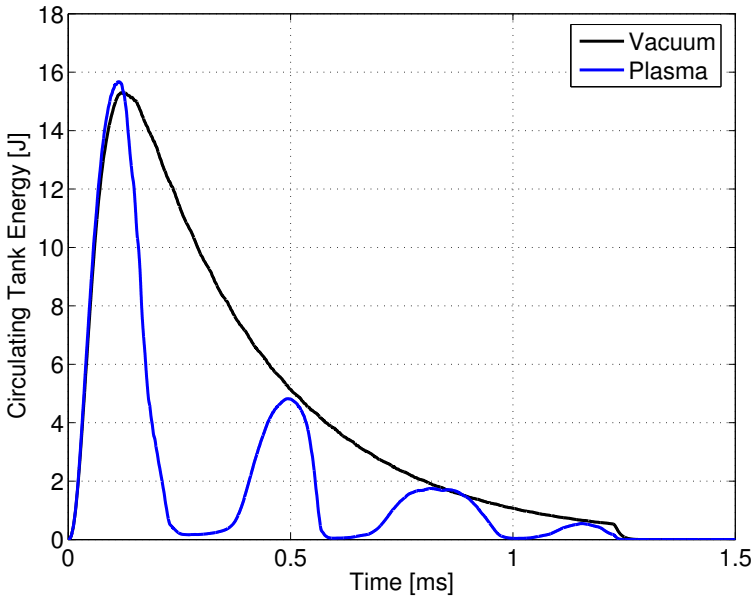

(b) Circulating energy in both RMF tank circuits is significantly reduced during subsequent discharges.

Figure 3.16: RMF tank voltage and circulating energy for a vacuum shot and a multiple discharge plasma shot.

low until enough plasma has left the cone to reduce the energy absorption rate. At this point, the RMF amplitude begins to increase again, the RF supply adding energy to the tank circuit, while neutral gas continuously streams into the cone. When the RMF amplitude gets high enough, the neutral gas in the cone undergoes a second cascading ionization process (aided by any remaining ionized particles), absorbing the energy circulating in the tank, and reducing the RMF amplitude. This process repeats itself until either the energy in the RF supply or the neutral gas is exhausted.

When less neutral gas is released by the puff valve and the density within the cone is low, the RMF loading is observed to be incomplete, only partially reducing the circulating energy in the tank. In this situation, there is not enough current driven to reverse the axial magnetic field when the bias is high, and the result is a magnetized, low-density jet of plasma, this mode of operation was not further investigated. While this mode may be capable of generating a stream of high velocity plasma, it is the intent of the ELF program to develop a thruster in which the plasma is isolated from the magnetic field of the thruster and resides on its own self-generated field lines to prevent the deleterious effects of incomplete magnetic detachment.

It has been observed that, with an adequate gas supply, the RMF can deposit almost all of the circulating energy stored in the tank within a few RMF oscillations. This energy distributes itself between magnetic and thermal components over collision timescales to form an FRC with similar properties as that described in Section 1.3 with gas pressure at the field null and magnetic pressure at the sep-

aratrix. This FRC is not strictly in radial equilibrium, but the energy deposition and equilibration timescales are shorter than the translation/expansion timescales which are, in turn, shorter than the flux and particle loss timescales (see Section 3.7), thus the configuration this FRC is similar that of one in radial equilibrium.

Examination of the external and internal probe traces reveals that the FRC is formed and is ejected from the thruster within a small span of time (tens of microseconds). This occurs at roughly the same time that the majority of the circulating energy is absorbed from the tank circuit. Once the FRC has been ejected from the cone, there is a trace amount of magnetized plasma left behind in which the RMF can deposit energy (seen during the relatively constant, low-amplitude region of the RMF trace). This low-density plasma is capable of absorbing significant amounts of energy while producing relatively little additional useful thrust before eventually being cleared from the cone. In addition to this non-useful expenditure of energy in the plasma, there are also non-trivial losses incurred as energy is resistively dissipated in the tank and RF supply circuits. Over time, these losses can easily come to dominate the total energy of the FRC.

While rapid plasmoid ejection is the intended purpose of this thruster, ringing the RMF continuously is not necessarily the optimal way to achieve this. Under the current configuration, the most efficient way to operate the thruster is to ramp up the RMF until it approaches the desired amplitude, then trigger the PI, which initiates the ionization of the neutral gas. Once the FRC has formed and consumed the energy circulating in the tank circuit, the RMF drive must be disengaged until enough neutral gas has re-filled the cone for the process to be repeated.

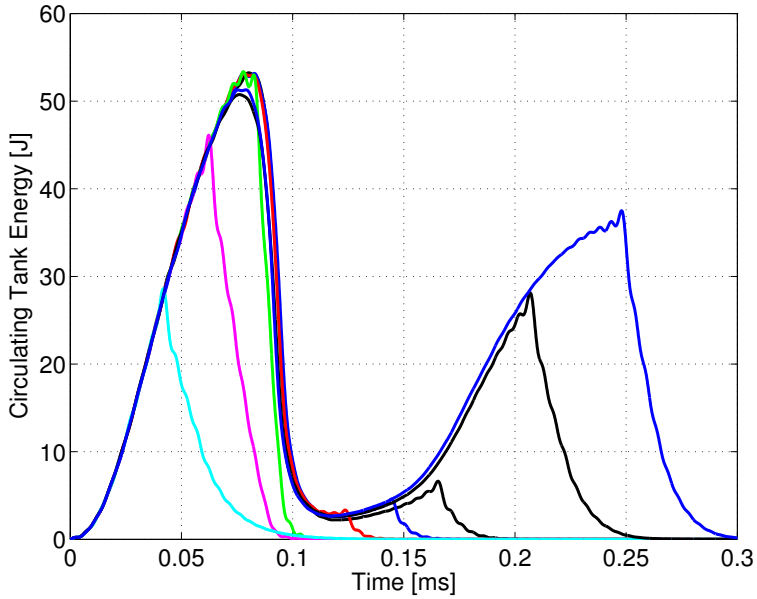

(a) Tank energy for varying RMF durations.

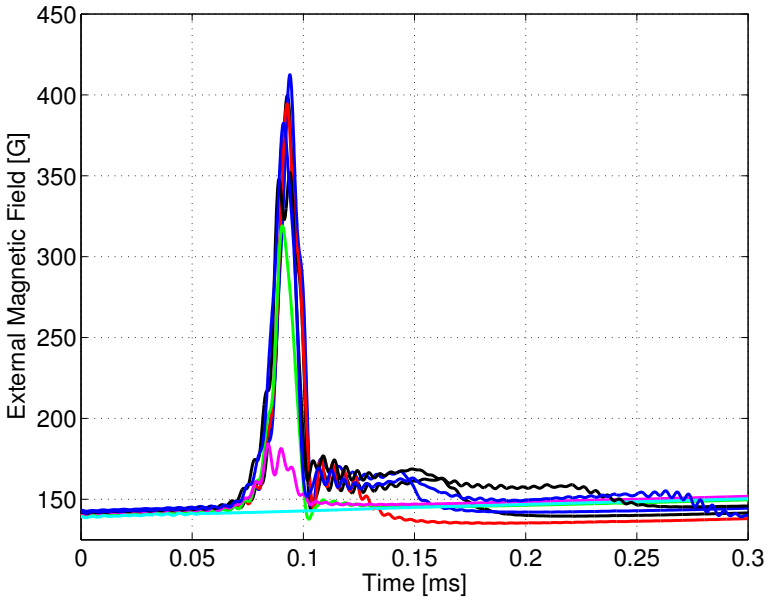

(b) FRC generated only during the initial RMF loading period.

Figure 3.17: The effect of varying the RMF duration for a single FRC discharge.

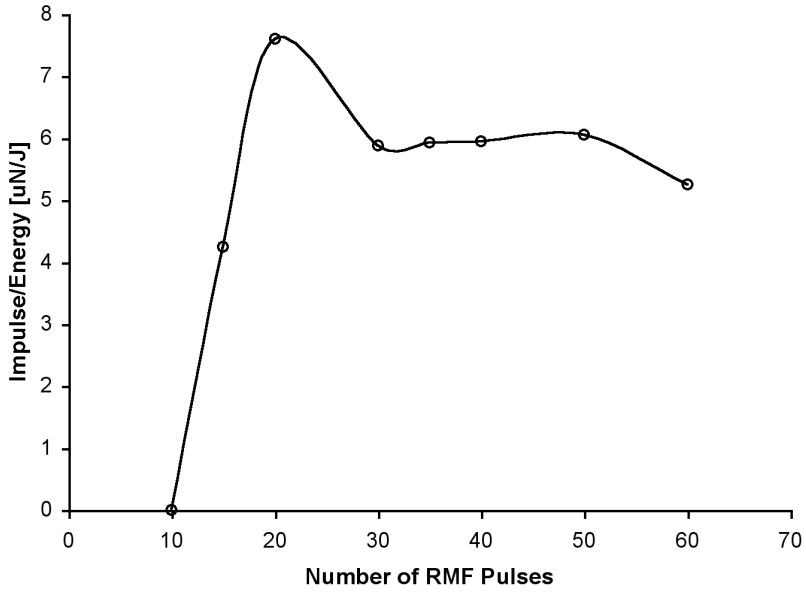

Figure 3.18: Thrust generated for varying RMF durations.

In a real-world application, the energy supplied to the thruster would be constant over time. However, in the case of ELF, the energy of the RF supply bank decays over time, this can be seen in Figure 3.16b. Because of this, only one discharge is possible at maximum energy, with all subsequent discharges occuring at lower energy levels. Thus, the ELF experiment is only able to produce one realistic FRC before recharging the capacitor banks. However, due to the pulsed nature of the thruster, one can gain a significant understanding of the dynamics of the thruster by studying variations of the single discharge shot.

In order to determine the most efficient time to disengage the RMF after the FRC has been ejected, several shots were performed in which the number of RMF pulses was varied while observing the change in impulse produced. Figure 3.18 shows the impulse per energy input as a function of the number of RMF pulses (the

energy into the plasma is computed using the SPICE model described in Section 2.6.6). A maximum is reached when the RMF is maintained until just after the FRC has absorbed the circulating energy in the tank, but before the RF supply can provide much more additional energy, this point is usually reached $\sim$ 85 μs after the RMF is triggered ($\sim$ 20 RMF pulses, see Figure 3.17a).

Since the number of RMF pulses is set prior to the shot, in order to achieve a good efficiency, the time at which breakdown occurs must be consistent from shot to shot. Since this is not the case, the number of driven RMF oscillations is not completely consistent over multiple shots, resulting in a slight spread in the amount of thrust generated. The adopted solution to this has been to take 5 shots at each data point, with the main source of error in the experiment arises from these inconsistencies in the time of RMF ionization.

3.5 Adjustable Bias

Over the course of the development of PI systems in earlier experiments, it was noticed that the ELF-type MPD plasma source is capable of producing a very collimated flow of plasma (as can be seen in Figure 3.19). In the pictured case, the guns were run at much higher current and in a slightly higher magnetic field than is typically the case in ELF. However, it was thought that the plasma produced by the ELF source may be too collimated to effectively facilitate the breakdown of the neutral gas by the RMF. This, coupled with the fact that the breakdown time of the PI is not always consistent, could account for the observed spread in the time

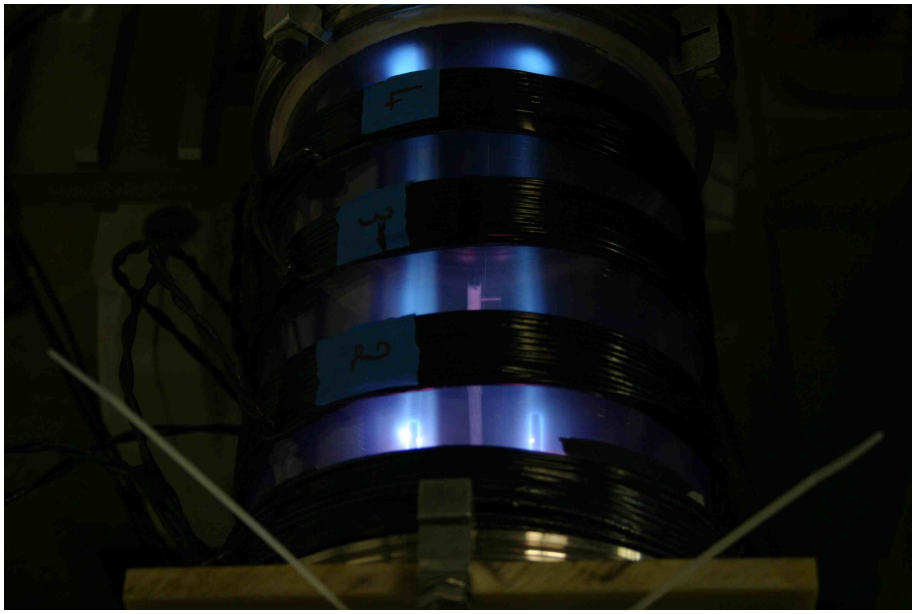

Figure 3.19: Collimated flow emanating from two adjacent ELF-type discharges in a previous experiment.

of breakdown initiated by the RMF.

A major unknown factor in the development of ELF was the optimal pitch angle of the conical section. The optimal angle must be between 0 (cylindrical tube), where there is no conversion of transverse to axial motion, and 90 degrees (annular disc), where expansion occurs essentially in all dimensions. Obviously, this is something that is not easily altered, but it may be critical to efficient operation.

Both of these issues were be studied through the use of an additional bias coil located near the small end of the cone, in the vicinity of the PI. The magnet, which is powered by a separate capacitor bank (described in Section 2.2), is capable of being repositioned axially, and hence is referred to as the adjustable bias. This enables some degree of control over the axial bias profile by changing the position

and charge voltage of the the adjustable bias relative to the fixed cone bias. The effect of the adjustable bias on the axial magnetic field can be seen in Figure 3.20 (since the value of the magnetic field varies throughout the cone, the different levels will be referred to by the charge voltage on the capacitor bank).

It was initially thought that the addition of the adjustable bias would decrease the variation in RMF breakdown time observed in earlier shots for two reasons. First; it was believed that the breakdown within the PI could be altered by adjusting the magnitude of the bias field near the electrodes. This would impart an azimuthal swirl to the gas via the $\mathbf{j} \times \mathbf{B}$ force (radial $\mathbf{j}$, axial $\mathbf{B}$) increasing the uniformity by causing ions to orbit the cathode, rather than directly impact. Second; as the adjustable bias is increased, flux lines that spread throughout the cone are mapped directly to the electrodes of the PI (see Figure 3.20f), this allows plasma to have a large radial spread without having to depend on cross field diffusion.

It was not observed that there was any appreciable increase in the consistency of breakdown time with the addition of the adjustable bias. Also, the variation of the time of the arc in the PI for the shots plotted in Figure 3.21 is much smaller than the variation in RMF breakdown time, suggesting that inconstancies in the timing and distribution of the seed plasma is not the cause of the irregularity in the RMF breakdown time.

The addition of the adjustable bias does, however, have a large effect on the overall performance of the thruster. Once can see this clearly in Figure 3.10. Firing the PI into a cusp field (as depicted in Figure 3.20a and 3.20b) resulted in poor thrust and, in some cases, an inability of the RMF to break down the gas. This is

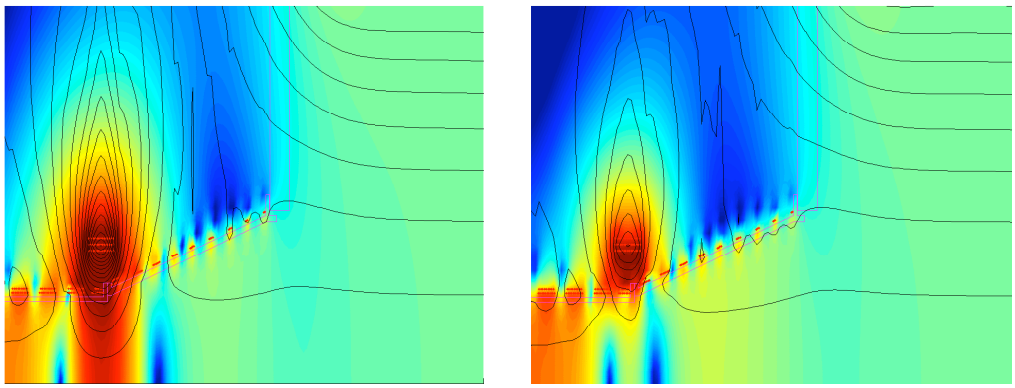

(a) Adjustable Bias at -100 V.

(b) Adjustable Bias at -50 V.

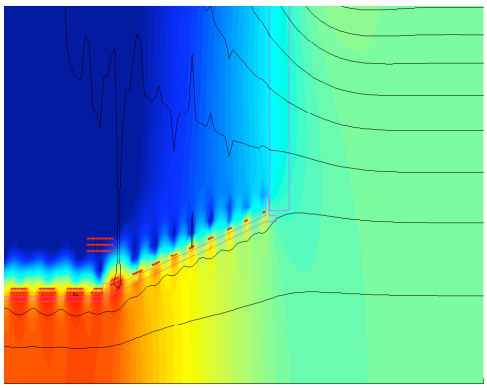

(c) Adjustable Bias at 0 V.

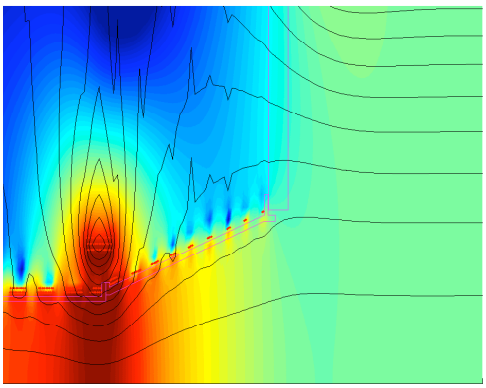

(d) Adjustable Bias at 50 V.

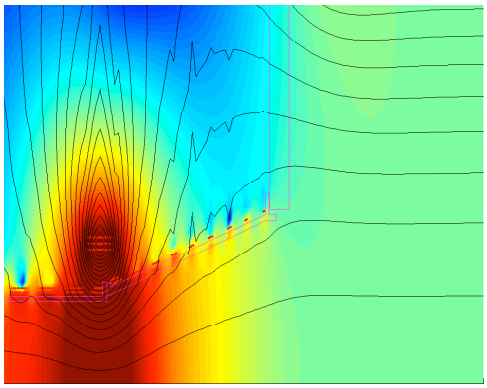

(e) Adjustable Bias at 100 V.

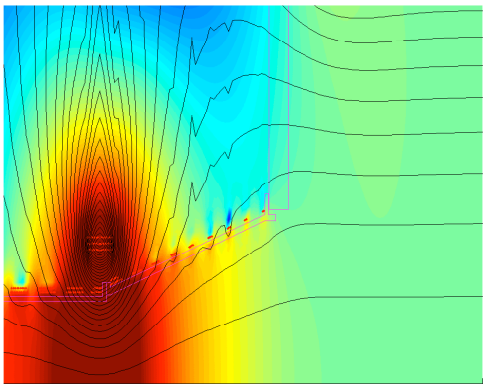

(f) Adjustable Bias at 150 V.

Figure 3.20: Effect of the Adjustable Bias at various bank voltages (lines are flux surfaces, color is $\mathrm{Log}_{10}|\mathbf{B}|$, cone bias is set to 50 V).

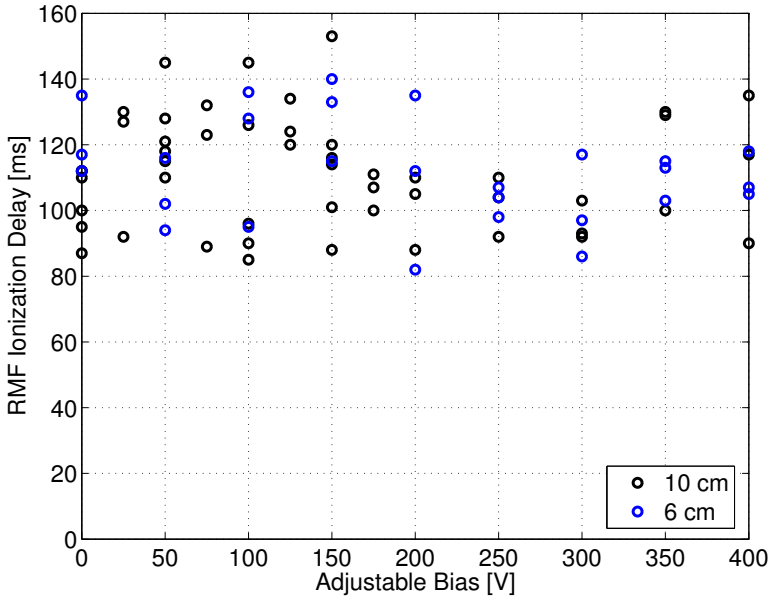

Figure 3.21: Time of RMF ionization for various adjustable bias conditions.

presumably due to the fact that the seed plasma cannot easily cross into the region of forward bias field and thus facilitate the RMF breakdown. In addition, when the adjustable bias is operated with a reversed current (cusp mode) the effect in the RMF section is to reduce the radial component of the bias field, thereby decreasing the thrust.

If the adjustable bias is operated with a forward current (Figures 3.20d-3.20f), the increase in radial magnetic field interacting with the driven current in the plasma (through the $\mathbf{j} \times \mathbf{B}$ force) increases the impulse imparted to the plasma. This process cannot, however, be increased indefinitely. Eventually, as the bias field is increased, the driven current within the plasma becomes insufficient to reverse the axial magnetic field, resulting in a high beta plasma column rather than a field reversed configuration. When this is the case, the plasma is produced on magnetic

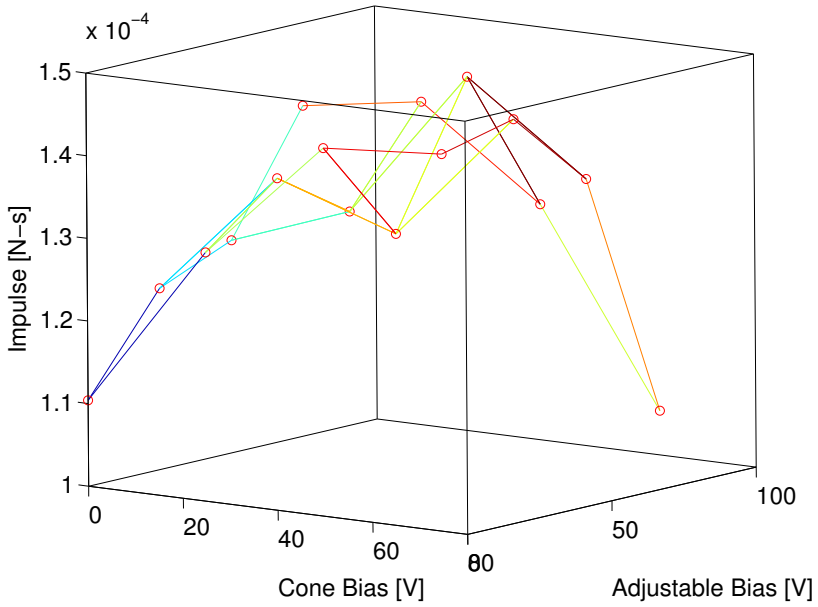

Figure 3.22: Average impulse at varying cone and adjustable bias conditions.

field lines that are tied to the thruster, and it can no longer escape to infinity without detaching from the field lines.

Figure 3.22 shows the average impulse obtained from testing at various cone and adjustable bias settings. One can see that when the two bias systems combine to form a very low or very high bias field within the cone, the impulse suffers. But when the combined field is at a medium value, the thrust is maximized.

If one examines the variation of the axial field (on axis) with time for the various bias settings, one can see that the settings with the highest field reversal and the highest field swing (corresponding to driven current) occur near the point of 50 Volts on each bias system (see Figures 3.23 and 3.24).

In light of these results, the ratio of the charge on the cone and adjustable bias banks would be set at 1:1 for all subsequent testing (nominally 50 V on each

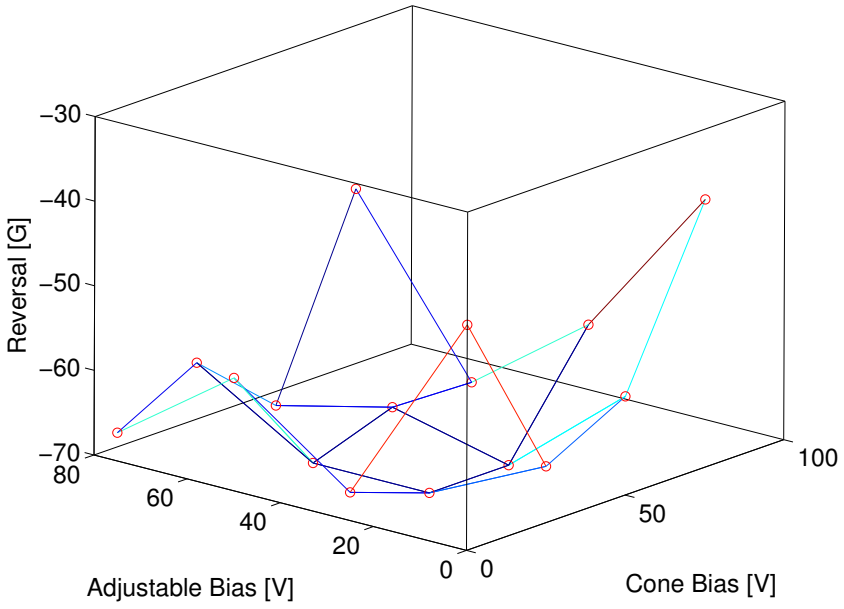

Figure 3.23: Average reversed axial field within the FRC.

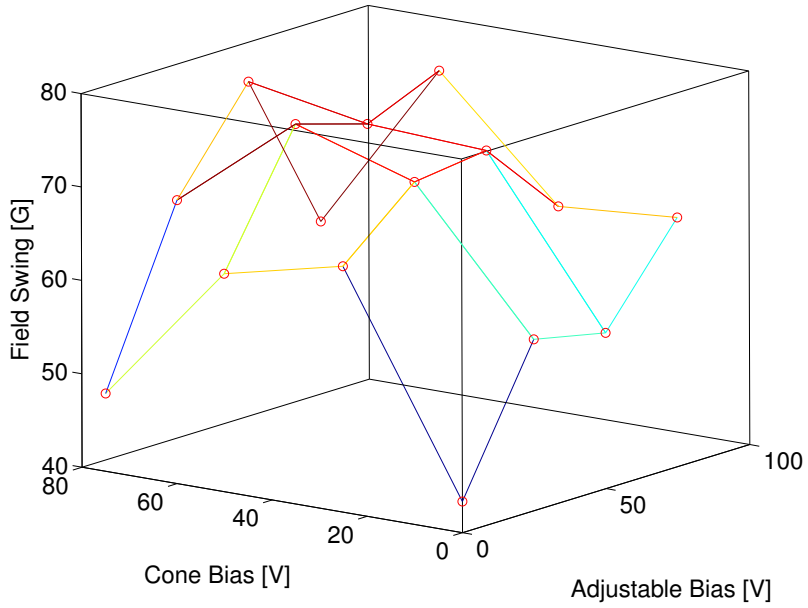

Figure 3.24: Average axial field swing due to the presence of the FRC.

bank). Later testing utilized various the charge voltages while keeping this ratio fixed. This produces an axial magnetic profile that is consistent with the intended operation of the thruster, and has provided the best thrust while maintaining good field reversal on axis, with a large azimuthal current.

3.6 PI Operation

As discussed in the previous section, it had been initially thought that the inconsistency of the time of breakdown within the PI played a part in the observed inconsistency of the time of the RMF-induced ionization event within the cone. However, it was found that the uncertainty in the time of RMF ionization was much larger than the uncertainty in the time of PI breakdown. In previous testing, it was discovered that the RMF is capable of ionizing the neutral gas without the assistance of the PI. Operating in this manner, however, resulted in very poor consistency in the time of ionization. It stood to reason that the PI could be used to trigger the RMF ionization if the correct timing could be determined.

In addition, the amount of seed plasma produced by the PI should have an affect on the RMF ionization statistical delay time by providing more free particles with which to initiate the ionization process. The production of plasma could be manipulated by changing the current that flows in the PI. This can be affected by changing the value of the ballast resistor which limits the current to the PI.

Several sweeps of the PI start time were performed using various values of ballast resistance, but there was very little effect on the consistency of the time

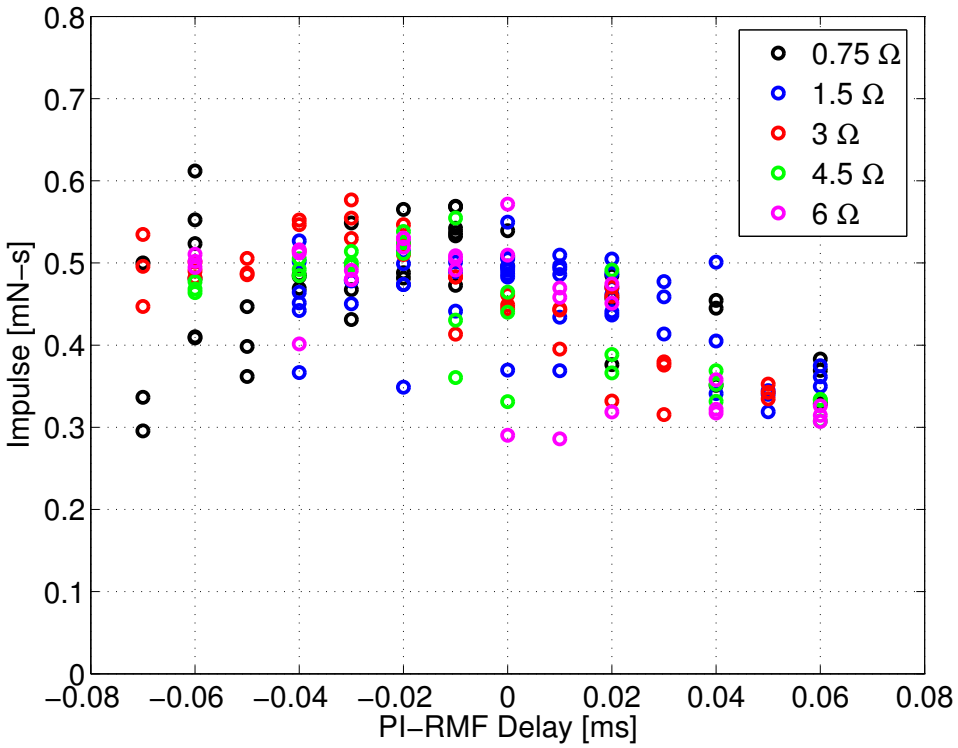

Figure 3.25: Changes in impulse as a result of the start time and current within the PI (these shots were performed using a longer RMF duration in which the impulse was indicative of the RMF breakdown time).

of the RMF ionization (see Figure 3.25). The tendency for the RMF ionization event to occur slightly later than desired necessitated sweeping the PI start time backward in time. However, even when triggering the PI before the RMF, the time of ionization was only slightly sooner than then the PI was not triggered at all. Variations in PI impedance also had a negligible effect. Eventually, it was determined that a PI start time of -25 μs and an impedance of 3 Ω resulted in the most consistent times of ionization. The PI end time was then set to +75 μs (100 μs duration) since that was roughly the time of the RMF discharge, and there was little sense in continuing the PI past that point in time.

In the ELF PI, the voltage drop across the electrodes is fairly independent of the current. Thus, the power into the plasma is proportional to the current, which is proportional to the ballast impedance. The power dissipated in the ballast is unimportant to the feasibility of the thruster concept due to the fact that a reactive ballast could be used in place of the current resistive ballast, resulting in very little power dissipation. The resistor was merely used out of convenience.

It is fortunate that an increase in PI current does not increase the impulse or effect the breakdown of the thruster. This indicates that the RMF does not need more seed ionization in order to operate effectively, and very little power needs to be spent in the PI. This also enables the use of different techniques of pre-ionization that may be more efficient or more amenable to a long operational lifetime.

Gas	N_2	**Line Pressure**	20 psig
PI Charge	950 V	**PI Impedance**	3 Ω
PI Timing	299.975-300.075 ms	**Puff Driver Charge**	600 V
PI Position	+6 cm	**Puff Timing**	299-299.42 ms
RMF Charge	600 V	**Cone Bias Charge**	50 V
RMF Start	300 ms	**Adj. Bias Charge**	50 V
RMF Duration	20 pulses	**Drift Bias Charge**	60 V

Table 3.1: Selected parameters of the standard shot.

3.7 Standard Shot

After roughly determining the characteristic settings that produce discharges in accordance with the project objectives, it became useful to define a "standard" shot; a shot using nominal settings based on the testing described in the previous sections and other testing that was not mentioned concerning every other variable parameter on the experiment. This set of parameters is not meant to define the point of optimal operation, but to provide a starting point for comparative studies in which selected parameters are varied one at a time. In the testing described in Sections (3.8-3.10), a single parameter was varied while keeping all others set to the standard shot conditions. The operational parameters of the standard shot are contained in Table 3.1. There are other parameters to the standard shot (e.g. RMF frequency), they were set relatively early on, and were held constant thereafter. These and other details of the experiment as it was during this phase of testing are detailed in Chapter 2.

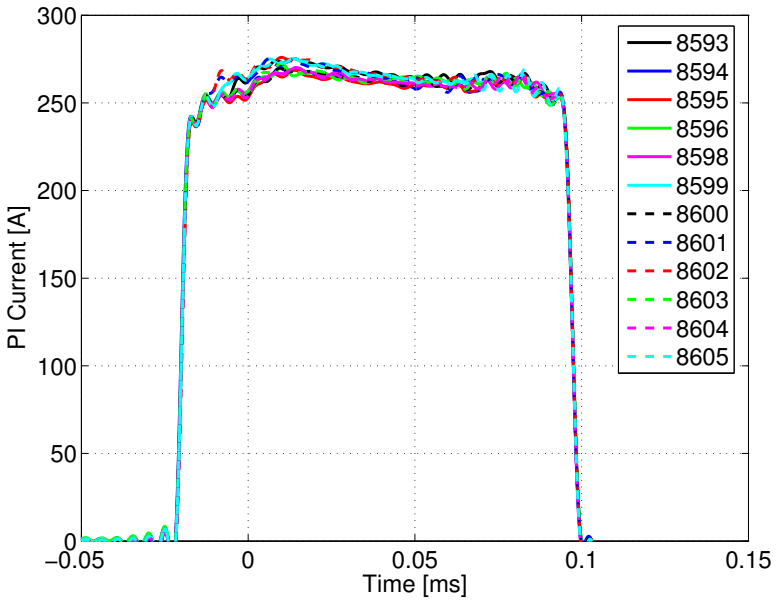

(a) PI current for several standard shots.

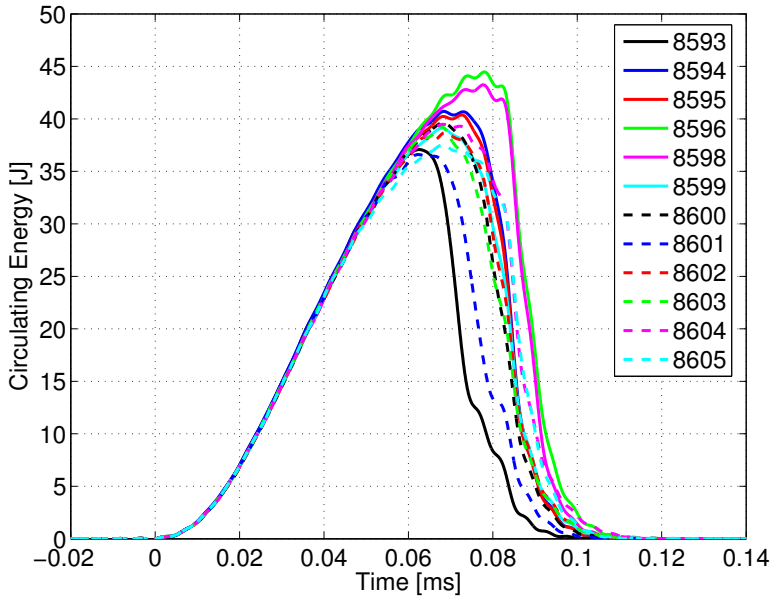

(b) RMF circulating energy for several standard shots.

Figure 3.26: The PI breakdown occurs reliably during the standard shot, however the time of RMF ionization does not

3.7.1 Formation

It has been observed that, in the standard shot, there is very little variation in the PI breakdown time, yet there is a significant variation in the time of the main RMF ionization event (see Figure 3.26). Since there is ample neutral gas present within the cone prior to the triggering of the RMF, and changes in the timing and distribution of the seed plasma is observed to have little effect on the time of ionization (as observed in Section 3.6), this would indicate that the observed variation in ionization time in the standard shot is a result of the RMF ionization process itself rather than the other experimental parameters. In addition, it was computed that the cross field particle drift, as well as the rigid body rotational speed, was insufficient to make any contribution to the ionization process. It is known that large voltages can be generated along the magnetic field lines within the formation section. The acceleration of the electrons along these field lines is thought to be the mechanism behind the RMF ionization process in ELF.

Despite irregularities in the time of RMF ionization, the details of the FRC formation process in the standard shot are fairly consistent. In all cases, the gas is ionized and current is driven in roughly the same location in the cone. The current rise times, residence times, and decay times are all very similar to one another (see Figure 3.27). One may observe that the current begins forms in the plasma roughly 50 μs after the start of the RMF, while the RMF is still at peak amplitude. Shortly after this, the current suddenly increases and the RMF amplitude decrease simultaneously. Then, as the RMF amplitude approaches zero, the FRC begins to accelerate downstream, eventually leaving the cone after 20-30 μs (the location

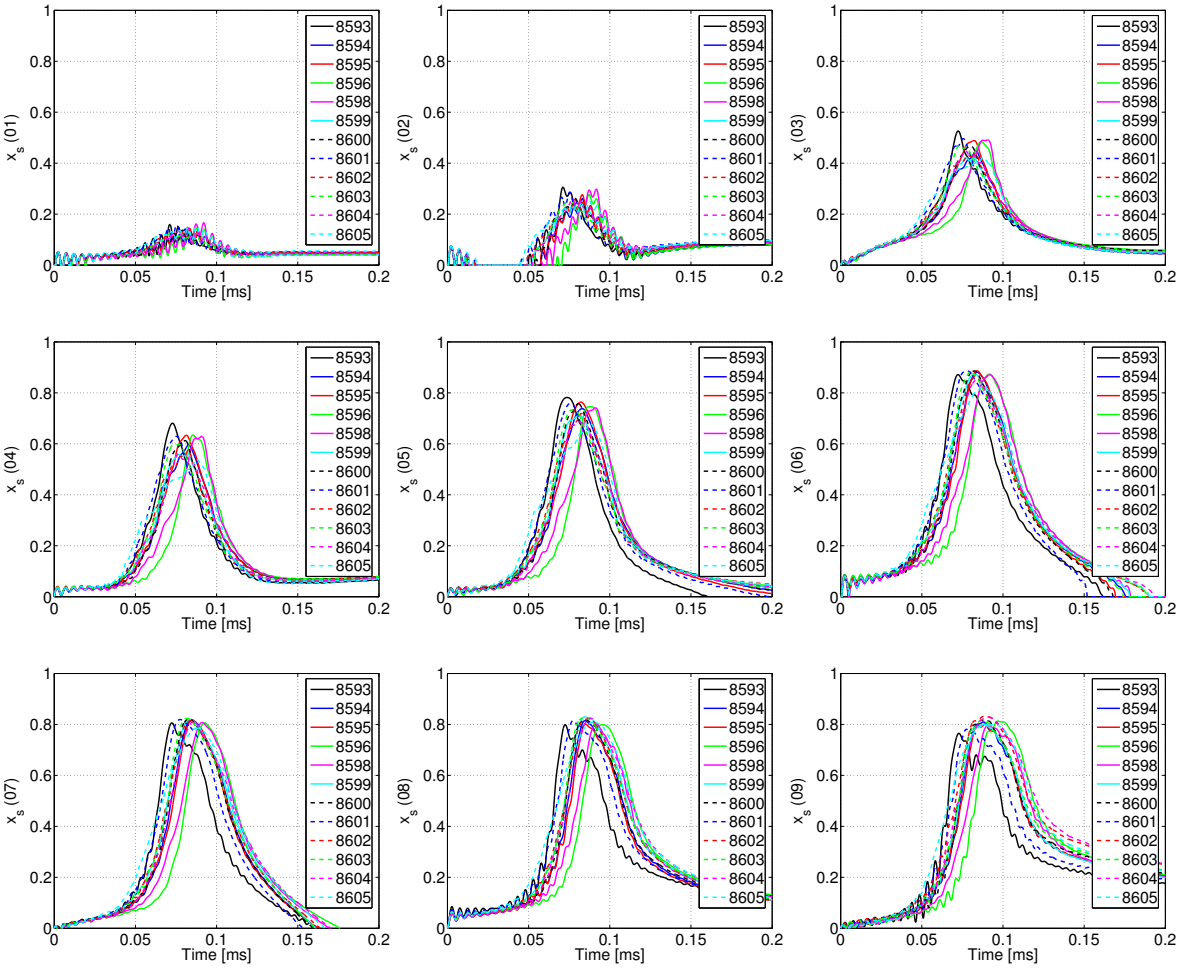

Figure 3.27: Xs at various axial locations for several standard shots (measured with the external B-probes).

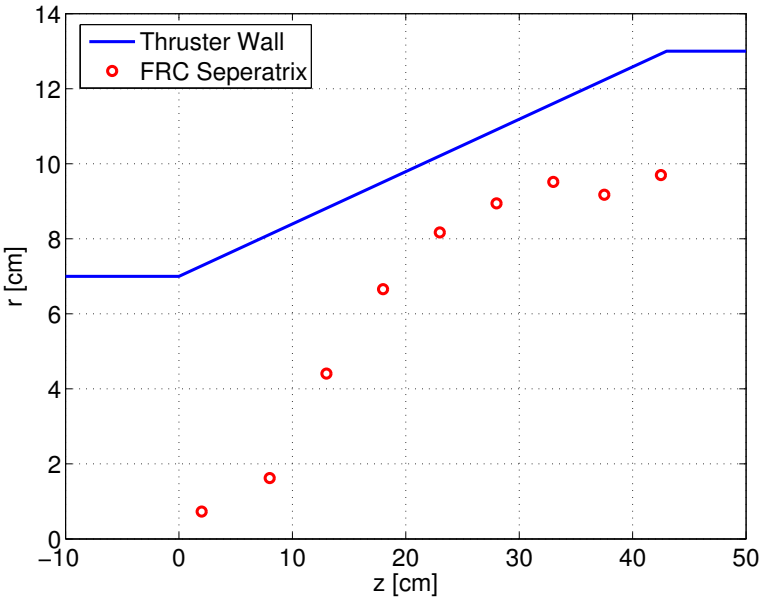

Figure 3.28: Shape of the FRC separatrix prior to ejection.

and size of the FRC is determined non-perterbatively using the array of external B-probes mounted on the exterior of the cone as described in Section 2.6.5).

One may also notice that the FRC forms mainly in a region of relatively low axial bias field (see Figures 3.28 and 3.29). This is due to the fact that the high level of bias in the small end of the cone imparts a significant axial force on any current driven in that vicinity. The current is forced downstream until it merges with the other current that is driven in the lower bias field region, which is where the majority of the current assembles. As downstream end of the FRC begins to leave the cone, the stretching of the transverse field threading the plasma (due to the RMF) imparts an upstream axial force that opposes the downstream force produced by the interaction of the current and the compressed radial bias field. These contraction forces add to the pre-existing tendency for the FRC to contract

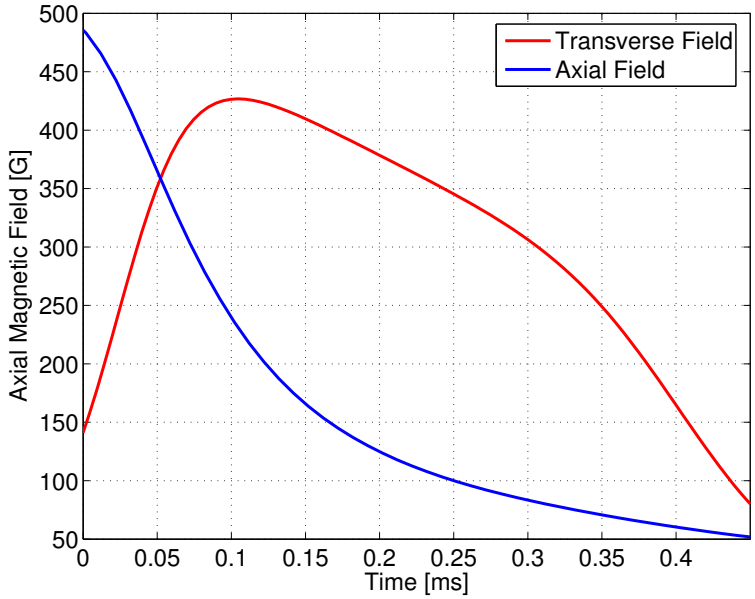

Figure 3.29: Magnitude of the RMF and Bias fields along the axis of the thruster.

axially due to the self generated magnetic fields, all of which is balanced by the gas pressure within the FRC. As the current increases, the axial force arising from magnetic pressure near the wall of the cone increases, reaching a maximum pressure of 487 Pa at a position roughly $\frac{2}{3}$ of the way down the cone.

The internal B-probe mounted roughly halfway along the cone, is an interesting diagnostic with which to observe the formation process. This probe can be oriented longitudinally or transverse to the axis of the experiment in order to observe the axial field reversal or the transverse RMF fields respectively. The axial magnetic profile of the FRC within the cone obtained using this probe is displayed in Figure 3.30. One can see that almost all the change in axial field (and hence current) is located more than halfway to the wall in radius. The inner portion of the profile is relatively flat, and the magnitude of the reversed field is roughly equal to the

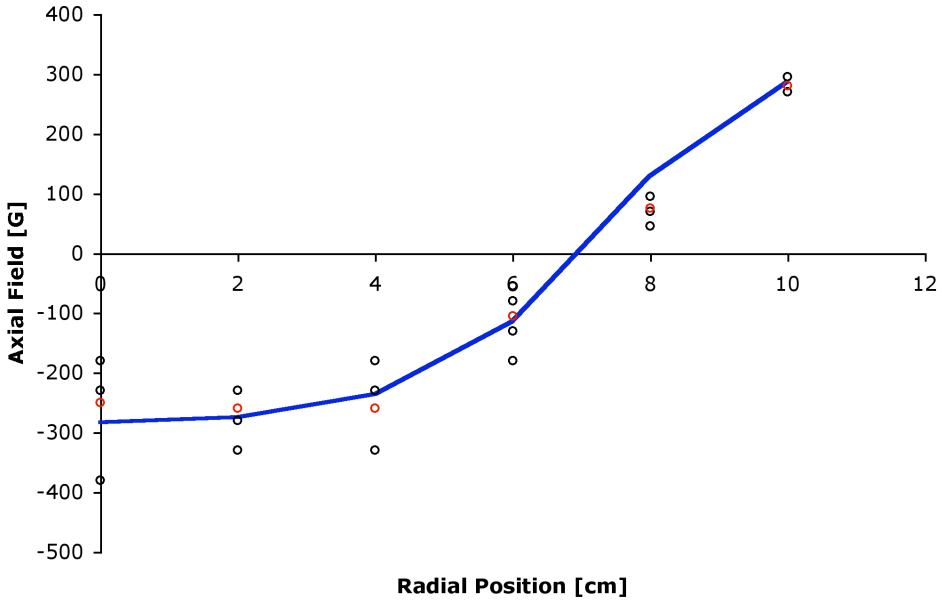

Figure 3.30: Internal B-probe oriented to measure the axial field within the thruster.

external field. This indicates that there is a relatively large amount of magnetic flux linking the FRC, with the current driven fairly uniformly throughout the region of field swing.

Since the x_s of the FRC is known one can calculate the value of R, and thus plot a rigid rotor FRC profile (see Section 1.3) atop the data recorded by the internal B-probe (see Figure 3.30). This allows one to fit for the rigid rotor profile factor K_{RR} and determine an estimate for the density profile. Figure 3.31 shows the density profile for the K_{RR} determined from Figure 3.30. In this case, the rigid rotor parameter is $K_{RR} = 1.4$, and the line density is $N' = 0.02 n_{e_{max}}$ (note: $N' = \int_{r=0}^{r_{wall}} n(r) r \mathrm{d}r\mathrm{d}\theta$). This, along with knowledge of the length of the FRC, the magnetic pressure (from external B-probe data), and the total plasma mass (from

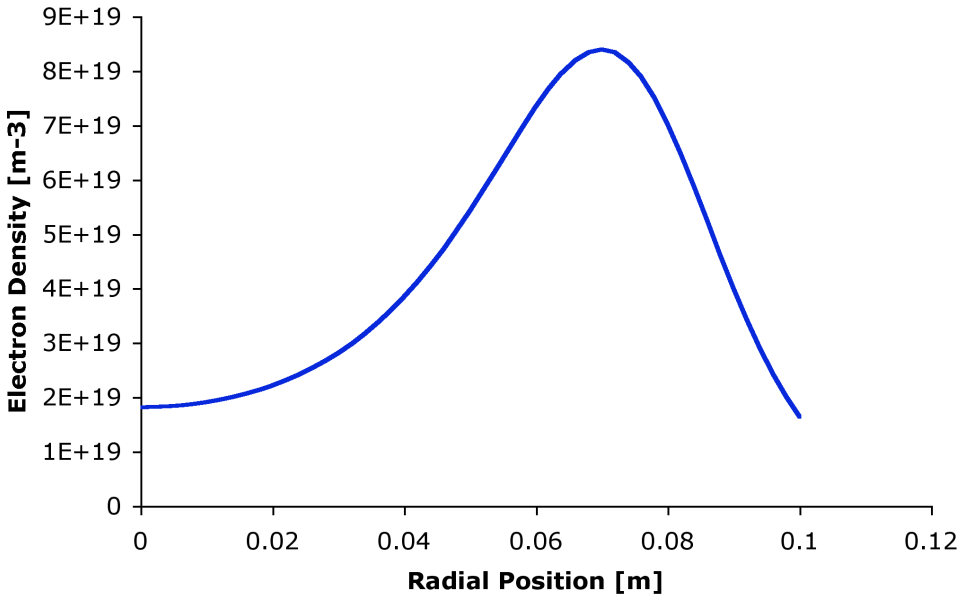

Figure 3.31: Density profile within the thruster.

velocity and impulse data), can allow one to determine the maximum density and the total temperature. Alternatively, the total line density can be computed using the axial magnetic field swing from the axis of the thruster to the wall ($\Delta B = \mu_o I_\theta$, where $I_\theta = \int_0^{r_{wall}} j_\theta dr$, and $j_\theta = e\omega n_e r$). These approaches produce roughly equivalent results.

In the average standard shot, the total number of ions has been found to be $N = 6.71 \times 10^{17}$ (see Section 3.8). From the external B-probe data, the length of the FRC while in the cone is estimated to be $l_{FRC} = 0.4$ m, the line density was $N' = 1.68 \times 10^{18}$ m^{-1}, and the maximum density $n_{e_{max}} = 8.39 \times 10^{19}$ m^{-3}. From the measured external magnetic field, the total temperature is computed to be $T_{total} = T_e + T_i = 36.2$ eV. This puts the combined thermal and magnetic energy of the FRC within the cone to be $E_{th+B} = \frac{5}{2}NkT = 9.74$ J (see Section 1.5).

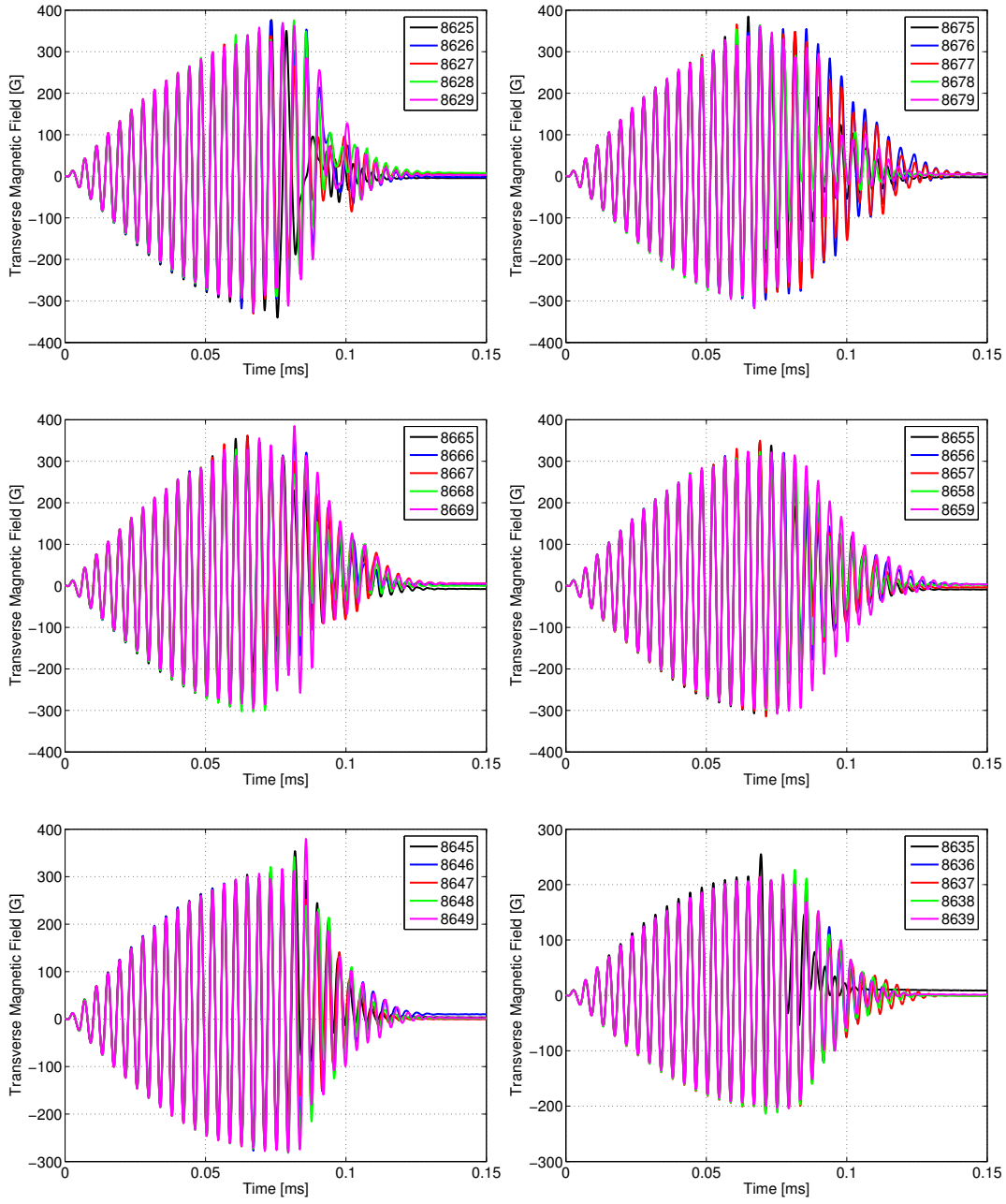

Figure 3.32: Internal B-probe oriented to measure the transverse (RMF) field during formation.

Using the temperature and density from above and the RMF parameters of $\langle B_\omega \rangle = 350$ G and $\omega = 242$ kHz, the non-dimensional numbers γ and λ may be computed (see Section 1.4). For current drive to take place and the RMF fields to penetrate the plasma, the condition $\gamma \geq \lambda$ must be satisfied. Within the cone during the standard shot, $\gamma = 77$ and $\lambda = 7.9$, with the ratio of the two $\frac{\gamma}{\lambda} = 9.76$, well within the range for fully penetrated RMF fields. In addition to measuring the axial fields, the internal B-probe can be utilized to measure the transverse RMF magnetic field within the FRC by simply rotating the probe. One can clearly see in Figure 3.32 the (almost) fully penetrated RMF field during the time of FRC formation.

3.7.2 Ejected Plasmoid

Two types of internal probes were used to study the ejected plasmoid: Langmuir/Mach probes, and magnetic pickup probes. The details of the probes' construction and operation are described in Sections 2.6.4 and 2.6.5. The probes are positioned at axial locations of +54 cm, +94 cm, and +132 cm (indicated by positions 3, 1, and 2 respectively, see Section 2.6). At positions 1 and 2, there are two ports installed in the drift section, permitting the use of a Langmuir probe and an internal B-probe simultaneously. There is only one port installed at position 3, which contained a Langmuir probe for the majority of the referenced testing, though some internal B-probe measurements were taken at this position prior to the construction of the Langmuir probe under standard shot conditions (see Figure 3.36b).

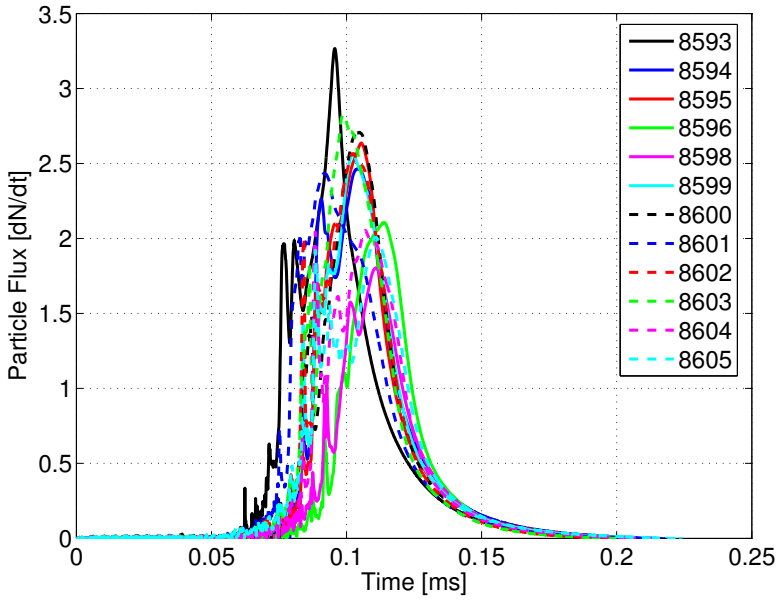

Figure 3.33: Langmuir probe directly outside the exit of the cone (position 3).

One can see in the Langmuir probe traces (Figures 3.33, 3.34a, and 3.35a) that the plasmoid is expands axially as it translates along the drift chamber. Since different parts of the pasmoid are moving at different velocities, a center-of-mass velocity must be obtained to determine the specific impulse of the thruster. The Langmuir probe signal is approximately proportional to the particle flux intercepted by the probe tip (see Section 2.6.4), therefore, the center-of-mass velocity of the plasma can be determined by computing the time of flight of the centroid of the Langmuir signal between probes 1 and 2.

When the center-of-mass velocity is computed from position 3 to 1 and from 1 to 2, the speed is seen to increase as the plasma translates downstream by roughly 20%. This is expected as the plasmoid is still within a region of diverging magnetic field between probes 3 and 1. One may also notice that the majority of the mass

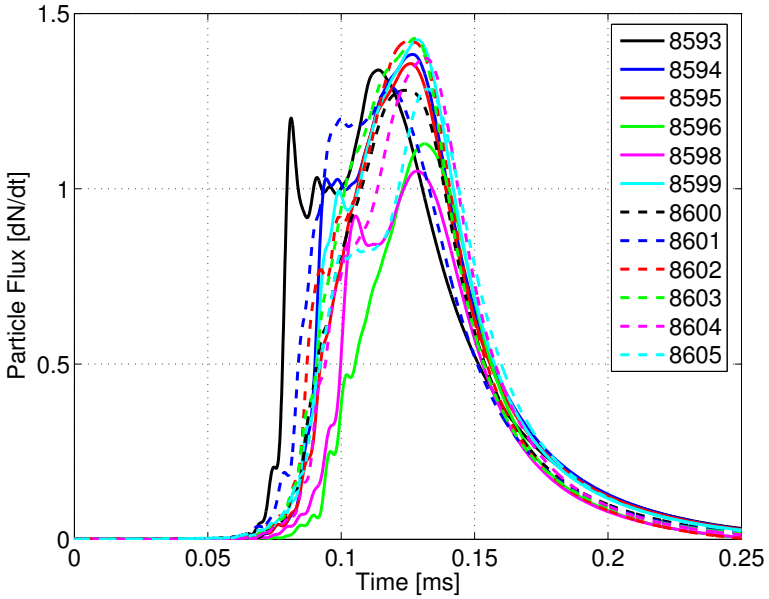

(a) Langmuir probe.

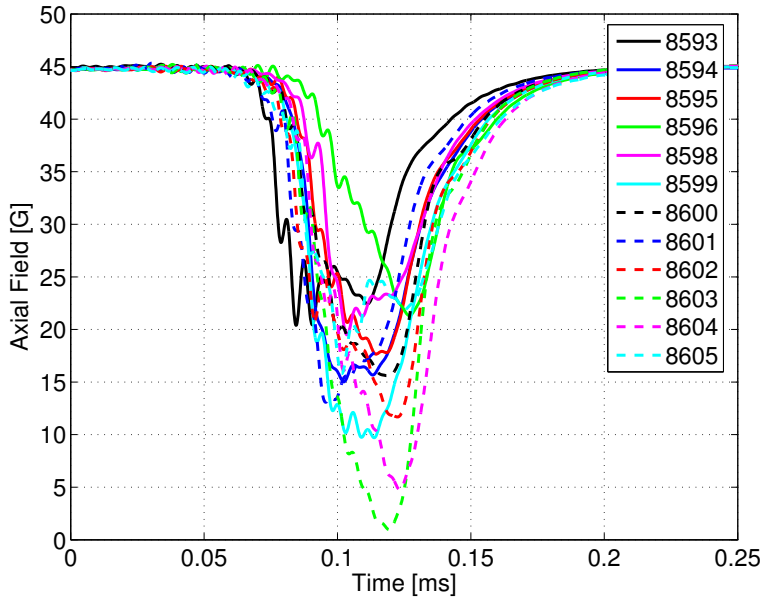

(b) Internal B-probe.

Figure 3.34: Internal probe traces at position 1.

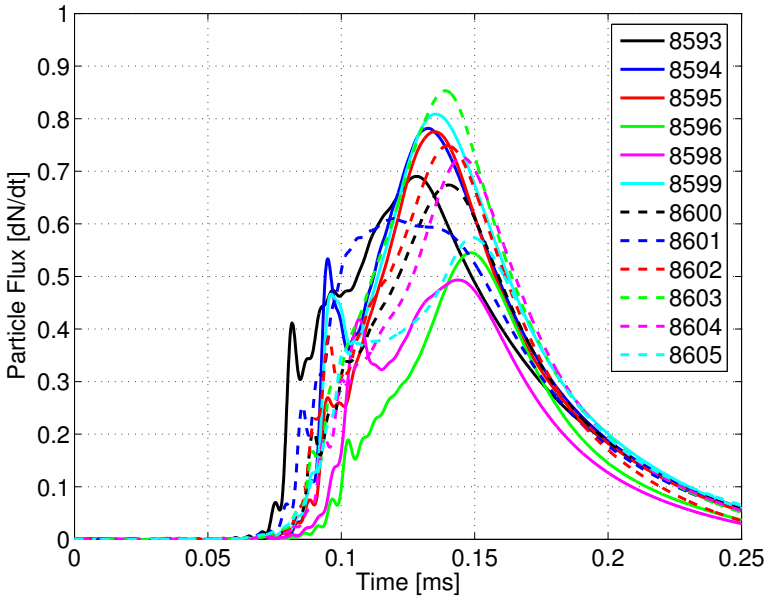

(a) Langmuir probe.

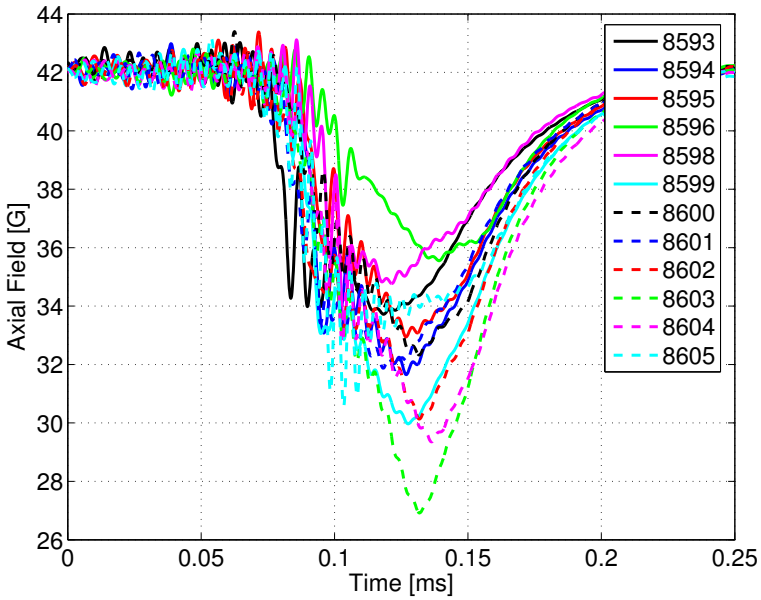

(b) Internal B-probe.

Figure 3.35: Internal probe traces at position 2.

contained within the plasmoid is located near the back of the magnetic structure. This indicates that the plasma is undergoing acceleration, since if the equilibrium were inertial, the plasma would distribute itself throughout about the center of the magnetic configuration.

In addition, it can be seen that there is a small lump of plasma in the front of the main magnetic structure. This has been observed throughout the testing process with two possible explanations of this phenomena having been formulated. The first is that, as observed in the FIG data (see Section 3.3), there is some amount of neutral gas in the drift chamber just outside of the thruster through which the FRC must translate. In doing so, the neutral gas is ionized and pushed along by the magnetic field of the FRC, resulting in a snowplow-like effect. The second theory is that particles which have been lost from confinement across the separatrix migrate to the ends of the FRC (since it is easier for them to move along the magnetic field lines than across them) and form two axial jets, one on either side of the plasmoid. In this way, particles are ejected either upstream or downstream away from the FRC along the axis of the experiment. This leading edge plasma phenomenon is explored further in Section 3.9.

It can be seen in Figure 3.36 that the density and magnetic profiles show a central region with fairly constant values for a small radial span, surrounded by a region of sudden radial change, which is itself surrounded by another fairly constant region. This profile is very similar to the one observed in the cone using the internal B-probe. This indicates that, just outside the cone, the FRC has similar properties as it did when it was still within the cone. Most importantly, that the plasma is

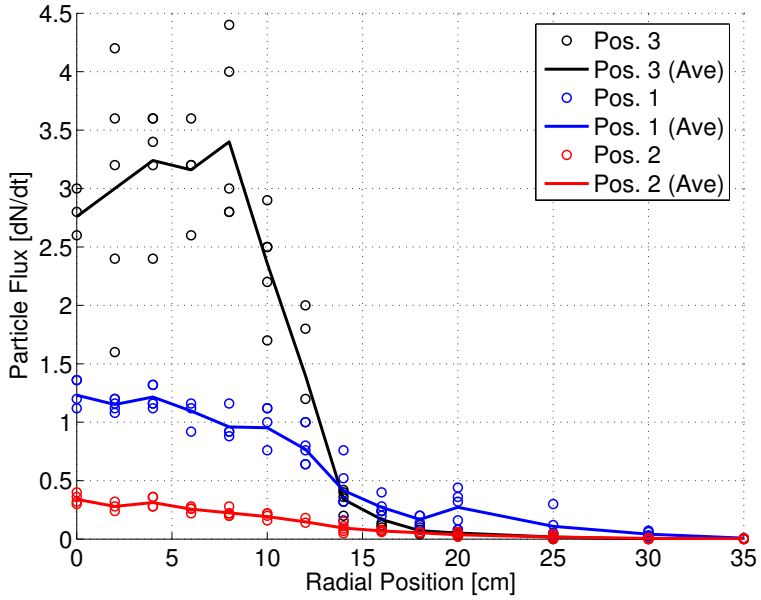

(a) Langmuir profiles.

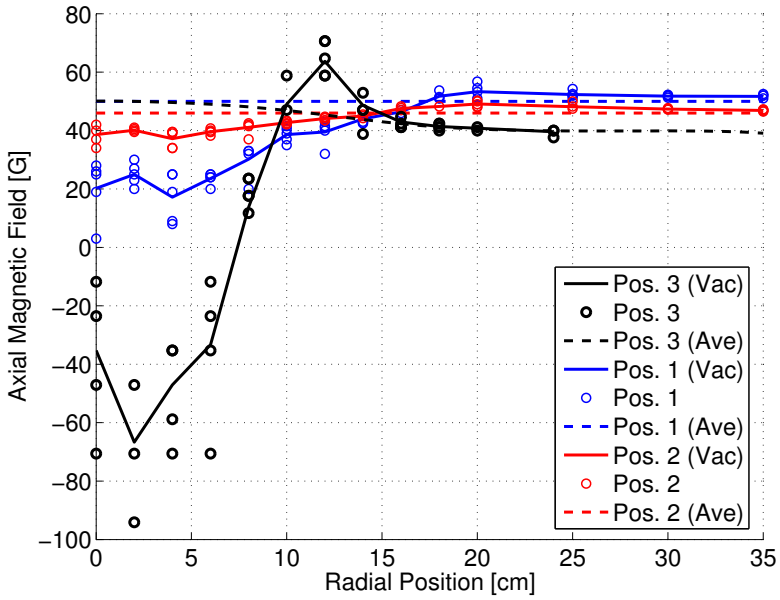

(b) Magnetic profiles.

Figure 3.36: Langmuir and axial magnetic field profiles at the three downstream locations.

still strongly confined within the magnetic structure after it has left the cone.

One also notices in the magnetic profile at position 3, that the external field overshoots the value that it takes the wall. This is due to the fact that the FRC is not yet in radial equilibrium. Consider the magnetic field of a current ring in empty space; as one move away from the ring the field will drop off like r^{-3}. The degree of overshoot indicates the length of the FRC in that a longer cylindrical current produces less overshoot than a shorter cylinder. By matching the profile, it is possible to reconstruct an approximation of the current in the FRC and obtain a length estimate. Estimating the length of the current ring using this method yields a length of roughly 10 cm at position 3. This is somewhat inaccurate due to the fact that the axial and radial current profiles are not modeled with very high fidelity. However, it provides some indication that the FRC contracts axially as it leaves the cone (while the central field is still reversed) as predicted by the conservation of energy (see Section 1.5), before expanding axially in the drift chamber (at which point the plasmoid is no longer an FRC, see below).

As the plasmoid moves downstream the profile changes; the plasma becomes less confined and it expands both outward radially and inward to fill the central hole (Figure 3.36b). In addition, the current has decayed and the magnetic field is no longer reversed on axis. The FRC has become a blob of diamagnetic plasma, although some semblance of its former profile can still be seen. By the time the plasma reaches the probes at position 2, the profile no longer resembles that of an FRC. The density is peaked on axis and plasma has spread out almost to the wall. The diamagnetic current has decayed almost completely; there is only enough

diamagnetic current to reduce the field on axis by ~ 10 G.

The total time elapsed from the time that the RMF current drive ceased to the time of observation at position 2 was roughly 50 μs. Using the observed dimensions of the FRC and assuming an overall resistance similar to that which was switched into the tank circuit in the SPICE model of Section 2.6.6 ($R_p \approx 250$ mΩ), gives a decay timescale of $\tau_{L/R} \approx 15$ μs, which matches the observations.

The SPICE analysis also allows an estimate of the total energy into the plasma to be made. The actual amount of energy into the plasma varies depending on the amount of time that elapses between the RMF breakdown of the neutral gas, and the time at which the RF supply stops adding energy to the system (as discussed in Section 3.4). For the standard shot, the times of breakdown associated with most of the shots resulted in a calculated 46 J of energy into the plasma. For the few shots with a late time of breakdown (after the RF supply had stopped), the energy into the plasma was calculated to be 36 J. There was enough consistency in the amount of energy absorbed that it would be appropriate to use 46 J as the average amount of energy absorbed for the standard shot and also most of the shots in the subsequent sections.

Shortly prior to the in-depth testing of the standard shot and variations thereof, the Langmuir bias voltage was swept in order to make sure that they were still well within the ion-saturation regime assumed in the analysis of the data (see Section 2.6.4). The maximum recorded signal as a function of bias voltage (plotted in Figure 3.37) confirmed that the probes were in ion-saturation, and in addition, the fitting of the data indicated that the electron temperature of the plume was 7 eV.

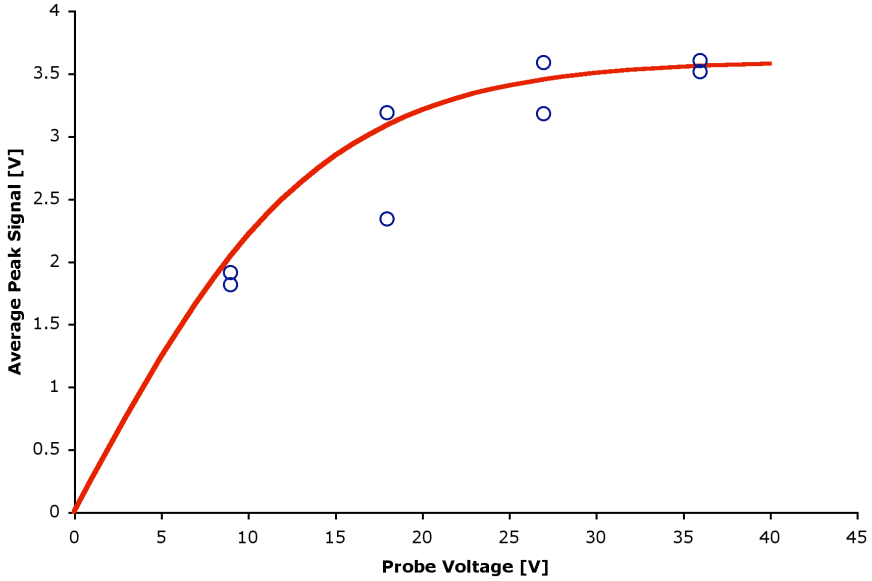

Figure 3.37: Maximum Langmuir signal as a function of probe bias voltage (fit to a 7 eV curve).

The combination of the center-of-mass velocity and the plasma impulse corrected for the amount of mass missing the pendulum (see Section 3.8) allows one to obtain estimates for the mass of the plasma and the kinetic energy. If one assumes that the electron and ion temperatures are the same, the total thermal and magnetic energy contained in the plume can be computed using the methods of Section 1.4. One can also use the mass to determine the minimum required energy that would have been needed to ionize the plasma in the FRC (also see Section 1.4). The sum of these energies is the total energy of the plasma flow in the drift chamber. The total plasma energy while the FRC is still within the cone can also be computed using the data obtained from the internal cone probe.

These energies, combined with the estimate for the energy absorbed by the

Impulse	274 μN-s	**Ionization Energy**	2.09 J
Corrected Impulse	338 μN-s	**Cone Th.+Mag. Energy**	9.74 J
Plasmoid Velocity	2.19 cm/μs	**Plume Th.+Mag. Energy**	3.76 J
Computed Mass	15.6 μg	**Plume Kinetic Energy**	3.69 J
Max Density	8.39×10^{19} m^{-3}	**Energy Input**	46 J
Max Temp. ($T_e + T_i$)	36.2 eV	**Cone Total Energy**	11.8 J
Plume Temp. ($T_e + T_i$)	14 eV	**Plume Total Energy**	9.54 J

Table 3.2: The standard shot.

plasma (using the SPICE model) can provide insight into the relative efficiencies of the processes taking place within ELF. One can see in Table 3.2 that much more energy is lost in the formation process than in the acceleration process. This is most likely due to inefficiencies in the ionization process (radiative losses) and wall losses which may be improvable. It must also be noted that any energy in the ejected plasmoid other than kinetic energy is a frozen flow loss, which is not useful for the purposes of producing thrust. One notices that in after the ionization energy is paid, half of the energy in the plume is in the form of thermal energy and half is in the form of kinetic energy. This indicates that the efficiency of the expansion process ($\sim$ 50 %) could also be significantly improved. The study of possibly performance enhancing modifications is the subject of future work, discussed in Section 4.4.

3.8 Drift Bias Study

As stated in Section 2.2, the main purpose of the drift bias is to prevent the plasmoid from expanding into the chamber walls once it has left the thruster and

is drifting in the main chamber. In a space environment there would, of course, be no drift bias present, so the effect of its presence must be determined if one is to understand the operation of the thruster.

To accomplish this, the thruster was tested at varying levels of drift bias intensity, with radial probe sweeps performed at three selected settings. All other parameters were fixed to the settings they take in the standard shot. Plots of the measured impulse and center of mass velocity can be seen in Figure 3.38. Upon examination of the impulse plot, it can be seen that the measured impulse rises sharply as the level of the drift bias is increased from 0 to 33 gauss (corresponding to 60 V on the capacitor bank) where it reaches a maximum. It then slowly decreases over the remainder of the range of tested field intensity. The velocity plot shows the same sharp rise over the lower range of bias, peaks at the same value, then decreases. This trend continues until the applied field reaches roughly 150 G ($\sim$ 200 V), at which point the velocity becomes erratic from shot to shot with an increase in speed on average. In this high range, the magnitude of the bias field in the chamber is larger than the magnitude within the cone (see Figure 3.39), thus resisting the ejection of the plasmoid and affecting the formation process.

The mass can be inferred from the impulse and center of mass velocity measurements (see Figure 3.40). It is important to note that the measured mass is not constant throughout the bias sweep, and the maximum mass does not occur at the same value of bias field as the maximum impulse or velocity. The origin of these trends is due to the varying degree of expansion of the plasmoid for the various levels of applied bias field. At very low values, the FRC expands to the point at which

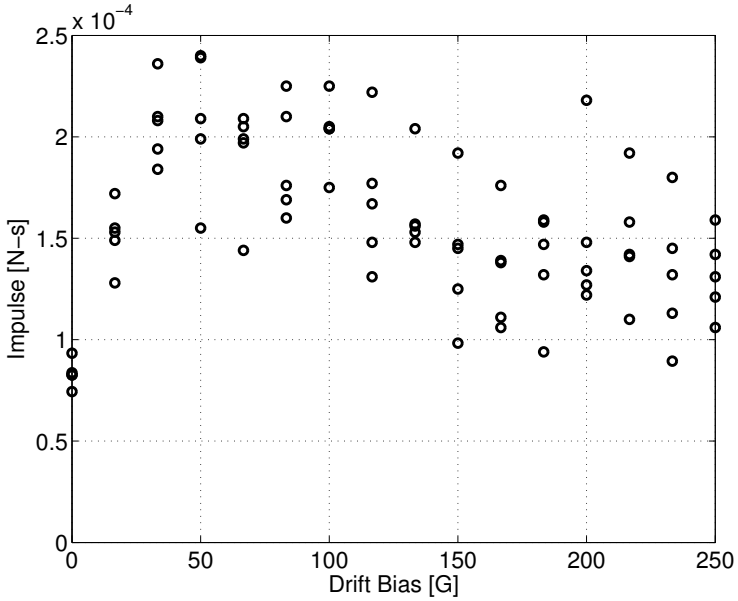

(a) Impulse.

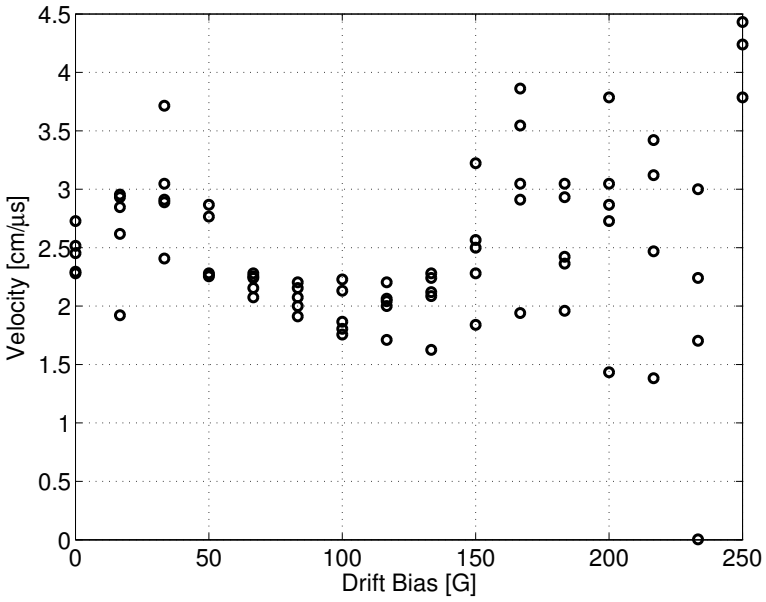

(b) Velocity.

Figure 3.38: Measured impulse and velocity over a sweep of the drift bias.

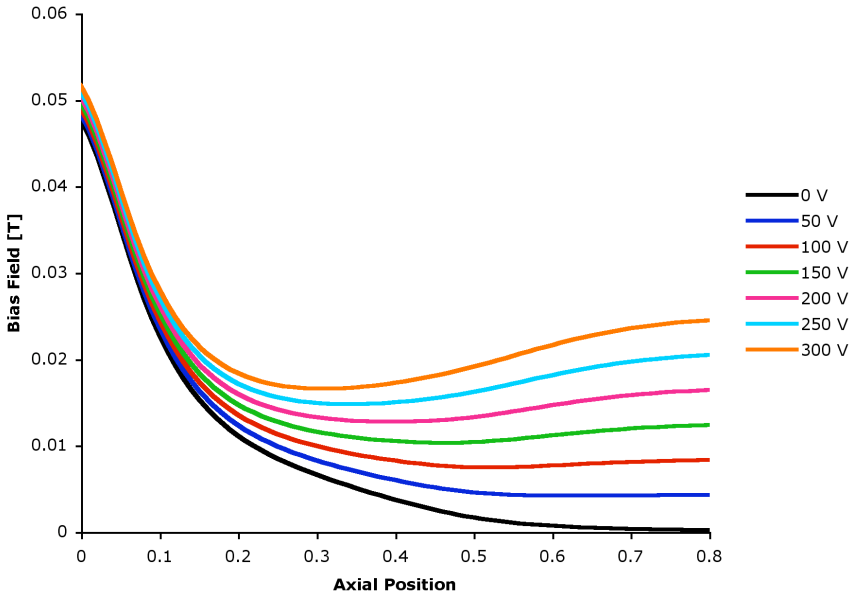

Figure 3.39: Axial bias profile for various drift bias conditions.

it makes contact with the walls of the drift chamber. This creates a drag on the plasma and reduces the final speed with which it strikes the pendulum decreasing the impulse. In addition, the amount of impulse measured by the pendulum is not the total impulse carried by the plasma. Since the face of pendulum (2500 cm^2) is roughly half that the cross sectional area of the drift chamber (5026 cm^2) some of the plasma misses the pendulum, resulting in a measured impulse that is less than the actual value. As the intensity of the bias field is increased, a higher fraction of the plasma impacts the pendulum as less of it spreads to large radii, also there is less drag from the chamber walls. At 33 G the lower interaction with the wall and the reasonably large expansion ratio combine to produce the largest velocity. As the bias is increased further, the reduction in wall drag is offset by the reduction in expansion ratio and the velocity drops. While the fraction of the plasma striking

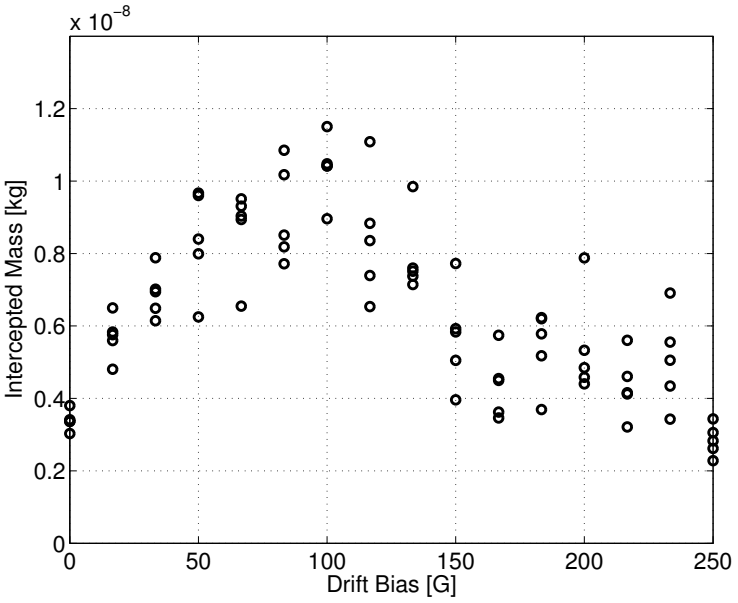

Figure 3.40: Measured mass as a function of drift bias.

the pendulum is still increasing with increasing bias field, the additional mass does not counterbalance the reduction in velocity. Between 50 and 115 G, the mass striking the pendulum is roughly constant, with the maximum occurring at 100 G. Above $\sim$ 130 G, as mentioned above, the bias field becomes strong enough to prevent the plasma from exiting the thruster, and the mass striking the pendulum is further reduced.

In the case of the standard shot, while there is enough bias field present to keep the plasma off the chamber walls, there is not yet enough to force all the mass on to pendulum. Doing so would slow the plasma down and possibly interfere with the proper operation of the thruster. Instead, in order to obtain the plasma impulse, one must take the maximum mass from Figure 3.40 multiplied by the observed velocity. The mass intercepted by the pendulum during the standard shot turns

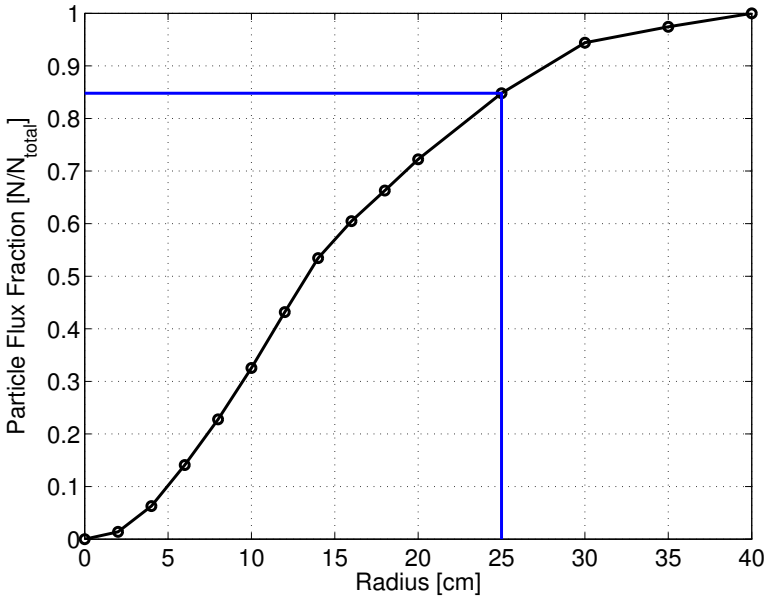

Figure 3.41: Mass flux as a function of pendulum radius as measured by Langmuir probe (blue line shows pendulum radius).

out to be $\frac{2}{3}$ of the total mass (thus one can simply multiply the measured impulse by 1.5 to obtain the corrected impulse). This multiplier is applied to the standard shot and can be used to estimate the true impulse in other tests in which the drift bias is fixed at the standard condition. Although this number will change as the flux within the FRC varies (see Section 1.5), this is nonetheless a reasonable guess as to the amount of missing mass.

In addition, several tests were performed in which the pendulum was placed within several inches of the exit of the cone. The same shot was repeated with the pendulum placed further downstream in the drift chamber. When the pendulum was close to the cone, all of the plasma exhausted by the thruster impacted the pendulum. When the pendulum was moved downstream, it intercepted less total

mass. The final estimate for the total mass exhausted by the thruster was very close to that estimated using the bias-focusing method of above (a correction factor of 1.6 was found).

A radial Langmuir and B-probe sweep was performed for the cases of the drift bias at 15 G, 50 G (standard condition), and 160 G in order to compare to the standard shot sweep shown in Figures 3.42, 3.43, and 3.44. One can easily see that the plasma attains a much larger radius when the bias field is low. Note that the plot of the mass variation with radius must be weighted by an additional factor proportional to r to account for the azimuthal nature of the distribution (a signal measured near the wall indicates more total mass than a signal of the same magnitude near the axis).

An investigation of the amount of mass missing the pendulum using the above method with the Langmuir probe closest to the pendulum indicated that only $\sim$ 15 % of the plasma misses the pendulum (half of the estimate obtained using the other two methods). It is thought that the proximity to the wall and the rapid decay of the plasma (high recombination rate) resulting in a violation of the assumptions used to estimate the local mass flow rate in the Langmuir probe analysis is the cause of the discrepancy. The results of the analysis can be seen in Figure 3.41.

The Langmuir profile taken while the drift bias is very high confirms the assertion that the plasma is restricted to the region near the axis. In addition, less total gas can be seen to escape from the thruster as the magnetic field in the conical section is lower that that in the drift section. As mentioned above, this mirror field

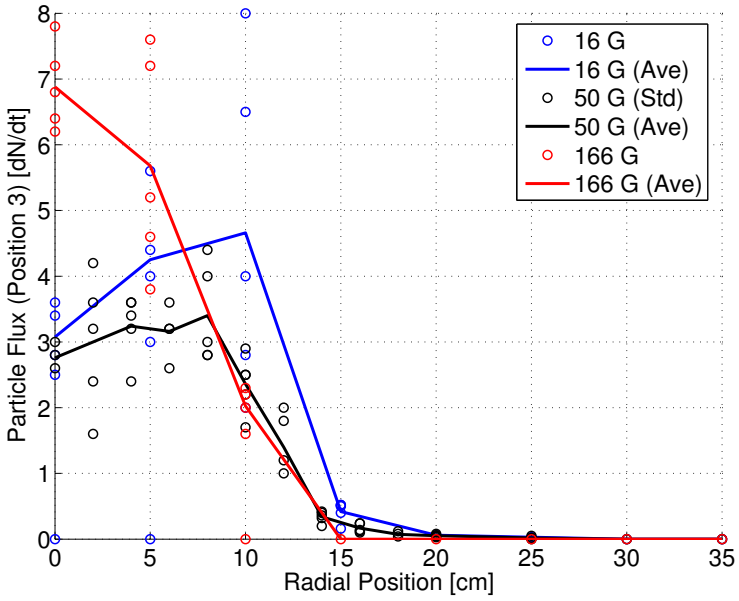

Figure 3.42: Langmuir profiles at position 3 for various drift bias settings.

imparts an upstream axial force to the plasma preventing some of the mass from translating downstream. The effect of the high drift bias may also be seen when in the Langmuir and internal B-probe signals. In contrast to the standard shot, it can be seen that when the drift bias is high, the plasma either spreads uniformly throughout the magnetic structure, or it is peaked in the front, indicating that the plasmoid is undergoing deceleration.

If one examines the differences in the magnetic profiles at the two downstream locations for the low and standard drift bias conditions, and the time it took for the plasma to travel the distance between the two probes, one can compare the relative decay rates of the current in the plasma. This can lend some understanding of how the expansion affects the lifetime of the plasmoid.

In most cases, the lifetime of an FRC is limited by the L/R decay of the current

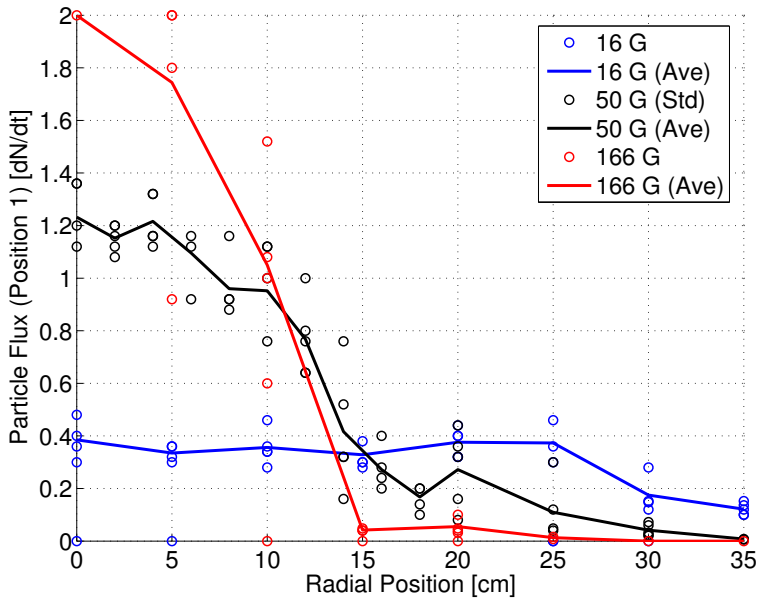

(a) Langmuir profiles.

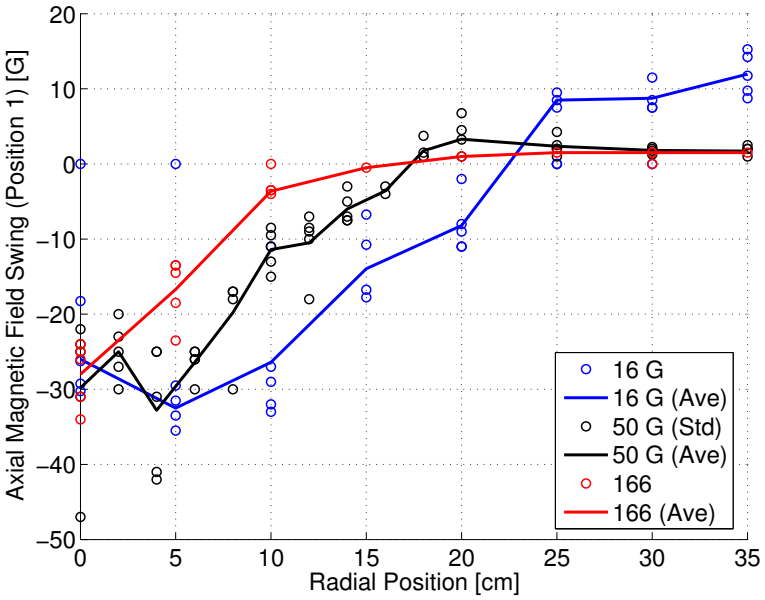

(b) Magnetic profiles.

Figure 3.43: Langmuir and magnetic profiles at position 1 for various drift bias settings.

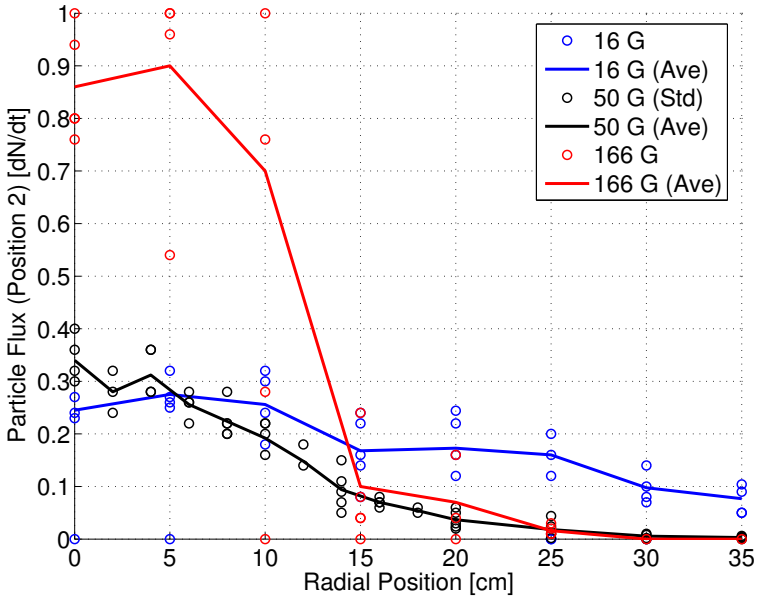

(a) Langmuir profiles.

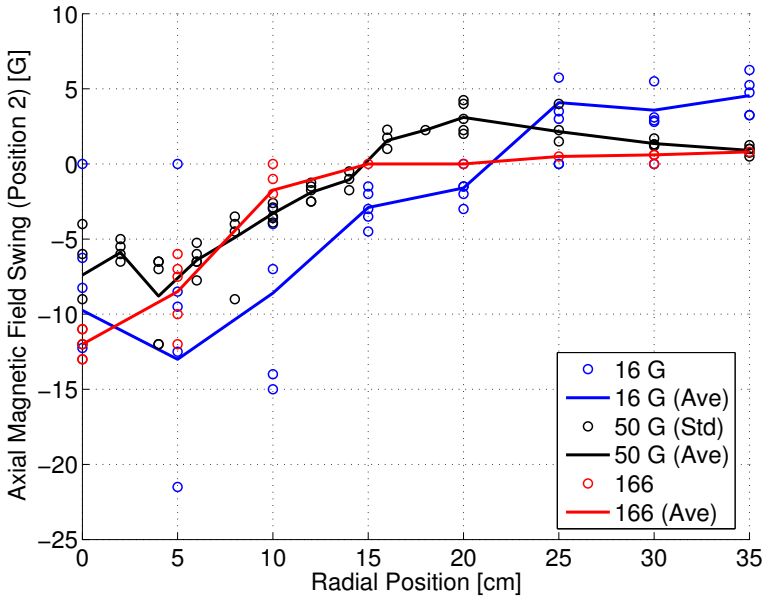

(b) Magnetic profiles.

Figure 3.44: Langmuir and magnetic profiles at position 2 for various drift bias settings.

in the plasma. As an FRC changes in size, the inductance and the resistivity both change, resulting in a change in the flux decay timescale (τ_ϕ). The inductance can be approximated by modeling the FRC as a 1 turn finite-length solenoid, however, the resistivity scaling of an FRC is not known a priori. There are several models which describe possible plasma resistivity scaling: Spitzer (classical), Bohm, Lower-Hybrid Drift (LHD), and Chodura. In an FRC, the LHD model reduces to Bohm since the ion gyroradius is roughly the same as the characteristic density length scale. Assuming that flux and the number of particles is constant, and that the expansion occurs 3 dimensionally (the plasmoid length is proportional to the radius).

$$B = \frac{\phi}{\pi r^2} \propto r^{-2} \tag{3.10}$$

$$n = \frac{N}{\pi r^2 l} \propto r^{-3} \tag{3.11}$$

$$T = \frac{pV}{N} \propto B^2 r^3 \propto r^{-1} \tag{3.12}$$

The proportionalities can be substituted into the formulations for the resistivities.

$$\text{Spitzer: } \eta_\text{S} \propto T^{-3/2} \propto r^{3/2} \tag{3.13}$$

$$\text{Bohm: } \eta_\text{B} \propto \frac{B}{n} \propto r \tag{3.14}$$

$$\text{LHD: } \eta_\text{LHD} \propto \eta_\text{B} \left(\frac{r_\text{gi}}{l_d}\right)^2 \propto r \tag{3.15}$$

$$\text{Chodura: } \eta_\text{C} \propto \frac{\omega_\text{pi}}{n} \left[1 - \exp\left(-n^{-1} T^{1/2}\right)\right] \tag{3.16}$$

$$\eta_\text{C} \propto r^{3/2} \left[1 - \exp\left(-r^{7/2}\right)\right] \tag{3.17}$$

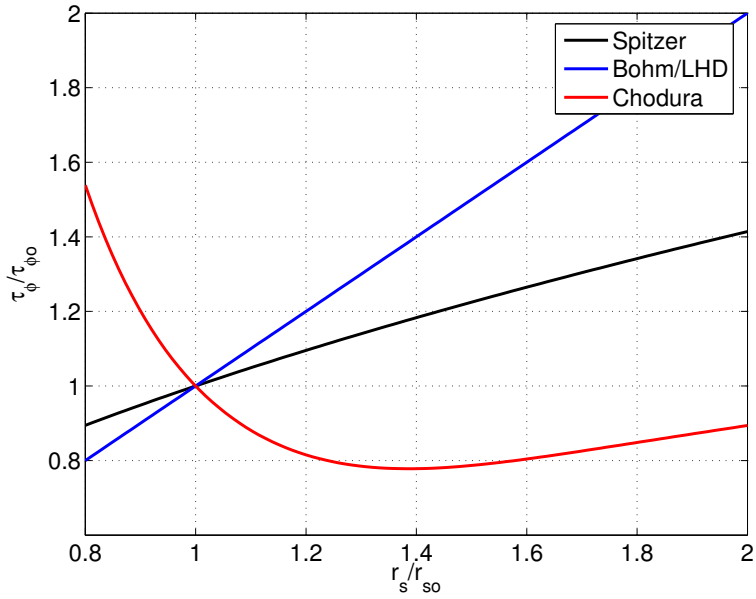

Figure 3.45: Flux lifetime as a function of expansion ratio for various resistivity scalings.

These resistivities are then used in the expression for FRC flux lifetime.

$$\tau_\phi = \frac{L}{R} \approx \frac{\pi r^2 10^{-6}/l}{\eta l/\pi r^2} \propto \frac{r^2}{\eta} \tag{3.18}$$

The resulting fractional change in flux lifetime vs. expansion ratio is plotted in Figure 3.45 (where τ_ϕ is the flux lifetime when the separatrix is of a radius r_s, and $\tau_{\phi o}$ is the flux lifetime when the separatrix is of a radius r_{so}, the initial radius). This analysis indicates that for all scalings except Chodura, for the expansion ratios observed in ELF, the flux lifetime should increase as the FRC expands. This is observed in the low and standard drift bias profiles with the scaling most resembling Bohm (lifetime ratio of ~ 1.4 at an expansion ratio of ~ 1.4, with an estimated

error of ~ 30 %, so Spitzer is also possible). The high drift bias profile, however, does not start at similar enough conditions (flux, number of particles, etc) to be comparable against the other two cases.

3.9 Puff Timing Study

After determining the necessary level of drift bias to maintain the intended operation of the thruster while properly measuring the plume, the actual thruster parameters were varied from the standard conditions and the effects of this change were observed. Experience has shown that the operation of ELF is very sensitive to the initial distribution of neutral gas prior to the discharge. Since the driver voltage and puff duration had already been optimized for the shortest, most concentrated pulse of gas attainable with the current hardware (see Section 3.3), the puff start time and the gas line pressure were then varied.

A series of tests were performed in which the puff start time was swept backwards in time over a range of roughly 2 ms (twice the time required for the neutral gas to begin emerging from the large end of the cone). As in earlier sections, multiple shots were taken at each setting. The series was repeated using several gas line pressures, which has the effect of amplifying the density while keeping the shape of the density trace the same in time (see Section 3.3).

Examining the standard case of 20 psig in Figure 3.46a, one can see that there is no impulse produce when the time between the start of the puff and the start of the RMF is short (~ 500 μs). This is because there there is insufficient time

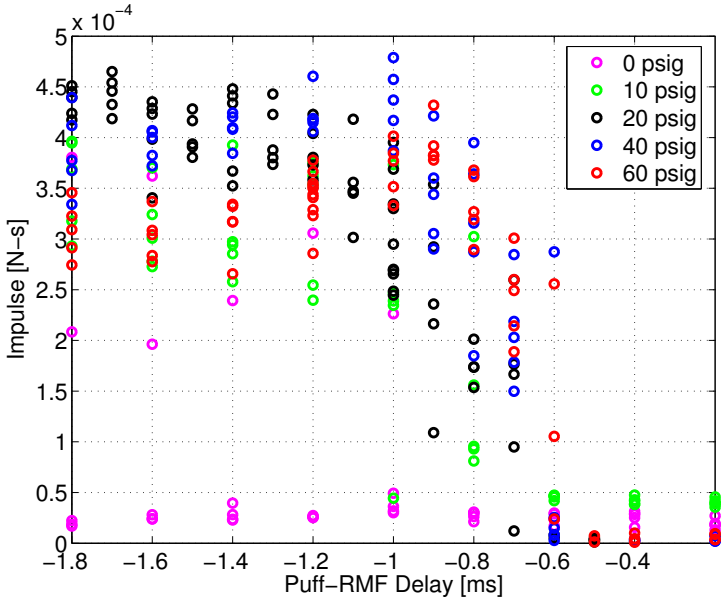

(a) Impulse.

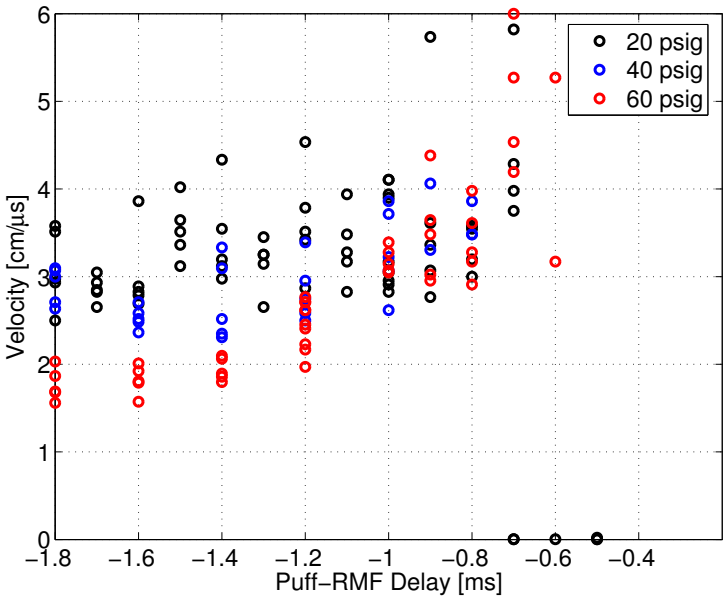

(b) Velocity.

Figure 3.46: Impulse and velocity for various puff and pressure operating conditions.

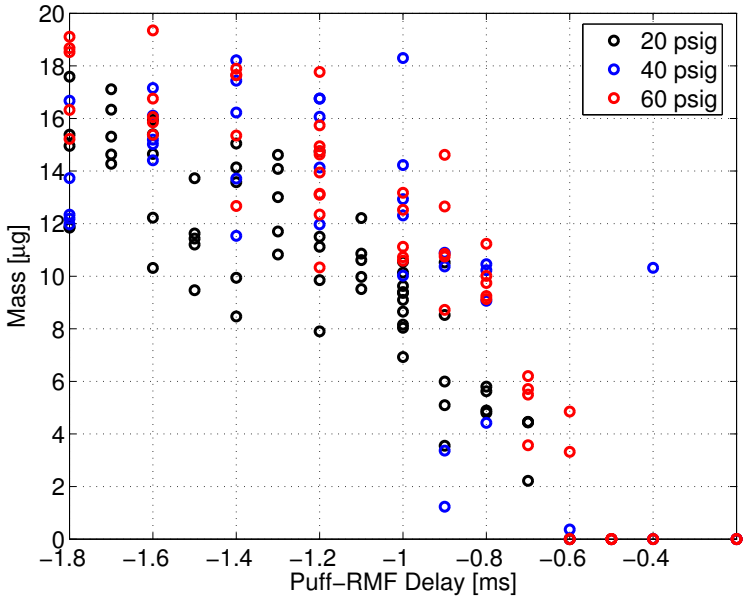

Figure 3.47: Mass for various puff and pressure conditions.

for enough neutral gas to flow into the cone to raise the density high enough for the RMF to be capable of initiating a cascading ionization process within the gas. After 500 μs, the RMF becomes capable of ionizing the neutral gas, however there is still relatively little gas within the cone. As a result of the low gas density, the produced plasmoid is lighter and faster, but contains less impulse than the standard shot (-1 ms). The velocity and mass (computed) can be seen plotted in Figures 3.46b and 3.47.

As more time is allowed to elapse between the start of the puff and of the RMF, one can see that the increase in impulse with delay time begins to slow near -1 ms and is almost level by -1.5 ms. The mass however, continues to increase throughout this range with the velocity decreasing accordingly.

If one plots the kinetic energy of the ejected plasmoid (along with the ioniza-

tion energy to account for differences in mass), one can see that the total energy increases until roughly -1.2 ms, at which point it levels off for the duration of the sweep. This plateau represents a constant level of physical efficiency where the operation of the thruster with respect to specific impulse can be varied. This does not, however, represent thruster efficiency (which peaks at -1.5 ms, in which ionization energy counts as a frozen flow loss). The thruster efficiency is explored in greater detail in Chapter 4.

When the puff start time is swept with increased line pressure, the result is a compression of the above trends into a shorter range of delay times, with the "knee" of the impulse vs. puff timing curve taking place at -1 ms at 40 psig and -800 μs at 60 psig. In addition, one can observe that the impulse begins to decrease as the delay between the start times of the puff and the RMF grows large enough.

This occurrence has been observed to a lesser extent a line pressure of 20 psig if the range of the sweep is extended, however, the reduction in impulse is less severe than it is in the case of higher line pressures. The reduced impulse continues at a consistent level for the next several milliseconds of delay. This corresponds to a peak amount of neutral gas within the cone, as the rates outward and inward gas flow combine to produce a fairly constant level of neutral particles within the cone for several milliseconds. Eventually the impulse drops off as the particle supply from the gas puff runs out.

When the sweep is performed with lower line pressures (0 and 10 psig), the impulse rises over a larger range of puff start times. However, there is a limit that is reached at roughly -1.5 ms where any additional gas that enters through the

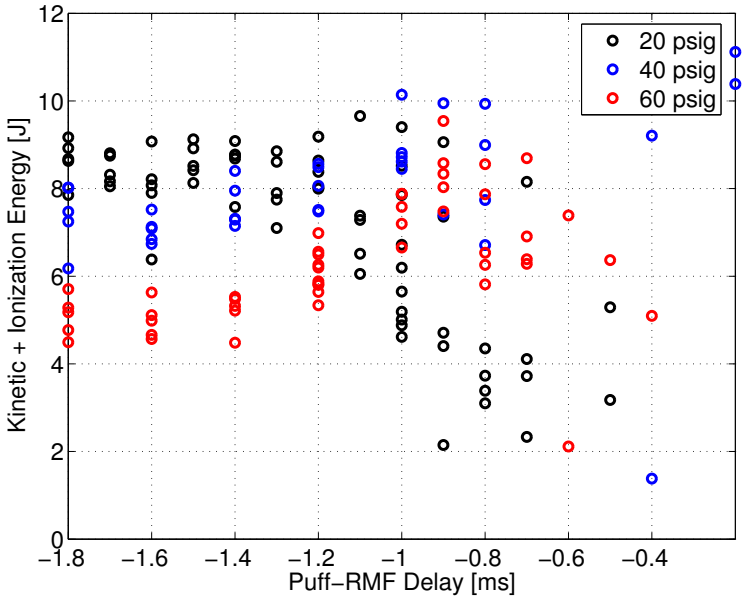

Figure 3.48: Kinetic + ionization energy for various puff and pressure conditions.

small end of the cone is offset by the gas streaming out of the large end. This translates into a maximum number of particles attainable within the cone, which for lower line pressures, is insufficient to produce an efficient discharge.

One notices that, in all cases, the mass of the plasmoid continues to increase after the point at which gas begins to stream out of the large end of the cone. This can be due to the sweeping up of mass as the plasma exits the cone, and it can also be due to the fact that the mass flow rate (as observed by the FIG) is continually increasing for several milliseconds after the puff is initiated.

The sweeps conducted at higher line pressures, as with the 20 psig case, result in the velocity decreasing as the mass increases with the delay time. However at the higher line pressures this trend is more pronounced than it is at 20 psig. One can also see a clear range where the total energy within the plume is maximized, taking

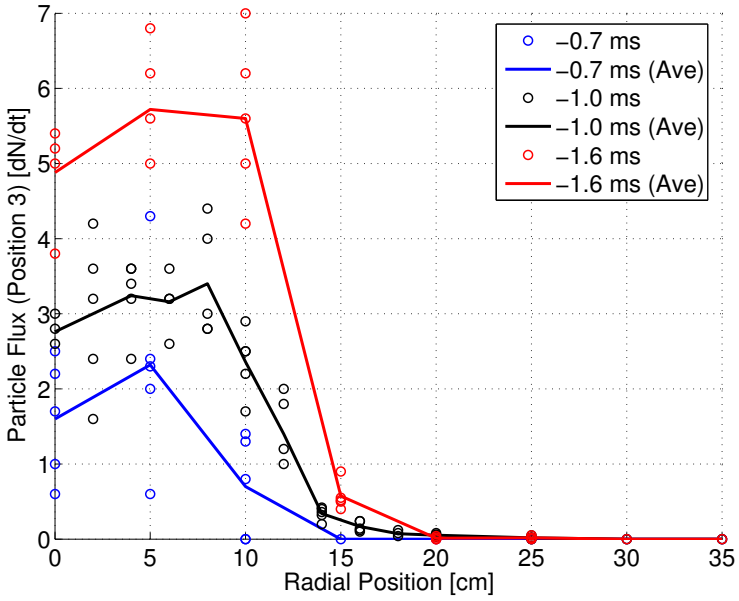

Figure 3.49: Langmuir profiles for various puff timings at 20 psig (Position 3).

place at roughly the same times that the impulse is maximized. This suggests that there is a mass of $\sim$ 12 μg at which this particular formation process is at an optimum. This number is, however, subject to change with changing operational parameters.

It makes sense that there would be an optimum near this point. There needs to be at least enough charge carriers present to reverse the axial bias field and form a closed configuration, however, the radiative losses go up with the square of the density, and as the mass of the plasmoid goes up there is less energy with which to drive current after the ionization penalty is paid, which is not insignificant, especially at lower exhaust velocities.

Three cases chosen on which to perform a radial Langmuir and internal B-probe sweep: -0.7 ms, -1.0 ms, and -1.6 ms (shown in Figures 3.49, 3.50, and 3.51). If

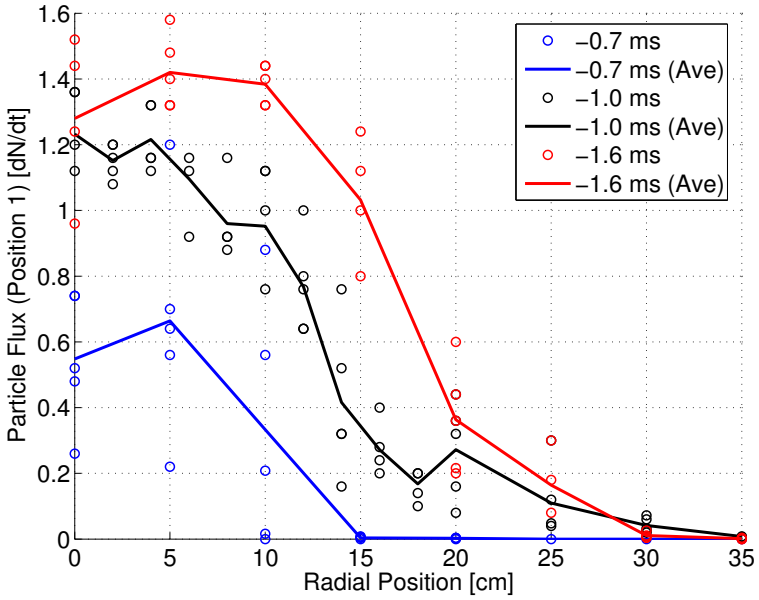

(a) Langmuir profiles.

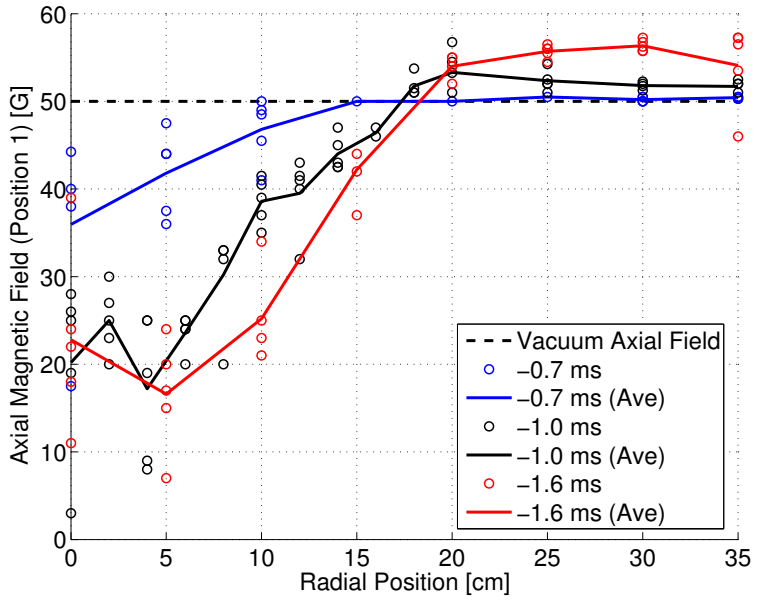

(b) Magnetic profiles.

Figure 3.50: Langmuir and magnetic profiles for various puff timings at 20 psig (Position 1).

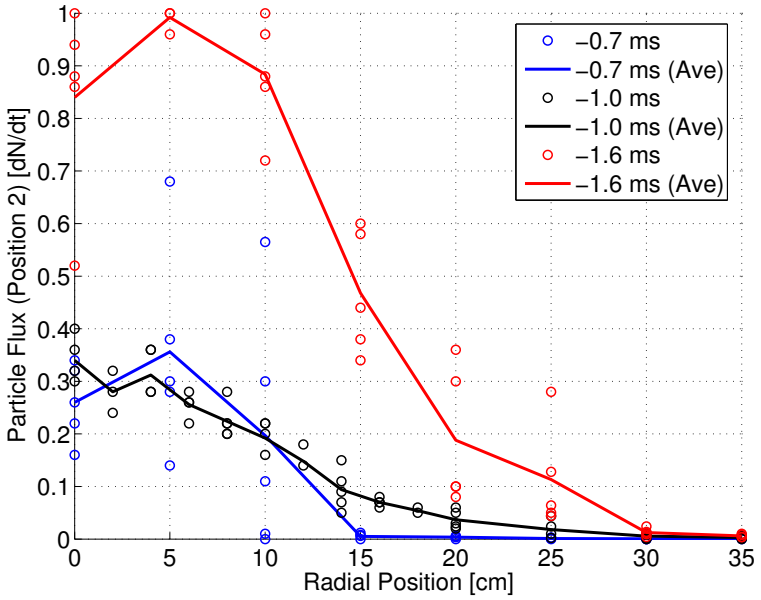

(a) Langmuir profiles.

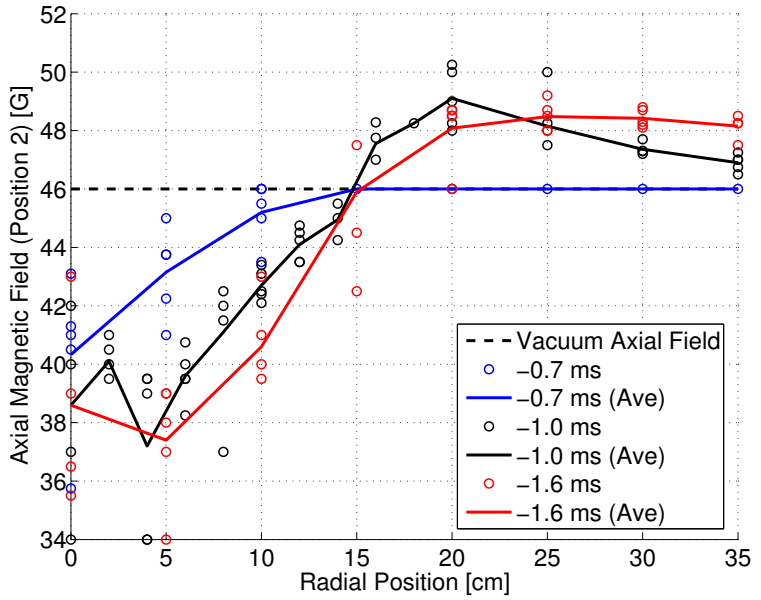

(b) Magnetic profiles.

Figure 3.51: Langmuir and magnetic profiles for various puff timings at 20 psig (Position 2).

one examines the differences in the Langmuir profile between the three cases, it becomes apparent that the peak particle flux at any position scales like the puff-RMF start delay time. When the slight difference in plasma velocity is taken into account, this resulting trend in peak density is slightly more pronounced. The observation of higher plasma peak density scaling with the puff timing delay is not particularly surprising since the mass of the FRC scales in this way. Also, the fact that the RMF seems to have no difficulty driving current at these densities means that there is a strong confining magnetic field which increases the pressure within the FRC.

An examination of the axial magnetic field profiles shows that this is the case, exhibiting a trend of higher diamagnetic current corresponding to higher particle inventory. Since in this case (20 psig and the stated delay times) the discharge appears to be density-limited, the fraction of the particles driven by the RMF is close to unity, thus the amount of driven current is proportional to particle count as described in Section 1.4. This increase in current/particles/pressure as a result of increased magnetic field also results in a slightly increased plasma radius as that is observable in both the Langmuir and B-probe traces.

One may also notice that the decay in magnetic field is less when the particle count is lower. This is due to the fact that, at lower densities, the collision rate is reduced, which results in a lower resistivity. This drop in resistivity more than makes up for the drop in inductance due to the slightly reduced size of the plasmoid.

Similarly to the 20 psig case, when the puff delay time is increased from the -0.7 ms to the -1.0 ms setting, the result is an increase in radius, peak density,

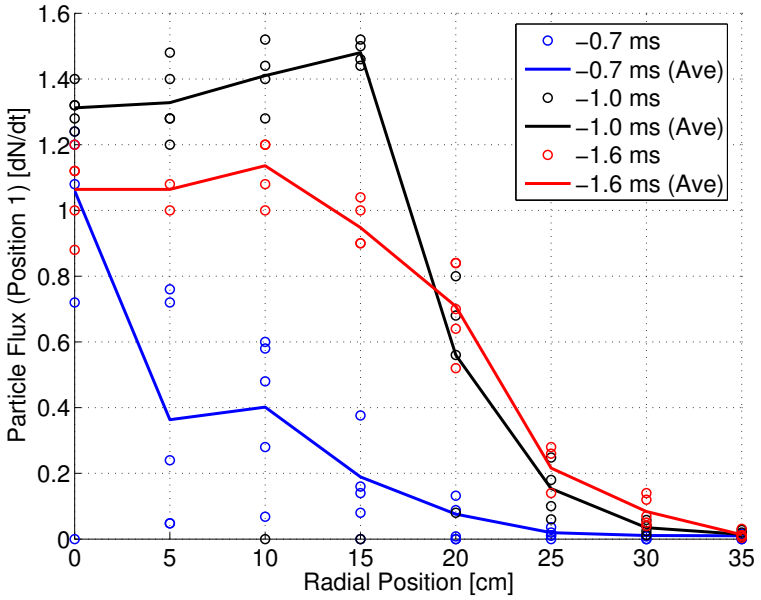

(a) Langmuir profiles.

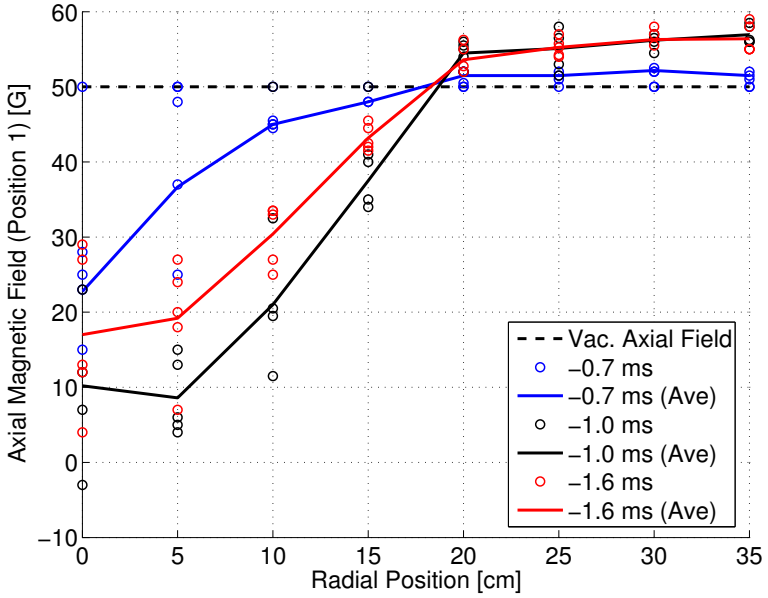

(b) Magnetic profiles.

Figure 3.52: Langmuir and magnetic profiles for various puff timings at 40 psig (Position 1).

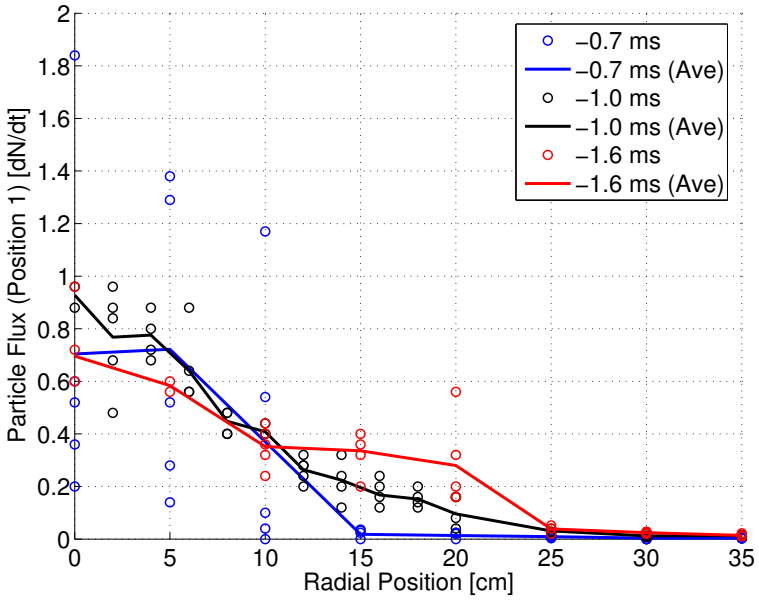

(a) 20 psig.

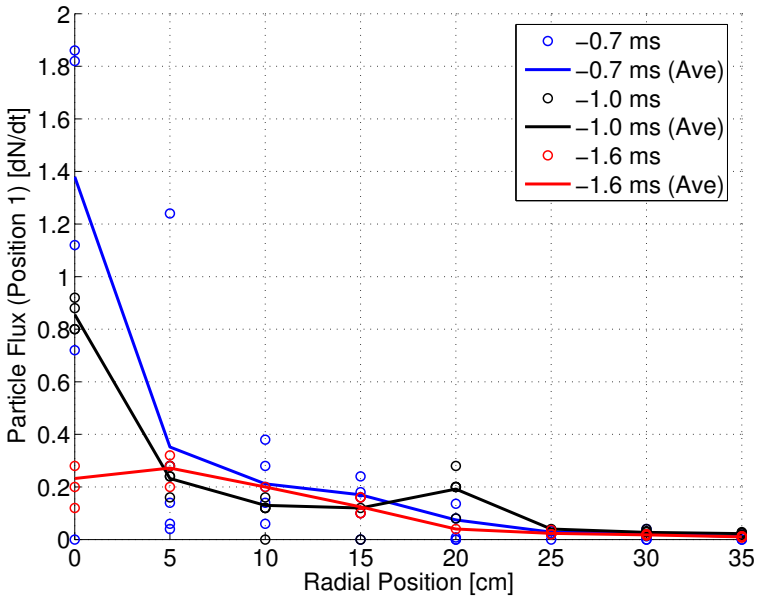

(b) 40 psig.

Figure 3.53: Profile of the leading edge plasma pulse measured at position 1 for 20 and 40 psig line pressure.

and driven current. However, these quantities do not increase further as the delay is increased -1.6 ms. In the Langmiur profile, once one factors in the decrease in velocity, the peak density is the same for these two conditions. Also there is no increase in plasma radius between the two timings. The B-profile reveals a slight decrease in driven current from -1.0 ms to -1.6 ms. This is due to the fact that as the mass increases over this range, the RMF starts to lose current drive efficiency (see Figure 3.48), and that the higher density results in a shorter flux lifetime.

In addition to measuring the peak density of the bulk plasma for the various conditions mentioned above, the leading edge plasma pulse was also examined. There were two proposed mechanisms for the origin of this pulse. One was that the plasmoid was ionizing and sweeping along trace neutral gas that had leaked out of the cone prior to the RMF discharge. The other was that it was one of two jets of plasma emanating from upstream and downstream ends of the FRC, as a result of plasma particles leaking across the separatrix (a typical occurrence in FRC experiments). It appears that the former theory is incorrect since, as the puff timing was swept, there would have been differing amounts of gas in front of the FRC as it was ejected from the cone, which would have resulted in differing amounts of leading edge plasma. This was not observed. It was found that the amplitude of this pulse was independent of puff timing at 20 psig (Figure 3.53a), and actually reduced slightly with the amount of gas in front of the plasmoid during testing at 40 psig (Figure 3.53b).

3.10 Cone and Adjustable Bias Study

In addition to the puff timing and gas pressure, the cone and adjustable bias settings have a large impact on the operation of the thruster. The optimal relative levels of the two thruster bias systems were determined during earlier testing (see Section 3.5), however, the effect of varying the absolute level of these fields still needed to be determined. The intensity of the axial magnetic field is a critical parameter affecting the formation of the plasmoid within the cone, and the subsequent acceleration and ejection. Unlike the drift bias field, whose main purpose is to provide the ability to study the plume, the cone and adjustable biases are part of the thruster, and integral to its operation.

In order to determine the effect of changes to these fields, a series of tests were performed in which the charge voltage of both bias systems (maintained at a ratio of 1:1) were swept from 0 to 300 V. Once again, multiple shots were taken at each setting to gain a more accurate estimate and determine the uncertainty in performance at a particular setting.

One can see in Figure 3.54a, that the impulse rises with the bias field intensity as the charge on the capacitor banks is increased from 0 to 50 V. However, at 50 V, the impulse reaches a local maximum and then begins to decrease with increasing bias. This continues until roughly 100 V, at which point the impulse reaches a local minimum and begins to increase again. This second region of increasing impulse continues until roughly 200 V, where it reaches another local maximum, and then slowly decreases as the bias is further increased. This intriguing trend

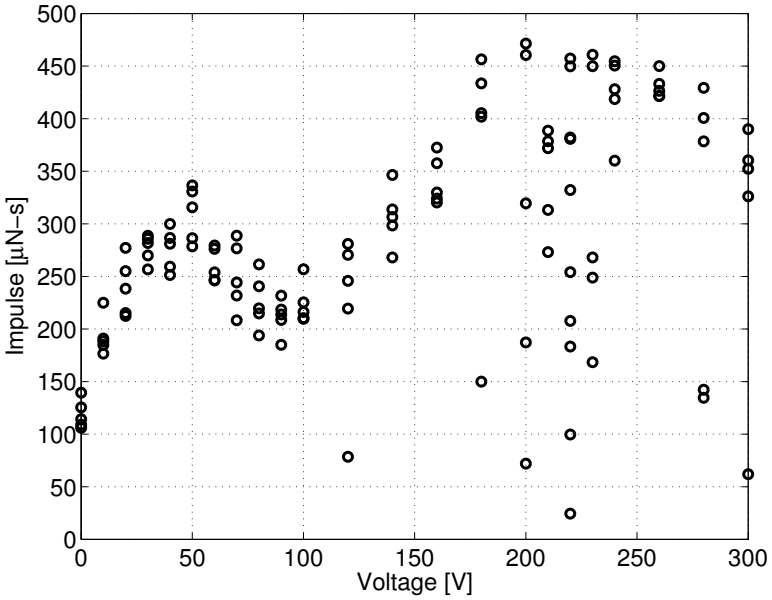

(a) Impulse.

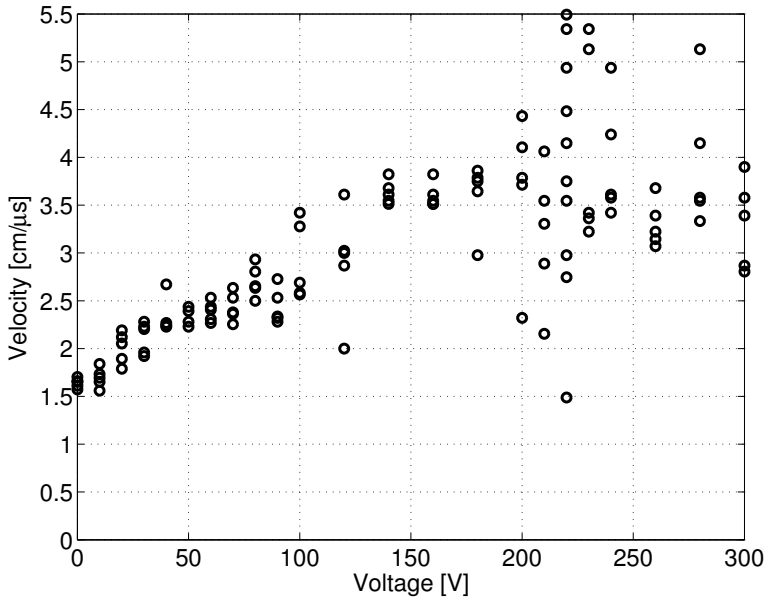

(b) Velocity.

Figure 3.54: Impulse and velocity for various cone and adjustable bias settings.

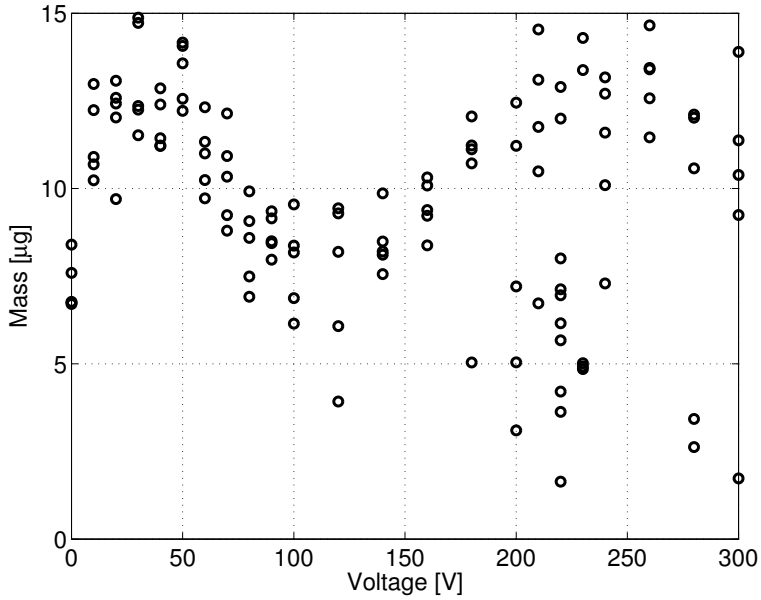

(a) Mass.

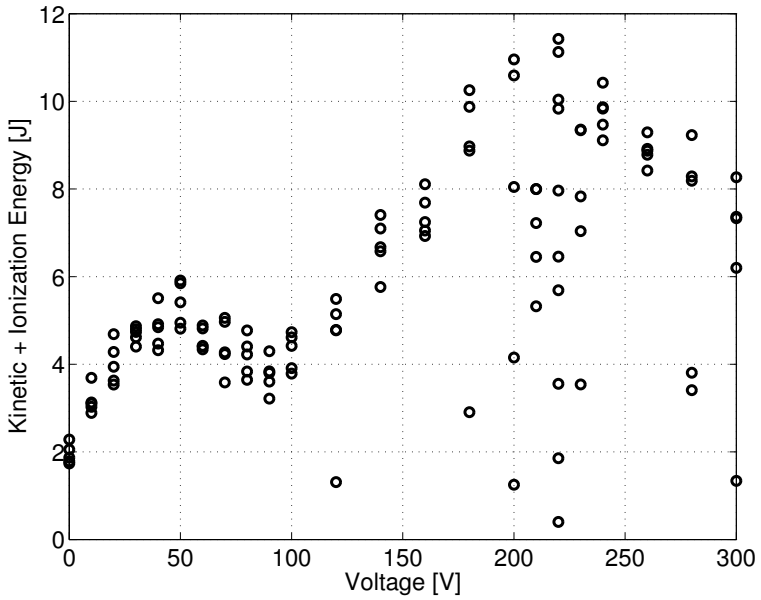

(b) Kinetic energy + ionization energy.

Figure 3.55: Mass and kinetic + ionization energy for various cone and adjustable bias settings.

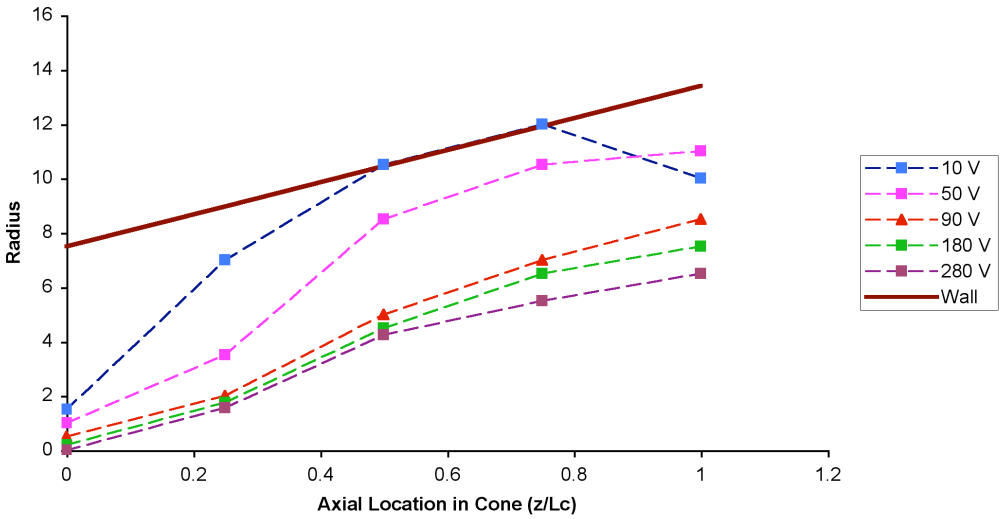

Figure 3.56: Distribution of azimuthal current within cone for various bias conditions.

is not reflected in the plot of the velocity, which increases linearly with increasing bias field (see Figure 3.54b).

This results in the mass and energy plots displaying the same unusual trend as the impulse (Figures 3.55a and 3.55b). The mass is relatively constant until 50 V, then decreases until $\sim$ 100 V, then increases again back to its original value by $\sim$ 200 V, and remains constant after that. The mechanism behind this behavior can be revealed through an examination of the axial profile of the current driven in the plasma as measured by the external B-probes (see Figure 3.56).

One can see from the plots of the location of the current within the cone that the FRC forms further downstream as the intensity of the bias field is increased. At any axial location there will be magnetic gradient tending to push downstream any diamagnetic current until the RMF can drive enough current to form a region

of axial field that is less than both the upstream and the downstream values. The current will be drawn to this minimum in the field, which further decreases the field in that region. Eventually enough current collects and is driven in this location to reverse the field and form an FRC. At low bias field conditions, this point is roughly halfway down the cone. However, as the axial bias is increased, this point moves downstream, eventually leaving the cone altogether, and the current conglomerates in the drift chamber. Internal probing using the cone B-probe confirms there is no field reversal when the bias is high.

When bias is at low values ($V_{\text{chg}} < 50$), the formation takes place within the cone, and at high values ($V_{\text{chg}} > 200$), the formation takes place outside of the cone. However at intermediate values ($50 < V_{\text{chg}} < 200$) the formation process takes place in the very end of the cone, where there is a thick shell of copper flux conserver within the chamber. This shell is thick enough to shield out the high-frequency RMF (as it was designed for a soak through time that was longer than the FRC lifetime), preventing current drive from occurring within this region, forcing the RMF to drive current elsewhere. Eventually all of the driven current merges into an FRC and translates downstream, but the formation process is handicapped by having to take place in a less optimal manner.

Internal probing reveals the shape of the Langmuir profile is similar as the cone and adjustable bias is swept. If one takes into account the velocity of the plasma by the time it reaches probe 2, the peak densities are all very similar throughout the profile. Since the formation process is still taking place near the upstream probes, their data are less reflective of characteristics of the plasmoid far downstream of

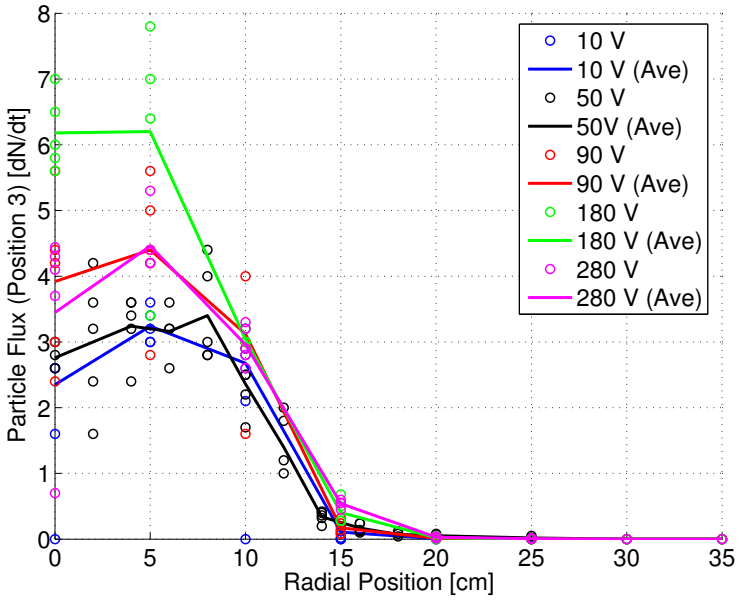

Figure 3.57: Langmuir profiles for various cone and adjustable bias settings (position 3).

the thruster.

In contrast to the similarity between the plasmoids revealed by the Langmuir probes, the internal B-probes show that the diamagnetic current is seen to increase (by the time the plasmoid reaches probe 2) as the bias is increased. This increase, however, is a result of the fact that the plasmoid begins life further downstream at higher bias values, thus it has had less time for the current to decay.

It was thought that, since the gas was required to travel further downstream to fuel the formation process in the higher bias cases, the plasmoid impulse could be increased and more efficient operation could be attained by increasing the delay between the start of the puff and the start of the RMF. To this end, a puff timing sweep was performed at the higher bias condition. However, there was very little

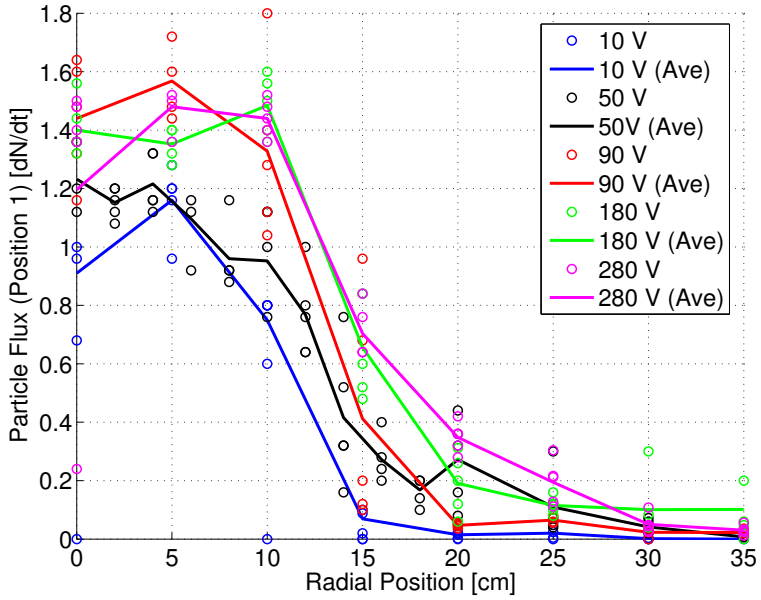

(a) Langmuir profiles.

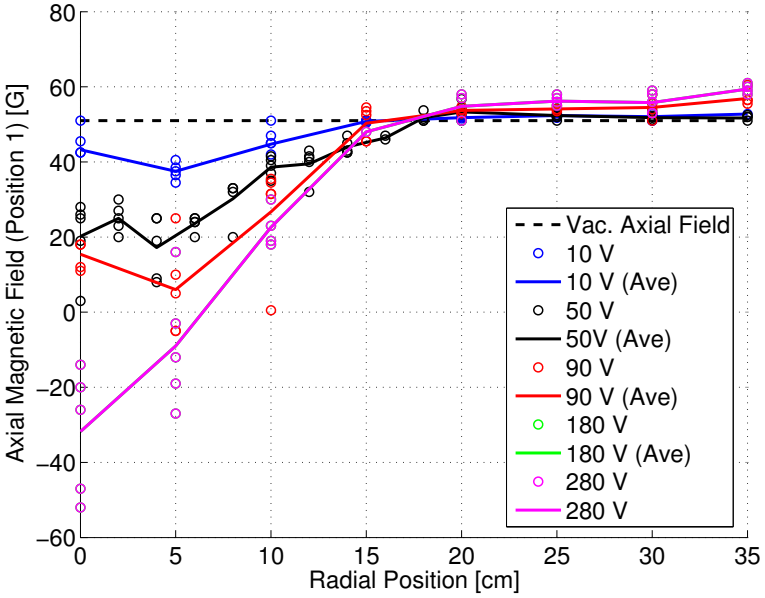

(b) Magnetic profiles.

Figure 3.58: Langmuir and magnetic profiles for various cone and adjustable bias settings (position 1).

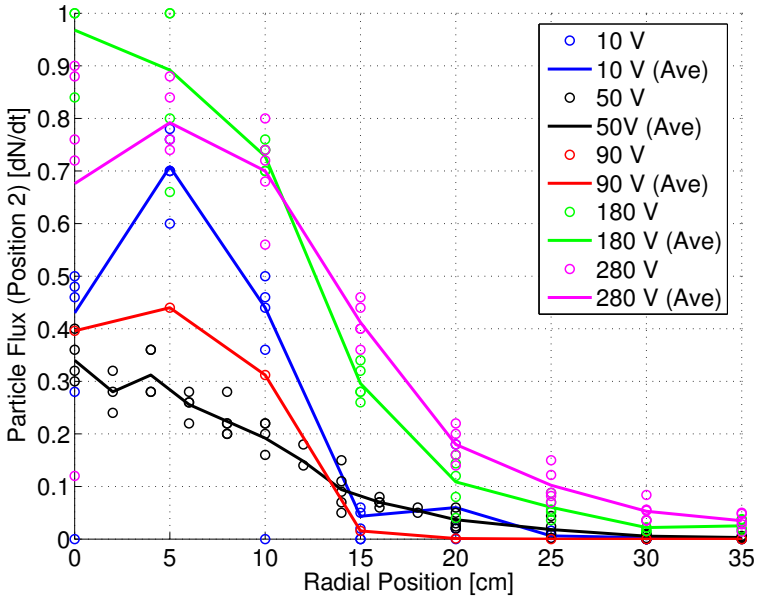

(a) Langmuir profiles.

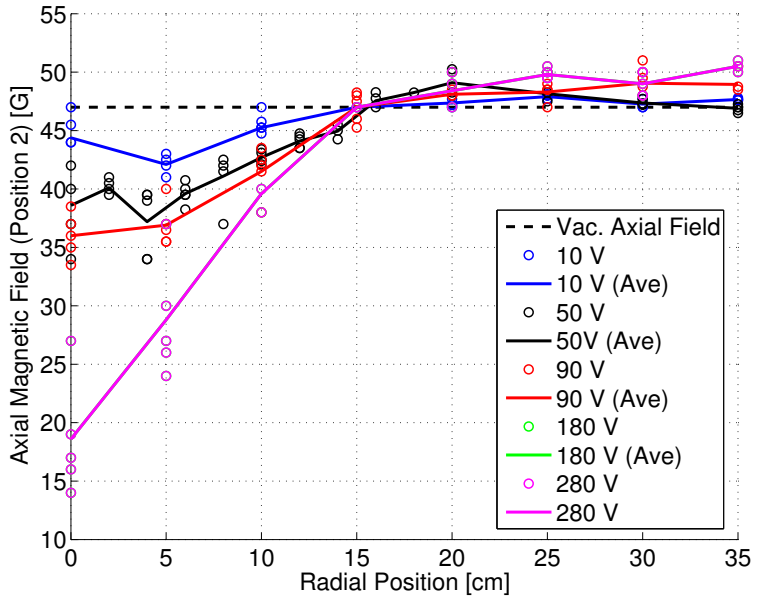

(b) Magnetic profiles.

Figure 3.59: Langmuir and magnetic profiles for various cone and adjustable bias settings (position 2).

increase in performance observed throughout the sweep. The relatively efficient formation of the FRC downstream of the ends of the RMF section is an interesting phenomenon, and will most likely be the subject of a future study in RMF current drive technology similar to the Plasma Magnet experiment [34]. The main lesson in this case, is that the RMF is capable of efficiently depositing energy anywhere in the vicinity of the antennae.

3.11 Alternative Propellants

Although the vast majority of the testing that was performed with ELF utilized nitrogen as a propellant, there was some testing which took place to investigate the feasibility of the use of alternative propellants. There are several properties which vary across the propellants tested that were thought to have an effect on the operation of the thruster including atomic mass and the ionization cross section. Species tested included: hydrogen, deuterium, helium, nitrogen, oxygen, nitrous oxide, a stoichiometric mixture of hydrogen and nitrogen resembling hydrazine, dry air, humid laboratory air, argon, and xenon.

Oxygen, nitrous oxide, dry air, and humid laboratory air all behaved in a similar way to nitrogen, and much of what was learned in the previous sections applies to these propellants as well. Slight differences in the neutral gas propagation speed within the cone was noticeable in the FIG data and in the dilation of the puff timing trends in time. Also, slight differences in the efficiency of RMF to kinetic energy conversion, the corrosion of the PI due to operation in oxygen, and the

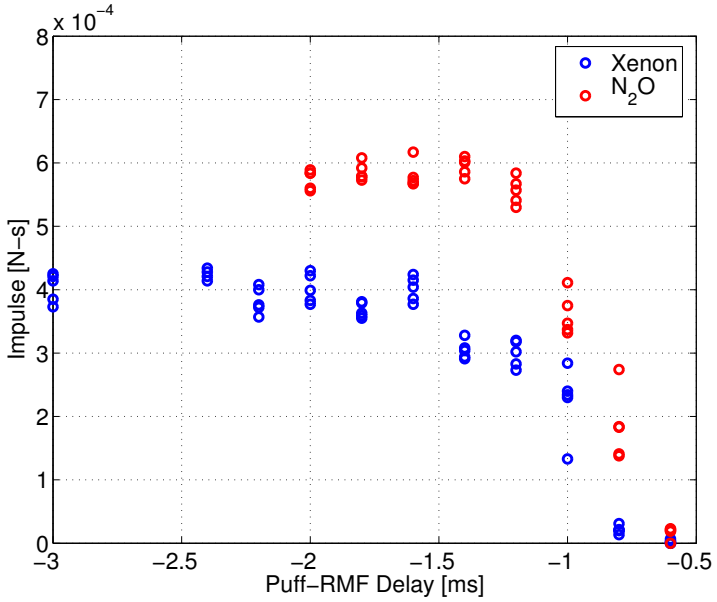

(a) Impulse.

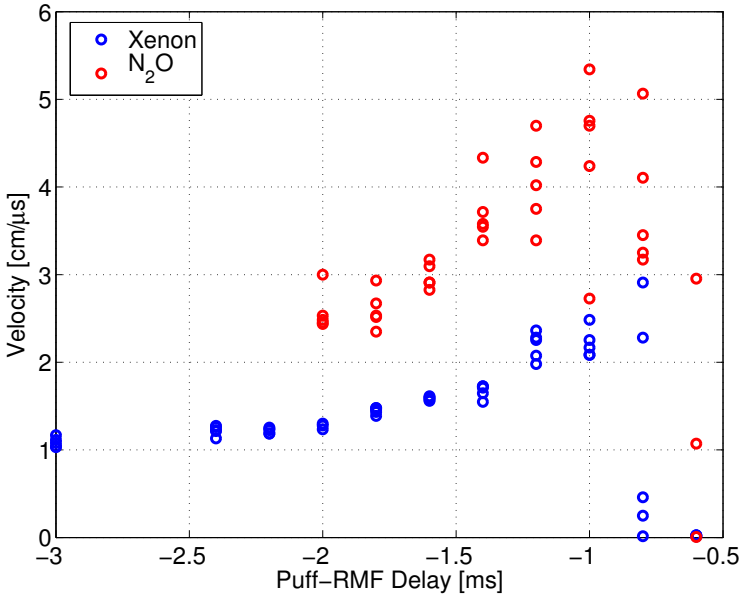

(b) Velocity.

Figure 3.60: Impulse and velocity for various puff timings during operation in xenon and nitrous oxide.

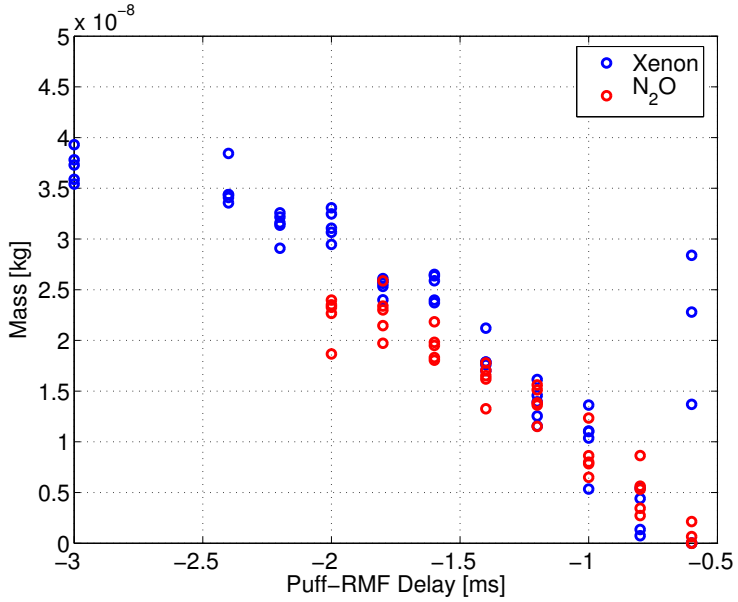

(a) Mass.

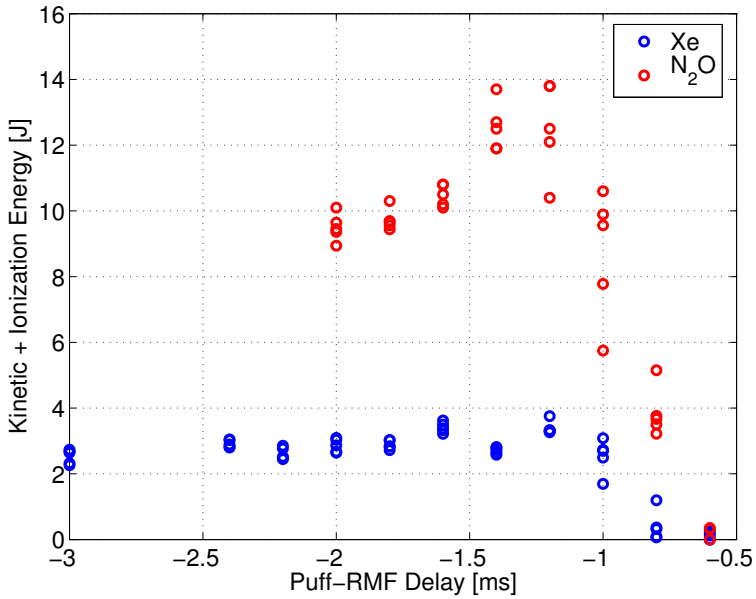

(b) Kinetic + ionization energy.

Figure 3.61: Mass and kinetic + ionization energy for various puff timings during operation in xenon and nitrous oxide.

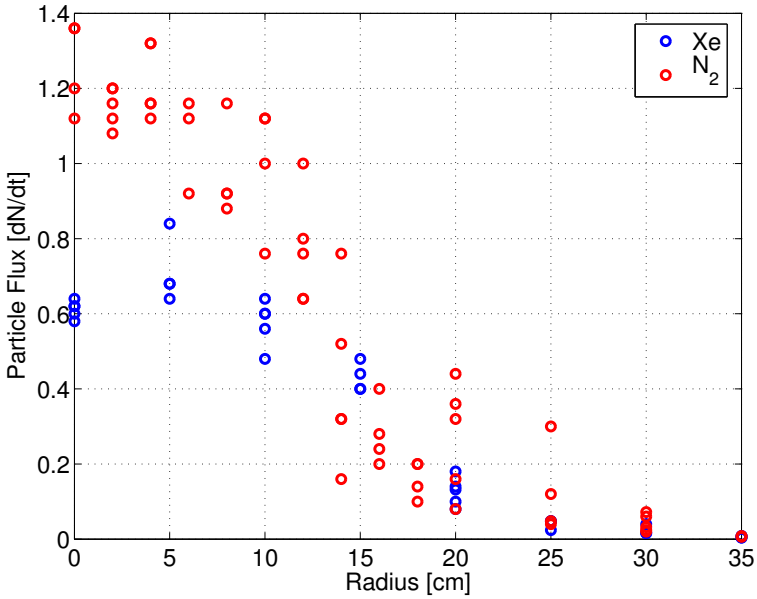

Figure 3.62: Langmuir profiles of xenon and nitrous oxide at position 2.

deleterious effects of water (when operating using the humid Seattle air) on the base pressure of the vacuum system.

While the puff timing trends of xenon and N_2O possess similar characteristics with the trends obtained using nitrogen, the overall performance is improved with N_2O and significantly worse using xenon. An examination of the circulating energy in the tank circuit with respect to time (Figure 3.63) reveals that during operation in xenon, the main RMF ionization event took place at a significantly lower energy than nitrogen and N_2O. This is due to the difference between the initial gas distribution, density, and ionization cross section in xenon. This resulted in a slow input of energy over many RMF oscillations, rather than the high power input of energy at high RMF amplitudes (as is the case in N_2O). This lower energy formation permits more opportunity for energy losses to occur (see Section 4.1).

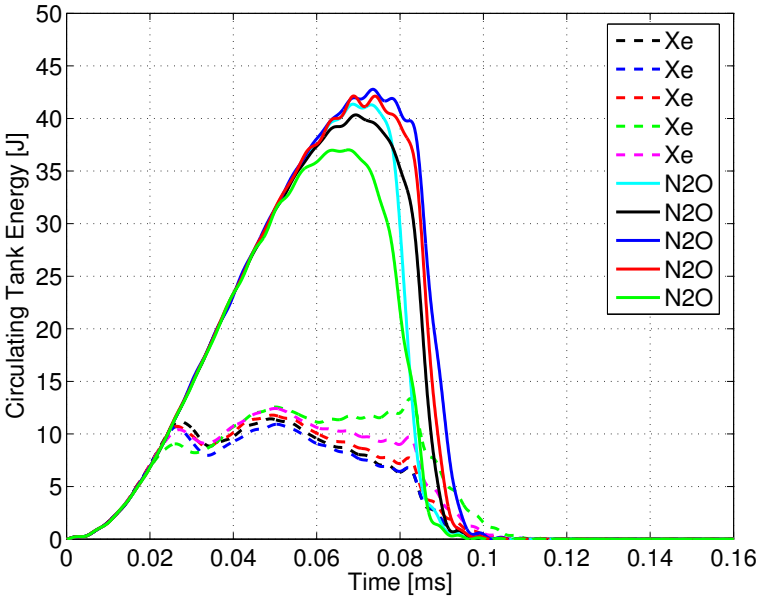

Figure 3.63: Circulating tank energy during operation in xenon and nitrous oxide.

Thus, the increased efficiency of nitrogen is a consequence of the RMF amplitude required for the ionization process to occur, since the circulating energy in the tank circuit and power of the formation process is also a function of RMF amplitude.

There was surprisingly few differences between operation in nitrogen, argon, and xenon considering the mass difference between the species. It was thought that the large gyro-orbits of the heavier mass elements would result in a plasmoid which would rapidly diffuse throughout the entire drift chamber, however, only a small increase in the spread of the density profile (compared to nitrogen) were observed as the plasmoid traveled downstream (see Figure 3.62). It is thought that large electric fields are developed at the edge of the plasmoid in order to prevent the loss of ions with large gyroraii and maintain quasineutrality. It is these electric fields, rather than the magnetic fields at the edge of the plasmoid, which confine

the particles.

Testing in the lighter elements revealed very different behavior than that exhibited by the intermediate and heavy elements. While testing in hydrogen, deuterim, and helium, the RMF experienced significant difficulty ionizing the neutral gas, sometimes requiring over 100 pulses before the discharge would occur, while no ionization took place when operating in hydrogen. This is due to the fact that the RMF frequency in deuterium and helium was roughly the same as the ion-cyclotron frequency (not much larger, as in the other gases), and was lower than the ion-cylotron frequency of hydrogen. Because of this, the RMF was no longer driving only the electrons, and the azimuthal current required to form the FRC could not be developed (see Section 1.4).

Chapter 4

Discussion

In this chapter, the utility of the ELF system as a thruster concept is explored. Specifically, the relevant energy loss mechanisms inherent in the thruster are explored, and estimates for these losses for the conditions present during the standard shot are computed. The potential efficiency of the thruster is discussed using the example of the use of xenon as a propellant to illustrate the variability of the specific amount of energy lost in each mechanism. A brief discussion of possible future work is also included.

4.1 Thruster Efficiency

The thruster efficiency (η_t) is the measure of the ratio of propulsive power to the power consumed by the thruster. In ELF, this ratio is equal to the kinetic

energy of the exhausted plasmoid divided by the total energy put into the system.

$$\eta_t = \frac{E_{KE}}{E_{in}} \tag{4.1}$$

Where E_{in} is the energy input into the system by the RMF. It should be noted that although the plasma is accelerated through the $\mathbf{j} \times \mathbf{B}$ interaction with the bias field, there is no energy input from the bias field over the timescales of the formation and ejection process due to the segmented flux conservers.

In order to understand the processes taking place within the thruster, one must first consider separately the various loss mechanisms which come into play. The thruster efficiency can then be expressed in terms of these loss channels.

$$\eta_t = \frac{E_{KE}}{E_{KE} + E_{th+B} + E_{iz} + E_{\eta} + E_{sc} + E_{conv} + E_{rad}} \tag{4.2}$$

Where E_{KE} is the kinetic energy of the ejected plasmoid, E_{th+B} is the thermal plus the magnetic energy within the FRC and compressed external magnetic field, E_{iz} is the energy required to ionize the neutral particles, E_{η} is the resistive losses in the flux conservers, E_{sc} is the fraction of the RMF energy that cannot be deposited into the FRC due to screening currents, E_c is the energy lost due to particle convection away from the FRC, and E_{rad} is the energy lost to radiation. These mechanisms are described in the following subsections.

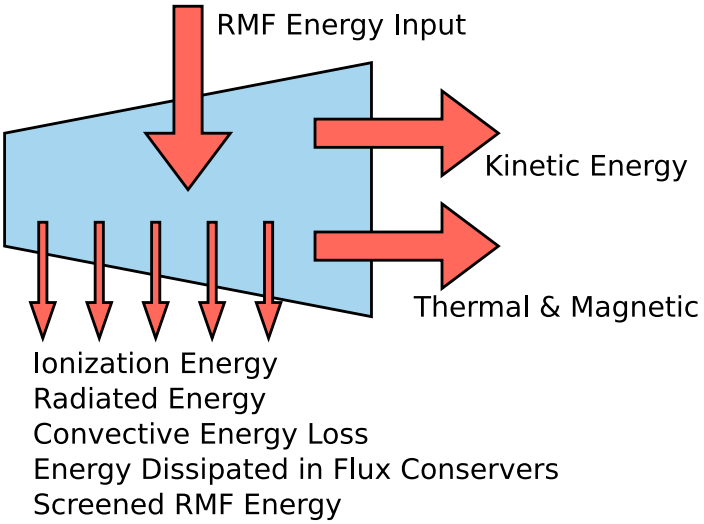

Figure 4.1: Various energy channels present in ELF.

4.1.1 Kinetic Energy

The kinetic energy of the ejected plasmoid is the only useful form of energy from the standpoint of a thruster. It is the goal of any thruster to maximize the fraction of the input energy which becomes converted to kinetic energy.

$$E_{KE} = \frac{1}{2} m_{frc} v_e^2 \tag{4.3}$$

However, one must also consider the fact that for a given space-flight system and mission ΔV, one must balance the power consumed by the thruster against the thrust, mass of the system, mass of propellant used, and various other mission parameters. Thus, the desired amount of kinetic energy per plasmoid, FRC mass, and exhaust velocity may all be subject to change for any particular spacecraft and mission.

4.1.2 Thermal and Magnetic Energy

Upon formation within the RMF section, the FRC is hot and dense. Through the expansion process, the thermal energy, as well as the internal and external magnetic energies are converted to bulk kinetic energy. In ELF, the expansion takes place first as the FRC translates and expands within the cone, then as it exits the region of diverging magnetic field in the drift chamber. The specific amount of energy converted depends on the details of the expansion process, and the expansion ratio. The sum of the thermal and magnetic energies within the FRC and the compressional energy of the axial bias field can be expressed as a function of the temperature and the total number of particles.

$$E_{th+B} = \frac{5}{2} NkT \tag{4.4}$$

Any thermal and magnetic energy remaining in the plasmoid once it has left the thruster is considered a frozen flow loss. However, due to the limited size of the drift chamber, the FRC cannot be expanded to the point at which all this energy is converted to kinetic energy. Thus, experimentally, one must consider the remaining thermal and magnetic energy in the ejected plasmoid to be useful energy when optimizing the thruster, since this energy could have been converted if the chamber were large enough.

4.1.3 Ionization Energy

In order to confine and accelerate a particle within an FRC, that particle must be ionized. The energy required to ionize the plasma leaves the thruster along with the plasma, and must be counted as a frozen flow loss. This amount of energy is simply the amount of required ionization energy (plus the molecular dissociation energy, if the propellant is multi-atomic) per particle, multiplied by the total number of particles.

$$E_{iz} = N(\varepsilon_{iz} + \varepsilon_{diss}) \tag{4.5}$$

Where ε_{iz} is the ionization energy per ion, and ε_{diss} is the dissociation energy per ion (not per molecule). It is undesirable to multiply ionize the propellant due to the fact that this energy is not recoverable, and is lost as the plasma is ejected.

4.1.4 Resistive Losses in the Flux Conservers

During the residence time of the FRC within the formation section, the axial bias field becomes compressed against the flux conservers at the wall of the thruster. This requires that a current be flowing in the flux conservers during this time. Since they posses a finite resistivity, there will be some energy dissipated during this period. The amount of this energy is simply equal to the integral of the resistive

power, summed over all flux conservers.

$$E_\eta = \sum_k \int I_k^2 R_k \mathrm{d}t, \tag{4.6}$$

where I_k is the current flowing in a particular flux conserver, and R_k is the resistance of the flux conserver. It must be noted that current only flows within a skin depth of the material, determined by the resistivity of the material and the residence time of the FRC. The specific amount of energy lost to this mechanism depends on the energy content of the plasma, the residence time within the thruster, and the design of the flux conservers.

4.1.5 Screened RMF Energy

As mentioned in Section 1.4, the penetration and current drive capability of the RMF is governed by the two dimensionless parameters γ and λ, with RMF penetrating the FRC and driving current when $\frac{\gamma}{\lambda} > 1$, and the RMF being screened by edge currents in the plasma and no current drive occurring when $\frac{\gamma}{\lambda} < 1$.

In the way the RMF is operated in ELF, the RMF amplitude is much more than required for full penetration and current drive prior to the formation process, however, as the circulating energy is drained from the tank circuit, the amplitude eventually is reduced to a point at which penetration and current drive can no longer occur. At this point, any energy remaining in the tank circuit is dissipated in the plasma external to the FRC, which is attached to the thruster field lines, and considered not to be important to the production of thrust. The mitigation

of this loss is intimately tied to the operation of RMF, and the plasma parameters during discharge.

4.1.6 Energy Loss due to Particle Convection

Convection losses occur when a particle is lost from confinement within the FRC and the energy carried by that particle is lost in a way that is unproductive for thrust. It should be noted that any particles lost from confinement within the FRC after the plasmoid has achieved a significant fraction of its final velocity still contribute to the thrust developed. In addition, it has been discovered that during the phase of formation while the RMF is still actively driving current there is a swirling flow present that prevents the loss of particles for the duration of the RMF sustainment [2]. Thus convective losses can only occur during the brief interval of time after the RMF has stopped driving current, but before the ejection process has occurred.

During this time, particles are lost across the FRC separatrix, convect along the magnetic field lines, and form two jets of particles flowing away from the FRC along the axis of the thruster (one in the upstream direction, and one flowing downstream). The particles in the downstream flowing jet are pushed along by the FRC as it is ejected and contribute to the developed thrust. Particles in the upstream jet flow back into the body of the thruster, however, due to the strong mirror field, much of these are reflected back downstream, and still contribute to the thrust. Only particles which find their way to a material surface contribute to convective losses. As the confinement properties of the ejected FRC are improved,

the amount of energy lost via this mechanism is reduced.

4.1.7 Radiative Losses

Any electromagnetic radiation emitted by the plasma during a discharge is unrecoverable energy and constitutes a loss mechanism. In ELF the radiative losses are dominated by line radiation from excited and subsequently de-excited atomic states. There will always be some degree of radiative losses present during the ionization, formation, and ejection phases of operation, however, the specific amount of energy radiated is heavily dependent on the plasma parameters during the operation of the thruster.

4.2 Standard Shot Thruster Efficiency

In this section, the amount of energy going into the various channels described in the previous section is computed for the standard shot of Section 3.7. It must be noted that this is not a particularly efficient shot with respect to various other explored ranges of operational space (the observed efficiencies ranged from 8 - 40 %). However, the most information is known about operation at this condition, due to the fact that it was used as a point of comparison against all other shots.

4.2.1 Kinetic, Thermal, and Magnetic Energy

During the standard shot, the energy into the plasma due to the RMF was found to be ~ 46 J. The kinetic energy of the ejected plasmoid was found to be ~ 3.8 J,

making the thruster efficiency roughly 8 %. While this may seem fairly low, it must be noted that this quantity is mainly a reflection of the constraints placed on the operation of the thruster due to the limits of the experimental setup as noted in the previous section. The thermal and magnetic energy found to be contained in the ejected plasmoid during it's transit of the drift chamber was found to be ~ 3.7 J. Thus, the thermal/magnetic to kinetic energy conversion of the expansion process was roughly 50 % (i.e. $E_{th+B} \approx E_{KE}$).

Since this is mainly a reflection of the limited size of the drift chamber, and virtually all of the thermal and magnetic energy are believed to be recoverable via the expansion process, the thermal and magnetic energy are considered useful forms of energy, and should be included in an expression of the efficiency of the experimental ELF thruster.

$$\eta_t = \frac{E_{KE} + E_{th+B}}{E_{KE} + E_{th+B} + E_{iz} + E_{\eta} + E_{sc} + E_{conv} + E_{rad}} \tag{4.7}$$

If one takes into consideration the limitations of the experimental setup, and that the thermal and magnetic energy are recoverable, then the thruster efficiency of the standard shot becomes 16 %.

4.2.2 Resistive Losses in the Flux Conservers

The amount of energy resistively dissipated in the flux conservers can be approximated using measurements of the increase in the local magnetic field beneath each flux conserver as measured by the external B-probes. Using the magnetic field

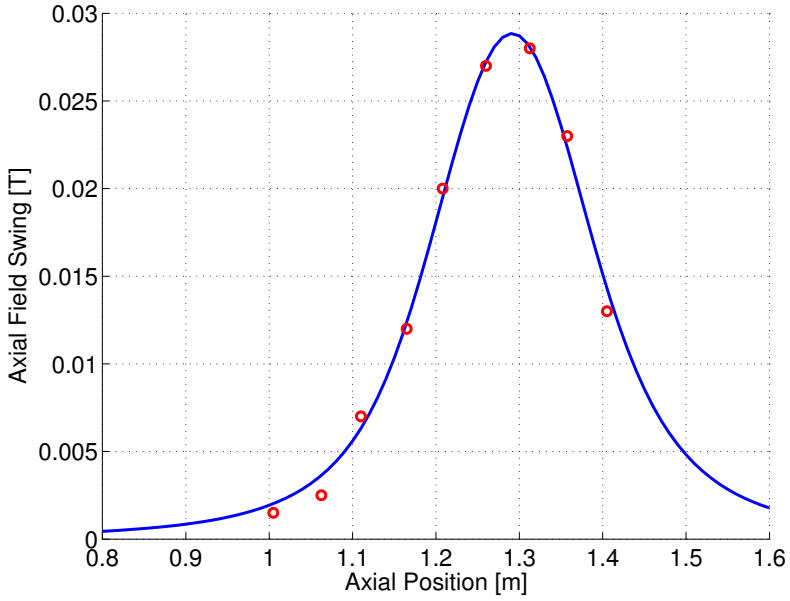

Figure 4.2: Simulated magnetic field profile due to currents in the flux conservers compared to observations.

solver described in Section 2.2, and fitting to the observed data, estimates for the amount of current carried by each of the flux conservers as a function of time can be made (see Figure 4.2).

Since the increased magnetic field is only present for a short time, the current in the flux conservers can only be carried within a skin depth of the surface. The characteristic frequency for calculating this distance is determined by the rise and fall time of the external field, this time is half of a period of the characteristic frequency.

$$\delta = \sqrt{\frac{2\eta_c}{\omega\mu_o}} \tag{4.8}$$

The skin depth is calculated to be 0.65 mm, the width of a flux conserver segment

is $\sim$ 3 cm. The resistive power dissipation for a single flux conserver can be determined from the resistance and the amount of induced current.

$$R = \frac{\eta l}{A} \tag{4.9}$$

$$P(t) = (I(t))^2 R \tag{4.10}$$

Where A is the cross sectional area of the current-carrying portion of copper (δ times strap width), and l is the circumferential length of the flux conserver. The time dependence of the current is determined by experimental observations of the external field. The total dissipated energy can then be determined by integrating the resistive power dissipated in each flux conserver.

$$E_\eta = \sum_k \int P(t)_k \mathrm{d}t \tag{4.11}$$

During the standard shot this quantity was found to be $\approx$ 0.16 J.

4.2.3 Screened RMF Energy

As stated in the previous section, the RMF will penetrate the plasma and drive current as long as $\frac{\gamma}{\lambda} > 1$. During the standard shot, this ratio was found to be ~ 10 when the RMF was at maximum amplitude. The RMF was observed to be fully penetrated into the plasma by the internal B-probe within the cone throughout most of the residence time of the FRC, however, as the RMF amplitude became reduced through the deposition of tank energy into the plasma, $\frac{\gamma}{\lambda}$ was also reduced.

The ratio of λ and γ can be expressed in terms of the imposed RMF field.

$$\frac{\gamma}{\lambda} = \left(\frac{\gamma}{\lambda}\right)_{max} \frac{B}{B_{max}} \tag{4.12}$$

When the amplitude of the RMF field during the standard shot dropped to 10 % of its maximum value the fields were screened and current drive ceased, dissipating any remaining tank energy in a way not useful for the purposes of creating thrust. This corresponds to the point at which 99 % of the energy in the RMF tank circuit has been drained. Thus, during the standard shot, roughly 1 % of the energy in the tank was lost, corresponding to ≈ 0.5 J.

4.2.4 Convection

As previously mentioned, losses attributable to particle convection primarily occur during the time between the end of RMF current drive, and the ejection of the FRC from the thruster section. During the standard shot, this time is roughly 10 μs.

The particle confinement timescale for an FRC has been experimentally determined to be roughly given by,

$$\tau_n = \left(\frac{m_i}{2\pi m_e}\right)^{1/2} \frac{s^4}{\omega_{cie}(1 + T_i/T_e)} \tag{4.13}$$

where $s = R/r_{gie}$ is the ratio of the radius of the magnetic null to the ion gyroradius in the external field, and ω_{cie} is the ion cyclotron frequency in the external field

[35]. For the conditions present during the the initial translation phase, the particle confinement timescale is computed to be $\tau_n = 91\langle Z\rangle^3 \mu$s.

The total number of lost particles can thus be expressed as

$$N_l = N\left(1 - e^{t/\tau_n}\right) \tag{4.14}$$

where N_l is the number of lost particles. During the 10 μs of interest during the standard shot, roughly 10 % of the total particle inventory is lost. Since the loss occurs in both the upstream and downstream directions, roughly half of these lost particles travel downstream ahead of the FRC, and still contribute to the produced thrust. The other half travel upstream back into the cone, where roughly half are assumed to be reflected and half are assumed to recombine on a material surface. Thus the number of particles lost due to convection that do not contribute to the total thrust is ~ 2 % of the initial FRC inventory. The energy of the lost particles can be computed as the sum of the thermal, magnetic, and ionization energies per particle.

$$E_c = N_l\left(\frac{5}{2}kT + \varepsilon_{iz} + \varepsilon_{diss}\right) \tag{4.15}$$

$$E_c = N\left(1 - e^{t/\tau_n}\right)\left(\frac{5}{2}kT + \varepsilon_{iz} + \varepsilon_{diss}\right) \tag{4.16}$$

For the standard ELF conditions, this energy is computed to be ~ 0.24 J.

4.2.5 Radiation

Due to the transient nature of the discharge in ELF, there is inadequate time for the atomic processes to come into coronal equilibrium. Thus, the radiative power emitted by the plasma in ELF must be determined using numerical models. Carolan and Piotrowicz [5] have computed the time-dependant normalized radiative power of carbon and oxygen immersed in a sea of hot electrons for a range of electron densities and temperatures (see Figure 4.3).

The curves for carbon and oxygen are similar enough over the temperature and density ranges observed in ELF that the behavior of nitrogen can be extrapolated with some degree of confidence. The electron density is assumed to be proportional to the driven current within the RMF section (a reasonable assumption considering the current drive regime, see above section). The total temperature can be obtained from the number density and the external magnetic field using pressure balance (Equation 1.4). Due to the disparity between the electron and ion masses, the thermalization of energy between the species takes place over a timescale of roughly $\tau_{eq} \approx \frac{m_i}{2m_e\nu_{ei}} \approx 57$ μs, therefore, the total temperature can be interpreted as hot electrons and cold ions. The ionic density is assumed to be equal to the electron density ($\langle Z \rangle \approx 1$, an assumption that will be justified in the next section). In this way, the radiative energy can be computed by fitting the signal from an external magnetic probe, computing the temperature and density profiles within the cone as a function of time, and integrating the radiated power. Performing the above analysis during an average standard shot, the radiated power was computed to be ≈ 35 J.

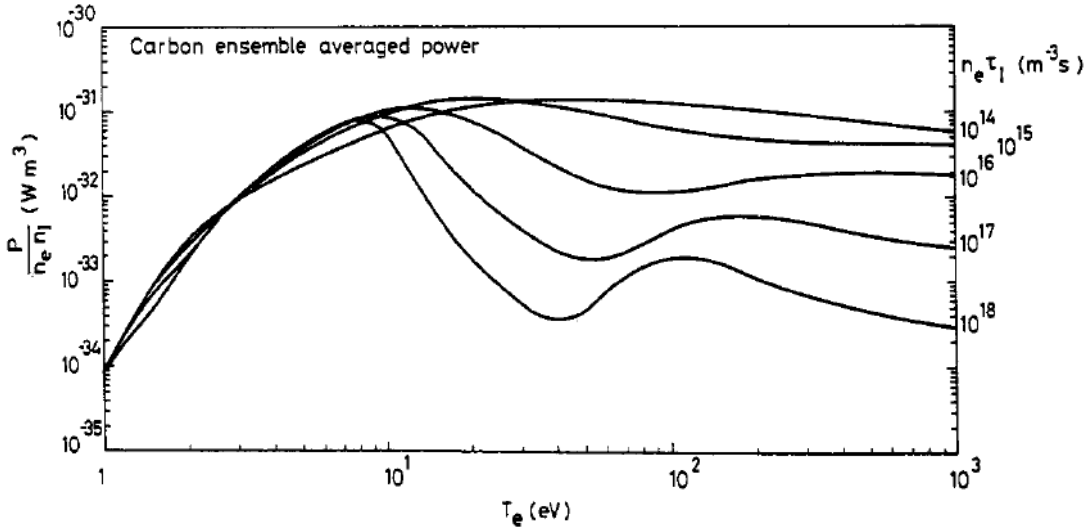

(a) Carbon.

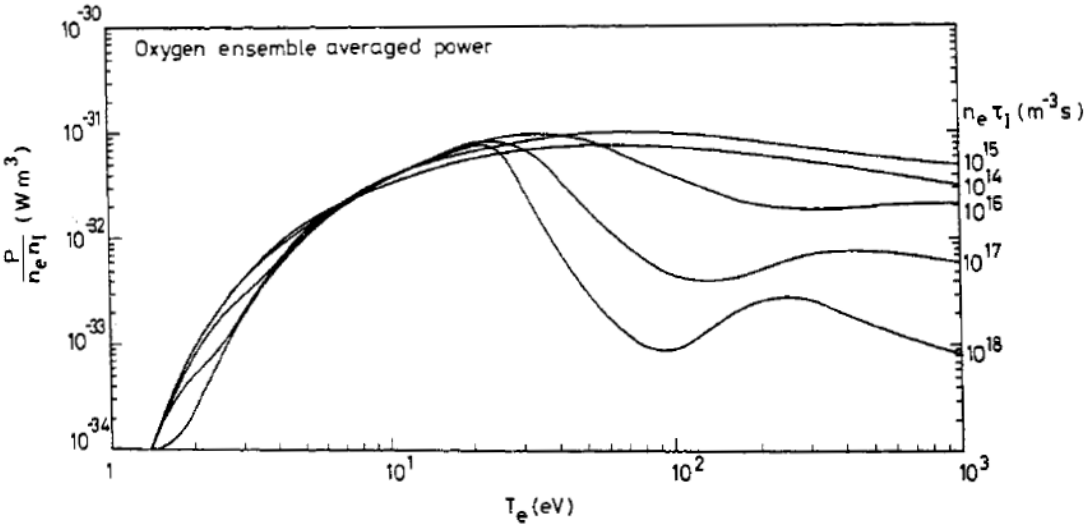

(b) Oxygen.

Figure 4.3: Ensemble averaged radiative power [5].

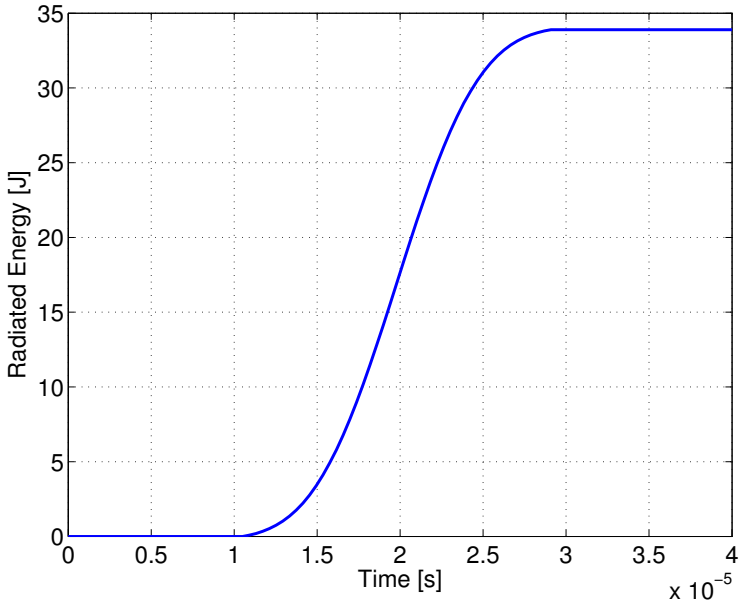

Figure 4.4: Total radiated energy calculated as a function of time.

The inherent uncertainty in this estimation is characteristically higher than the other estimates of lost energy. This is primarily due to the large sensitivity to the magnitude, temporal, and spatial variation in density ($P_{rad} \propto n^2$). In addition, suspected deviations from a maxwellian electron temperature distribution add to this uncertainty. However, the calculated value of $\approx$ 35 J matches the deficit estimated by subtracting the other energy estimates from the total observed power into the plasma.

4.2.6 Ionization Energy

In order to estimate the amount of frozen flow loss in the form of ionization energy, the average charge of the ions must be determined. It is necessary for the

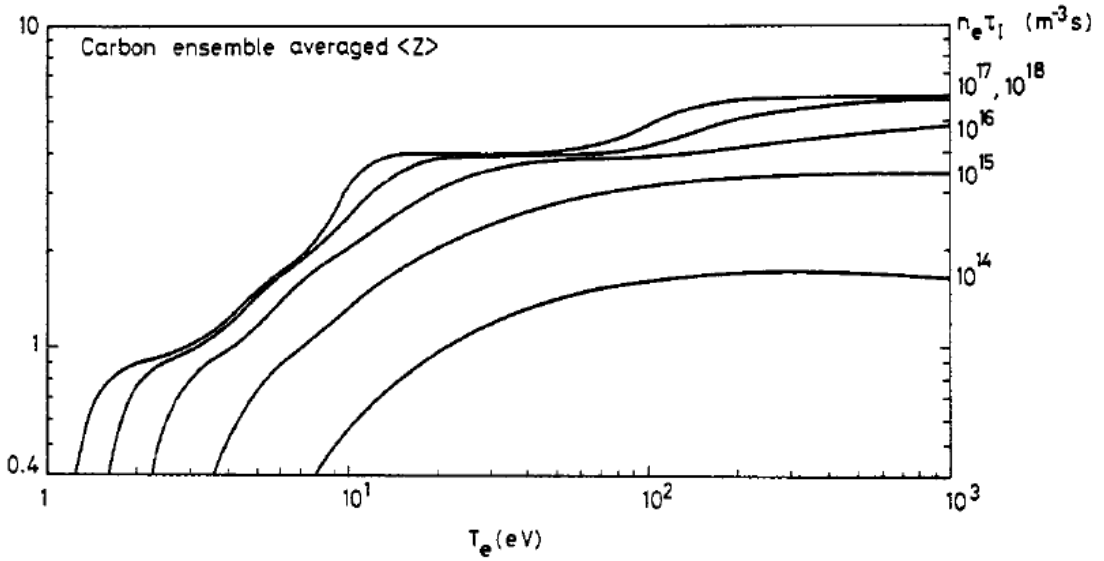

(a) Carbon.

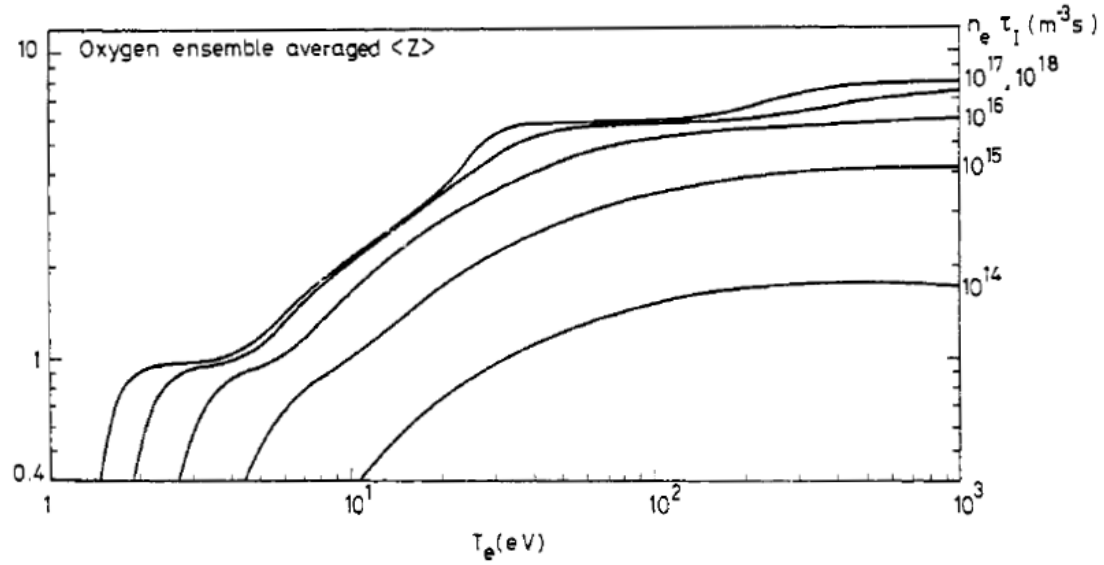

(b) Oxygen.

Figure 4.5: Ensemble averaged mean ionic charge ($\langle Z \rangle$) [5].

ions to be at least singly charged in order to be accelerated by the thruster, however, production of multiply charged ions is costly in terms of energy (the first ionization potential of nitrogen is 12.13 eV, the second is 20.97 eV [36]). Since, as stated above, the atomic processes are not in coronal equilibrium, the average atomic charge is time dependent and must be computed numerically. Again, using the model of Carolan and Piotrowicz, the behavior of nitrogen is extrapolated from the behavior of carbon and oxygen (see Figures 4.5). For the densities and temperatures present in ELF over the residence time of the FRC, the mean ionization is ≈ 1.

Assuming that all the particles accelerated by the thruster were ionized during acceleration, the ionization energy required to form the FRC can be expressed as the sum of the first ionization energy and the dissociation energy per particle times the number of particles.

$$E_{iz} = N\left(\varepsilon_{iz} + \varepsilon_{diss}\right) \tag{4.17}$$

Where ε_{iz} is the first ionization energy (stated above), and ε_{diss} is the molecular dissociation energy per ion (9.76 eV/N^2 $\rightarrow$ 4.88 eV/ion [37]). Using these values, the ionization losses in ELF are approximately 2.1 J.

4.2.7 Total Losses and Uncertainty

As stated earlier, there is a certain degree of uncertainty inherent in all of these estimates. This analysis is by no means intended to be completely rigorous. The intent is to obtain estimates the amount of energy lost via each mechanism for the purposes of targeting areas of interest for future thruster improvement.

Symbol	Description	Energy [J]	% Total	Error
E_{in}	RMF Energy Input	46	100	10%
E_{KE}	Bulk Kinetic Energy	3.7	8	30%
E_{th+B}	Thermal and Magnetic Energy	3.8	8	30%
E_{iz}	Ionization Energy	2.1	4.6	15%
E_{rad}	Radiated Energy	35	78	40%
E_{conv}	Convected Energy	0.24	0.5	40%
E_{res}	Energy Dissipated in Flux Consesrvers	0.16	0.3	25%
E_{sc}	Screened RMF Energy	0.45	1	90%

= Observed Quantity
= Calculated Quantity

Figure 4.6: Energy into various channels during the standard shot.

Figure 4.6 summarizes the results of the various energy estimates, along with the fraction of total energy that each channel consumes, and the estimated uncertainty (expressed as the fraction of the energy in the particular loss mechanism).

Mechanisms marked as "measured" quantities are calculated directly from experimental observed quantities, while the mechanisms marked as "calculated" are determined using the above mentioned methods, with experimentally measured quantities as input.

4.3 Potential Efficiency

It is important to understand that the relative amounts of energy estimated in each loss mechanism in the previous section may vary by large amounts depending on the specific details of the ionization, formation, and ejection process. In order to effectively judge the potential of the ELF concept as a thruster, one must first gain an insight as to the degree to which the loss mechanisms can be reduced. In

order to more effectively illustrate this, the example of operation using xenon as a propellant is explored. It is assumed that the mass and final velocity (kinetic energy) of the FRC are the same as in the standard shot ($E_{KE} \approx 3.7$ J).

4.3.1 RMF Energy at Ionization

As was seen during operation in xenon in Section 3.11, the amplitude at which the RMF ionization process took place limited the power level at which the formation process took place. This is a consequence of the RMF ramp up process used in ELF to introduce large amounts of energy into the tank circuit. This approach is not the only means of achieving the goal of putting energy into the tank, it is merely the approach used in ELF (in Section 4.4 an alternative method which avoids this issue is presented). In what follows, it is assumed that energy is added to the plasma in a similar manner as it was during operation in nitrogen.

4.3.2 Thermal and Magnetic Energy

Since the FRC cannot be expanded indefinitely, thus, there will always be a residual amount of thermal energy left in the plasmoid after exhaustion representing a frozen flow loss. In the chosen xenon example, the residual drift temperature is chosen to be identical to that measured during the standard shot (operation in nitrogen) to illustrate the effect of merely changing the propellant species. The total magnetic and thermal energy is then proportional to the total number of particles within the FRC, which is roughly 10 % of the number of nitrogen ions in

the standard shot.

$$E_{th+B} = \frac{5}{2} N k T_{res} \tag{4.18}$$

$$E_{th+B} = \frac{5}{2} \frac{m_F R C}{m_i} k T_{res} \tag{4.19}$$

This thermal and magnetic energy component of the xenon plasmoid is computed to be ~ 0.4 J.

4.3.3 Ionization Frozen Flow Losses

The ionization energy can be reduced by increasing the ratio of the ionic mass to the ionization energy per particle. Operation in a higher mass gas (xenon in this case) can drastically reduce this ratio (for xenon, $\varepsilon_{iz} = 12.3$ ev/ion [36]). In addition, there is no molecular dissociation which must take place, further reducing the energy requirements. Thus, much less energy must be spent on ionization for a given FRC mass.

$$E_{iz} = N \left(\varepsilon_{iz} + \varepsilon_{diss} \right) \tag{4.20}$$

$$E_{iz} = m_{frc} \left(\frac{\varepsilon_{iz} + \varepsilon_{diss}}{m_i} \right) \tag{4.21}$$

For an FRC of equal mass to the standard shot, the ionization energy required for xenon is ≈ 0.14 J.

4.3.4 Radiation

The radiative loss was, by far, the most severe loss mechanism present during the standard shot. However, among other things, the radiative power is proportional to the square of the particle density. Time-dependant, radiative power data for xenon is unavailable, however an examination of several other high atomic mass species reveals that the normalized power ($\frac{P}{n_e n_i}$) saturates at a similar value across species, and is relatively constant at the higher electron temperatures consistent with pressure balance in ELF. Thus, the total radiated power for similar FRC formation and ejection processes (of the same total mass) scales as N^2.

This powerful density dependance drastically decreases the total radiative losses. For xenon, the total particle count is roughly 10 % that of nitrogen, so the plasma radiates at roughly 1 % of the power of nitrogen. The total radiated energy during operation in the xenon example is estimated to be ~ 0.4 J.

4.3.5 Convective Losses

The convective losses for a xenon FRC are difficult to estimate due to the fact that, at the relatively low magnetic fields present in ELF, the ion gyroradius is much larger than the characteristic size of the plasmoid. However, it has been observed during testing of ELF that the confinement properties of a xenon FRC are not very different from that of a nitrogen FRC (see Section 3.11). Thus, the fraction of convectively lost particles is estimated to be roughly the same as was the case in nitrogen (roughly 2 %). This means that the amount of FRC energy within

the cone was roughly 1.02 times that of the sum of the magnetic, thermal, and kinetic energies in the drift section. The convective losses for the xenon example are estimated to be ~ 0.1 J.

4.3.6 Resistive Losses in the Flux Conservers

The resistive losses in the flux conservers are proportional to the residence time of the FRC and the amount of increase in the axial magnetic field due to the presence of the FRC ($E_\eta \propto (\Delta B)^2 l_{FRC} \Delta t$). Since the magnetic pressure is proportional to nkT, the quantity lB^2 is proportional to the total FRC energy (magnetic and thermal). Thus, if the formation and ejection timescales are similar, the ratio of energy resistively dissipated in the flux conservers (comparing nitrogen and xenon) should be equal to the ratio of the total FRC energy within the cone.

$$E_{\eta_{Xe}} = E_{\eta_{N_2}} \frac{E_{(ke+B)_{Xe}}}{E_{(th+B)_{N_2}}} \tag{4.22}$$

In this manner, the resistive losses in the flux conservers for xenon are computed to be ~ 54 % that of nitrogen, or ~ 0.09 J.

4.3.7 Screened RMF Energy

The screened RMF energy is a function of the maximum amount that the fraction γ/λ attains (see Section 4.1). This determines the amount of RMF energy which is injected into the FRC before the RMF currents are screened by the outer-edge plasma. The specific number depends upon the details of the formation

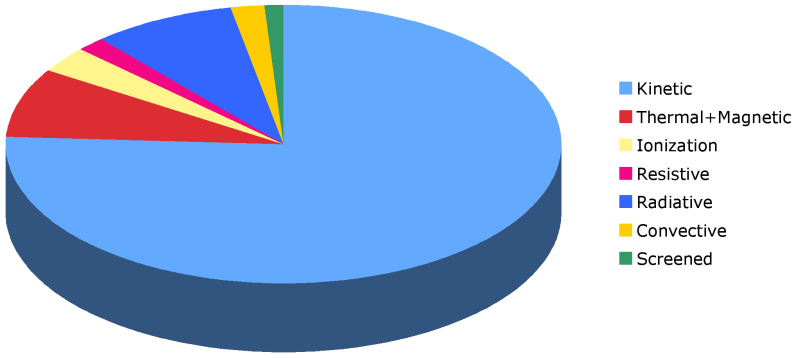

Figure 4.7: Estimated energy distribution during Xenon operation.

process, however, it is always possible to operate at a condition where this number is high. For the xenon example, the fraction of RMF energy that is screened, and hence lost, is taken to be the same as in the nitrogen discharge ($\sim$ 1 %). Thus, the amount of screened RMF energy is $\sim$ 0.05 J.

4.3.8 Hypothetical Xenon Thruster Efficiency

Based on these approximations, the total amount of RMF energy entering the system is computed to be 4.88 J. If the thermal, magnetic, and kinetic energies are taken to be useful forms of energy (as is taken to be the case in the ELF experiment), the estimated thruster efficiency in xenon is 84 % (if only the kinetic energy is counted, the thruster efficiency becomes 76 %.

4.4 Future Work

Much has been learned over the course of testing with ELF; a new and very promising method of FRC formation using RMF current drive technology has been discovered, the utility of the FRC confinement concept to space propulsion has been investigated, the behavior and operation of the ELF thruster was studied, and a significant amount of technological development has taken place. The level on knowledge regarding the ELF-type propulsion concept has been increased from the vague notion of using RMF to form and eject an FRC, to the point at which several rigorous scientific studies on the specific physics taking place within the thruster can be undertaken.

4.4.1 Experimental Upgrades

Since the ELF experiment was a proof-of-concept experiment, there was a fairly high degree of uncertainty inherent in the measured and estimated quantities. This is acceptable for the current time, however in future studies of the particular operational aspects of ELF, the amount of experimental uncertainty must be reduced.

Specifically the estimate of the amount of energy lost due to radiation must become more accurate as it is the dominant loss mechanism present for the specific propellant and conditions tested. Specifically, the addition of a spectrometer and bolometer to the diagnostic arsenal of the experiment is needed. Numerical simulations of the ionization and formation processes would also be particularly useful to the development of the thruster.

While the use of the ballistic pendulum was necessary for this initial phase of research due to the limited experimental facilities, its use presented several difficulties. In the next phase of ELF development, the use of a thrust stand is a vital experimental component. A thrust stand would provide an unambiguous measurement of thrust produced, and eliminate questions of missing mass and the accuracy of measuring the impulse of a hot plasma using a pendulum.

In addition to a thrust stand, a large vacuum chamber is needed to accurately simulate space and allow the ejected plasmoid to properly expand. This adds to the accuracy of a thrust stand measurement as well as enables more detailed studies of the accleration/expansion process during operation.

Currently MSNW has purchased a large (3 m diameter) vacuum vessel, and plans are in place to construct a thrust stand within the chamber for use as a general thruster testing facility.

4.4.2 Thruster Technology

As a result of the findings of the ELF study, several key areas of physics were identified as being vital to the operation of the thruster, and need to be the subject of future study. In particular the details of the ionization and formation process were found to be critical to the efficiency of the thruster. In the configuration previously described, the energy transfer rate of formation is intimately tied to the RMF amplitude at which the main ionization process takes place. The initiation of the ionization process is sensitively dependent upon the gas initial distribution, density, magnetic field configuration, induced electric field, and the particular species

of propellant. Thus, as was seen during operation in xenon, the range of parameter space available for exploration is limited by the current RMF configuration.

Alternative RMF systems can be constructed in order to decouple the energy and power of the RMF formation from the minimum ionization conditions of the propellant. Currently under development at MSNW is a new RMF setup which eliminates the need for the RF driver and transformer; instead the tank capacitor is charged to a pre-determined voltage, a switch is closed to complete the tank circuit, and the system rings at its characteristic frequency until all of the initial energy is either consumed by the plasma or dissipated. In this manner, the RMF can start at any desired amplitude, with less energy dissipated in the circuit prior to ionization, and no inefficient, heavy RF source. Thus, future versions of ELF will be much lighter and more compact, making them more amenable to testing on a thrust stand (or being developed into a high power, lightweight thruster).

The specific antennae geometry of the RMF system also has a large effect on the ionization and formation process. The main RMF ionization process occurs, at least initially, due to large electric potentials being developed along the magnetic field lines within the formation section (from both the bias and RMF systems), with the mean free path of the electrons and the ionization cross section of the propellant determining the specific conditions at which the ionization process begins. The RMF system can be thought of as being similar to an AC transformer in the sense that a loop voltage is induced within the plasma via Faraday's Law. The RMF system as tested, had the RMF antennae for a given channel in series with each other and the remainder of the tank circuit (a Helmholtz pair with the magnets

in series). This effectively formed a 2:1 transformer with the plasma. Variations of the turns-ratio of the RMF-plasma system would affect the magnitude of the magnetic field and the induced electric field, as well as the operation frequency of the system. Changes to the RMF frequency and circulating energy content can be affected through changes to the value of the tank capacitor. In addition, alteration of the size of the formation region changes the magnitude of the induced electric and magnetic fields within the thruster.

Changes to the gas distribution within the thruster prior to the discharge have proven to have a large effect on the performance of the thruster. In the configuration tested, the radial neutral gas profile was uniform, while the axial profile was determined by the gas puff, being heavily weighted towards the upstream end of the thruster. Testing with a different gas-feed system (such as an array of ports which feed gas into the thruster radially) would enable the study of different distributions of neutral gas. In addition, the maximum attainable thruster power is mainly determined by the fill rate of the neutral gas. Using a configuration in which the gas fill process was increased, the maximum thruster power would be increased proportionally. In this way, the operational power could be increased without significant changes to the other thruster systems.

As stated earlier, in addition to the gas distribution and density, the specific atomic properties of the propellant are also play a key role in the operation of the thruster. The first ionization energy per particle, the atomic mass, and the ionization cross section are three of the most important parameters. The majority of the testing which has taken place thus far has utilized nitrogen as a propellant,

mainly due to the fact that the ionization took place at an attractive RMF energy condition. As mentioned in the previous section, there is vast potential for the improvement of the thruster efficiency through the use of alternative propellants, as well as important implications for the mission design of spacecraft utilizing an ELF-type thruster. Additionally, the confinement properties of FRCs with extremely low kinetic parameters (s) may be investigated in these studies, and are important to the effective ejection of high atomic mass plasmoids. For these reasons, it is important that a subject of future experiments is an investigation of the operation as a function of the choice of propellant.

The process of conversion of the thermal and magnetic energy to bulk kinetic energy through plasmoid expansion is a potentially very efficient. A practical limitation on the fraction of energy that can effectively be converted is the size and mass of the magnetic structure necessary to establish the needed axial magnetic field. There will be a point at which additional thruster mass will offset any energy conversion gains. Through the use of the larger vacuum chamber mentioned above additional magnets of varying size can be placed near the exit of the thruster in order to optimize the configuration of the diverging magnetic field. Additionally, numerical studies can serve as a method for the rapid variation of parameters that would be prohibitively difficult to sweep experimentally (such as the pitch angle of the cone).

In conclusion, the ELF thruster concept has been shown to possess enormous potential as a space thruster system. As a direct result of the testing performed, several grants for additional studies have been secured, and the future for the

development of this system appears bright.

Appendix A

Sample MATLAB code

A.1 Voltage Probe Calibration File

```
function [data,time]=C00000RMFA_Volts(nShot)
% calibration file to convert measured signal to voltage

d = datExpr('RMFA_V',nShot,0,0);  % pull data
d.y=lowPass(d.y,d.t,1e6,1e5);  % filter
signal=(d.y-mean(d.y(1:10000)));  % get normalized signal

time=d.t;  % get time
const = 1.10;
R = 3.9e3;  % resistance
nt = 1;  % number of turns
data = signal*2*R*const/nt;  % into 50 ohms -> *2
data = data + cumsum(data.*2.4e-5);

end
```

A.2 Internal Magnetic Probe Calibration File

```
function [data,time]=C00000BBP1_B(nShot)
% calibration file to convert measured signal to magnetic field

d = datExpr('BBP1',nShot,0,0);  % pull data
% d.y=lowPass(d.y,d.t,2e5,2e4);  % filter
signal=(d.y-mean(d.y(1:35000)));  % get normalized signal

Rp = 7.236; % probe output impedance

time=d.t;  % get time
npoints = size(time);  % number of time points
dt = time(2)-time(1);

% int_V = integral of voltage
int_V = zeros(npoints);
for i = 2:npoints
    int_V(i) = int_V(i-1) + signal(i-1)*dt;
end

% ddt_V = time derivative of voltage
ddt_V = zeros(npoints);  % dvolts/dt
for i = 2:npoints
    ddt_V(i) = (signal(i)-signal(i-1))./dt;
end

L = 395.4e-6;
R = 10e3;
C = 10e-9;
A = pi*0.0063^2;  % area in m^2
N = 200; % number of turns
data = (R.*C.*signal + int_V + L.*C.*ddt_V)./(N.*A);
data= -1.*data.*10000;  % tesla to gauss

end
```

A.3 Pendulum Signal to Impulse Conversion

```
1  function [impulse]=multi_auto_impulse(shot)
2  % input a vector of shot numbers and get a vector of impulses
3  % also plots measured signal and corrected values for
       examination
4  clear impulse
5
6  %169 Pendulum Calibration Data
7  xcal = [0.00149 0.00238 0.00339 0.00455 0.00591 0.00750 0.00948
       ...
8       0.01075 0.01212 0.01399 0.01555 0.01653 0.01752 0.01836
           0.01909];
9  vcal = [4.502 4.008 3.509 3.008 2.505 2.000 1.500 1.232 1.000
       0.766 ...
10      0.624 0.552 0.493 0.448 0.417];
11 vmax = 5.28;  % max voltage the sensor puts out
12 norm = vmax/5;  % normalize signal to 5 volts
13 Calibration_Constant = 1.16; % [mN/mm] from DC testing
14 max_correction = 0.81885;  % from measurements
15 min_correction = 1.356151;  % from measurements
16 p = polyfit(norm.*vcal,xcal,6); % p(v,x)
17
18 xrange = 200;
19
20 for i = 1:length(shot)
21     % for every shot compute the impulse
22     d1 = datExpr('PENDULUM',shot(i),0,0);  % pull data
23     d2 = datExpr('PZERO',shot(i),0,0);  % pull data
24     signal = d1.y - mean(d1.y(3000:4000));
25     offset = mean(d2.y(1:40000)) + mean(d1.y(3000:4000)); % add
           offset at end
26
27     % check to see if the 2008 card is maxed out at any point
28     maxd1 = max(d1.y);
29     mind1 = min(d1.y);
30     if maxd1 > 0.247
31         disp(['check for 2008 over-volt (max) for shot #',
               num2str(shot(i))])
32     end
33     if mind1 < -0.247
34         disp(['check for 2008 over-volt (min) for shot #',
               num2str(shot(i))])
35     end
```

```
36
37      imxV = 4760;  % index of data point near maximum
38      imnV = 6010;  % index of data point near minimum
39
40      % fit the voltage data to smooth functions around the max
           and min
41      tmx = d1.t((imxV-xrange):(imxV+xrange));  % time range of
           approximation around maximum
42      tmn = d1.t((imnV-xrange):(imnV+xrange));  % time range of
           approximation around minimum
43      pmx = polyfit(tmx, signal((imxV-xrange):(imxV+xrange)), 2);
44      pmn = polyfit(tmn, signal((imnV-xrange):(imnV+xrange)), 2);
45      asig_mx = polyval(pmx,tmx);  % approximate signal around
           maximum
46      asig_mn = polyval(pmn,tmn);  % approximate signal around
           minimum
47
48      amxV = max(asig_mx);  % maximum of approximate signal
49      amnV = min(asig_mn);  % minimum of approximate signal
50      Xmax = polyval(p,amxV+offset);
51      Xmin = polyval(p,amnV+offset);
52      Xmax_c = polyval(p,amxV*max_correction+offset);  %
           impedance corrected signal
53      Xmin_c = polyval(p,amnV*min_correction+offset);
54
55      dx = abs(Xmax_c-Xmin_c)/2;
56      impulse(i) = 0.923797.*(1-(1-(dx./0.56).^2).^0.5).^0.5;
57
58      % Plot Signals for examination by operator.
59      signal(3000:4000) = 2;
60      figure
61      hold on
62      plot(d1.t,signal+offset,'-k')  % display measured signal
63      plot(d1.t(imxV),signal(imxV)+offset,'.r')  % display center
           of approximation
64      plot(d1.t(imnV),signal(imnV)+offset,'.r')
65      plot(tmx,asig_mx+offset,'-r')  % display approximate signal
66      plot(tmn,asig_mn+offset,'-r')
67      plot(d1.t,ones(size(d1.t)).*amxV+offset,'-r')  % max
68      plot(d1.t,ones(size(d1.t)).*amnV+offset,'-r')  % min
69      plot(d1.t,ones(size(d1.t)).*amxV.*max_correction+offset,'-b
           ')  % corrected max
70      plot(d1.t,ones(size(d1.t)).*amnV.*min_correction+offset,'-b
           ')  % corrected min
71      hold off
```

```
72      grid on
73      xlabel('Time [s]')
74      ylabel('Volts')
75      title(['Pendulum Data for Shot # ',num2str(shot(i))])
76  end
77
78  impulse = impulse';
79  end
```

A.4 Langmuir Signal to Velocity Conversion

```
function [CM_Velocity]=multi_auto_velocity(shot)
% determines center-of-mass velocity from two langmuir traces
% plots Langmuir traces with center of mass indicators for
    examination
clear CM_Velocity

for i = 1:length(shot)
    d1 = datExpr('Lang1',shot(i),0,0);  % pull data
    d1.y=lowPass(d1.y,d1.t,1.5e5,1e4);  % lowpass @ 150kHz
    d1.y=(d1.y-mean(d1.y(1:40000)));  % normalize signal
    % d1.y = d1.y+cumsum(d1.y.*3.7e-5);  % droop correction
    d2 = datExpr('Lang2',shot(i),0,0);  % pull data
    d2.y=-1.*lowPass(d2.y,d2.t,1.5e5,1e4);  % lowpass @ 150kHz
    d2.y=(d2.y-mean(d2.y(1:40000)));  % normalize signal
    % d2.y = d2.y+cumsum(d2.y.*5.2e-5);  % droop correction

    % obtain integral of the signal
    iend = length(d2.y);
    dt = d1.t(2)-d1.t(1);
    int_NV1 = zeros(iend,1);
    int_NV2 = zeros(iend,1);
    for n = 2:iend
       int_NV1(n) = int_NV1(n-1) + d1.y(n-1)*dt;  % int_NV =
          integrated signal
       int_NV2(n) = int_NV2(n-1) + d2.y(n-1)*dt;
    end
    int_NV1 = int_NV1 - mean(int_NV1(99000:100000));  % correct
        for offset
    int_NV2 = int_NV2 - mean(int_NV2(99000:100000));

    % center of mass is when half of the particle flux has
       passed
    iCM1 = 0;
    iCM2 = 0;
    [PeakNV1,iPeakNV1] = max(int_NV1);
    [PeakNV2,iPeakNV2] = max(int_NV2);
    for n = (iend/2):iend
        if ((int_NV1(n)>PeakNV1/2) & (iCM1==0))
            iCM1 = n;
        end
        if ((int_NV2(n)>PeakNV2/2) & (iCM2==0))
            iCM2 = n;
```

```
39          end
40      end
41      if iCM1==0
42          errormsg = ['Faied to read velcoity for shot #',
                num2str(shot(i))];
43          disp(errormsg)
44          CM_Velocity(i) = 999;
45      elseif iCM2==0
46          errormsg = ['Faied to read velcoity for shot #',
                num2str(shot(i))];
47          disp(errormsg)
48          CM_Velocity(i) = 999;
49      else
50          tCM1 = d1.t(iCM1);
51          tCM2 = d2.t(iCM2);
52          CM_Velocity(i) = 0.39/(tCM2-tCM1)/10000; % [cm/us]
53      end
54
55      % plot traces with landmarks
56      figure
57      subplot(2,1,1)
58      hold on
59      plot(d1.t,(d1.y),'-k')
60      if iCM1~=0
61          plot(d1.t(iCM1), (d1.y(iCM1)), '.b');
62      end
63      axis([0,500e-6,1.1*min(d1.y),1.1*max(d1.y)]);
64      grid on
65      ylabel('Voltage [V]')
66      xlabel('Time [s]')
67      title(['Langmuir Probe 1 (Shot # ',num2str(shot(i)),')'])
68      hold off
69      subplot(2,1,2)
70      hold on
71      plot(d2.t,(d2.y),'-k')
72      if iCM1~=0
73          plot(d2.t(iCM2), (d2.y(iCM2)), '.b');
74      end
75      axis([0,500e-6,1.1*min(d2.y),1.1*max(d2.y)]);
76      grid on
77      ylabel('Voltage [V]')
78      xlabel('Time [s]')
79      title(['Langmuir Probe 2 (Shot # ',num2str(shot(i)),')'])
80      hold off
81
```

```
82 %     % plot integrals with landmarks
83 %     figure
84 %     subplot(2,1,1)
85 %     hold on
86 %     plot(d1.t,int_NV1,'-k');
87 %     plot(d1.t(iCM1), (int_NV1(iCM1)), '.r');
88 %     grid on
89 %     hold off
90 %     subplot(2,1,2)
91 %     hold on
92 %     plot(d2.t,int_NV2,'-k');
93 %     plot(d2.t(iCM2), (int_NV2(iCM2)), '.r');
94 %     grid on
95 %     hold off
96 end
97
98 CM_Velocity = CM_Velocity';
99 end
```

Bibliography

[1] M. Tuszewski, "Field reversed configurations," *Nuclear Fusion*, vol. 28, no. 11, pp. 2033–2092, 1988.

[2] R. Milroy, "A magnetohydrodynamic model of rotating magnetic field current drive in a field-reversed configuration," *Physics of Plasmas*, vol. 7, p. 4135, 2000.

[3] R. Jankovsky, S. Tverdokhlebov, and D. Manzella, "High power Hall thrusters," in *35th joint propulsion conference, AIAA-99-315745*, 1999.

[4] M. Lieberman and A. Lichtenberg, *Principles of plasma discharges and materials processing*. Wiley-Interscience, 1994.

[5] P. Carolan and V. Piotrowicz, "The behaviour of impurities out of coronal equilibrium," *Plasma Physics*, vol. 25, pp. 1065–1086, 1983.

[6] K. Tsiolkovsky, "The exploration of cosmic space by means of reaction motors," *Scientific Review, Moscow and St. Petersburg*, 1903.

[7] N. G. R. Center, "Powering the future - NASA Glenn contributions to the International Space Station (ISS) electrical power system." NASA Facts, 2000. FS-2000-11-006-GRC.

[8] B. Spence, S. White, N. Wilder, T. Gregory, M. Douglas, R. Takeda, N. Mardesich, T. Peterson, B. Hillard, P. Sharps, *et al.*, "Next Generation UltraFlex Solar Array for NASAs New Millennium Program Space Technology 8," in *2005 IEEE Aerospace Conference*, pp. 824–836, 2005.

[9] R. Frisbee, "Advanced space propulsion for the 21st century," *Journal of Propulsion and Power*, vol. 19, no. 6, pp. 1129–1154, 2003.

[10] E. Baumeister, R. Rovang, J. Mills, J. Sercel, and R. Frisbee, "A Potassium Rankine Multimegawatt Nuclear Electric Propulsion Concept," in *Energy Conversion Engineering Conference, 1990. IECEC-90. Proceedings of the 25th Intersociety*, vol. 1, 1990.

[11] H. Blevin and P. Thonemann, "Plasma confinement using an alternating magnetic field," *Nucl. Fusion Suppl*, 1962.

[12] J. Slough, D. Kirtley, and T. Weber, "Pulsed plasmoid propulsion: The ELF thruster," in *International Electric Propulsion Conference Technical Program*, IEPC-2009-265, 31st International Electric Propulsion Conference, Ann Arbor, Michigan, USA, 2009.

[13] A. Hoffman, H. Guo, K. Miller, and R. Milroy, "Principal physics of rotating magnetic-field current drive of field reversed configurations," *Physics of Plasmas*, vol. 13, p. 012507, 2006.

[14] I. Jones, "A review of rotating magnetic field current drive and the operation of the rotamak as a field-reversed configuration (Rotamak-FRC) and a spherical tokamak (Rotamak-ST)," *Physics of plasmas*, vol. 6, p. 1950, 1999.

[15] I. Jones and W. Hugrass, "Steady-state solutions for the penetration of a rotating magnetic field into a plasma column," *Journal of Plasma Physics*, vol. 26, p. 441, 1981.

[16] G. Votroubek, J. Slough, S. Andreason, and C. Pihl, "Formation of a Stable Field Reversed Configuration through Merging," *Journal of Fusion Energy*, vol. 27, no. 1, pp. 123–127, 2008.

[17] G. Votroubek, J. Slough, A. Blair, C. Pihl, S. Andreason, R. Milroy, and T. Weber, "Compression of Dynamically Formed and Merged FRCs," in *APS Meeting Abstracts*, p. 4014, 2007.

[18] J. Slough, S. Andreason, H. Gota, C. Pihl, and G. Votroubek, "The Pulsed High Density Experiment: Concept, Design, and Initial Results," *Journal of Fusion Energy*, vol. 26, no. 1, pp. 199–205, 2007.

[19] G. Votroubek, J. Slough, C. Pihl, and D. Kirtley, "Plasma Liner Formation and Compression Experiments on PLC," in *APS Meeting Abstracts*, p. 7003, 2009.

[20] R. Jahn, *Physics of electric propulsion.* Dover Publications, 2006.

[21] S. Tobin, W. Reass, L. Schrank, G. Wurden, H. Guo, A. Hoffman, and D. Lotz, "Rotating magnetic field oscillator system for current drive in the translation, confinement, and sustainment experiment," *Review of Scientific Instruments*, vol. 72, p. 3528, 2001.

[22] S. Andreason, *The Pulsed High Density Experiment (PHDX): Design, construction, results.* PhD thesis, University of Washington, 2008.

[23] R. Bayard and D. Alpert, "Extension of the low pressure range of the ionization gauge," *Review of Scientific Instruments*, vol. 21, pp. 571–572, 1950.

[24] T. Flaim and P. Ownby, "Observations on Bayard-Alpert ion gauge sensitivities to various gases," *Journal of Vacuum Science and Technology*, vol. 8, no. 5, pp. 661–662, 1971.

[25] I. Hutchinson, *Principles of plasma diagnostics.* Cambridge University Press, 2002.

[26] T. Ziemba, J. Slough, and R. Winglee, "High Power Helicon Propulsion Experiments," in *AIP Conference Proceedings*, vol. 746, p. 965, 2005.

[27] W. Vincenti and C. Kruger, *Introduction to physical gas dynamics.* Krieger Publishing, 2002.

[28] H. Liepmann and A. Roshko, *Elements of gasdynamics.* Dover Publications, 2001.

[29] J. Meek and J. Craggs, *Electrical breakdown of gases*. John Wiley & Sons, 1978.

[30] R. Wijsman, "Breakdown probability of a low pressure gas discharge," *Physical Review*, vol. 75, no. 5, pp. 833–838, 1949.

[31] R. Farquhar, B. Ray, and J. Swift, "Determination of cathode quantum efficiencies using statistical time lag measurements," *Journal of Physics D: Applied Physics*, vol. 13, pp. 2067–2075, 1980.

[32] J. Slough. Private communication.

[33] A. Kuethe and C. Chow, *Foundations of aerodynamics*. John Wiley & Sons, 1998.

[34] J. Slough, "Plasma Sail Propulsion Based on the Plasma Magnet," in *International Electric Propulsion Conference Technical Program*, IEPC-2007-15, 30th International Electric Propulsion Conference, Florence, Italy, 2007.

[35] M. Tuszewski and R. Linford, "Particle transport in field-reversed configurations," *Physics of Fluids*, vol. 25, p. 765, 1982.

[36] J. Sansonetti and W. Martin, "Handbook of Basic Atomic Spectroscopic Data," 2010. `http://physics.nist.gov/PhysRefData/Handbook/index.html`.

[37] D. Frost and C. McDowell, "The dissociation energy of the nitrogen molecule," *Proceedings of the Royal Society of London. Series A, Mathematical and Physical Sciences*, vol. 236, no. 1205, pp. 278–284, 1956.

Vita

Thomas Weber has been interested in spaceflight since he was a small child. He earned a Bachelors of Aerospace Engineering and Mechanics from the University of Minnesota in 2005 and a Masters of Science in Aeronautics and Astronautics at the University of Washington in 2007. In 2010 he received his Ph.D. from the Department of Aeronautics and Astronautics at the University of Washington for his research into a novel form of plasma propulsion.